Advances in High-Order Harmonic Sources and Applications to Free-Electron Laser Pulse Characterization

Dissertation
zur Erlangung des Doktorgrades
an der Fakultät für Mathematik, Informatik und Naturwissenschaften
Fachbereich Physik
der Universität Hamburg

vorgelegt von
Agata Azzolin

Hamburg
2025

Gutachter/innen der Dissertation:	Prof. Dr. Francesca Calegari
	Prof. Dr. Markus Drescher
Zusammensetzung der Prüfungskommission:	Prof. Dr. Francesca Calegari
	Prof. Dr. Markus Drescher
	Prof. Dr. Franz X. Kärtner
	Prof. Dr. Markus Ilchen
	Prof. Dr. Daniela Pfannkuche
Vorsitzende/r der Prüfungskommission:	Prof. Dr. Daniela Pfannkuche
Datum der Disputation:	09.02.2026
Vorsitzender des Fach-Promotionsausschusses PHYSIK:	Prof. Dr. Johannes Haller
Leiter des Fachbereichs PHYSIK:	Prof. Dr. Markus Drescher
Dekan der Fakultät MIN:	Prof. Dr.-Ing. Norbert Ritter

Declaration on oath

I hereby declare and affirm that this doctoral dissertation is my own work and that I have not used any aids and sources other than those indicated. If electronic resources based on generative artificial intelligence (gAI) were used in the course of writing this dissertation, I confirm that my own work was the main and value-adding contribution and that complete documentation of all resources used is available in accordance with good scientific practice. I am responsible for any erroneous or distorted content, incorrect references, violations of data protection and copyright law or plagiarism that may have been generated by the gAI.

Furthermore, I declare that the dissertation submitted in electronic form (via the Docata upload) and the printed, bound copy submitted to the Physics Doctoral Study Office (Jungiusstraße 9, 20355 Hamburg) for archiving purposes are identical.

Place, Date

Signature

Summary

Attosecond and few-femtosecond light pulses provide the time resolution required to track and control the very first instants of electron dynamics in molecules and condensed matter. Since its first demonstration, High-order Harmonic Generation (HHG) sources have been at the core of experimental schemes aiming at unravelling ultrafast electron motion.

This thesis reports advancements in high-order harmonic sources and their applications to both solid-state spectroscopy and Free-Electron Laser (FEL) pulse characterization. First, it demonstrates and rationalizes efficient soft X-ray HHG in the so-called overdriven regime enabled by a custom-designed differentially pumped glass chip. This development directly addresses some of the technical challenges of conventional high-photon-energy HHG sources, providing a more accessible approach. Second, this work presents results on solid-state High-order Harmonic Generation (sHHG) spectroscopy in crystalline, amorphous, and semi-periodic TiO_2 samples. The experiment showcases the potential of HHG not only as a source, but also as a spectroscopic probe of the valence electrons governing materials functional properties. Finally, this thesis reports the experimental validation of Double-Blind Holography (DBH) of ultrashort FEL pulses. This is a fully optical platform for single-shot temporal characterization, phase retrieval, and few-femtosecond resolution delay tagging that is based on the interference with an unknown external field, in this case a standard HHG source.

Together, these developments extend the capabilities of high-order harmonic sources, opening new scenarios for investigating and controlling ultrafast electron dynamics in atoms, molecules and condensed matter, both with table-top schemes and at FELs.

Zusammenfassung

Attosekunden- und wenige Femtosekunden-Lichtimpulse bieten die erforderliche Zeitauflösung, um die allerersten Augenblicke der Elektronendynamik in Molekülen und kondensierter Materie zu verfolgen und zu steuern. Seit ihrer ersten Demonstration stehen Quellen für die Erzeugung höherer Harmonischer (Engl. High-order Harmonic Generation, HHG) im Mittelpunkt experimenteller Ansätze, die darauf abzielen, ultraschnelle Elektronenbewegungen zu entschlüsseln.

Diese Dissertation berichtet über Fortschritte bei Quellen für hochgradige harmonische Strahlung und deren Anwendungen sowohl in der Festkörper-Spektroskopie als auch bei der Charakterisierung von Impulsen aus Freie-Elektronen-Lasern (FEL). Zunächst wird eine effiziente Weichröntgen-HHG im sogenannten Overdriven-Regime demonstriert und rationalisiert, die durch einen speziell entwickelten, differentiell gepumpten Glaschip ermöglicht wird. Diese Entwicklung geht direkt auf einige der technischen Herausforderungen herkömmlicher HHG-Quellen mit hoher Photonenenergie ein und bietet einen insgesamt leichter zugänglichen Ansatz. Zweitens enthält sie Ergebnisse zur Festkörper-Spektroskopie der hochharmonischen Generation (Engl. solid-state High-order Harmonic Generation, sHHG) in kristallinen, amorphen und semiperiodischen TiO_2-Proben. Das Experiment zeigt das Potenzial von HHG nicht nur als Quelle, sondern auch als spektroskopische Sonde für die Valenzelektronen, die die funktionellen Eigenschaften von Materialien bestimmen. Schließlich berichtet diese Arbeit über die experimentelle Validierung der Double-Blind-Holographie (DBH) von ultrakurzen FEL-Impulsen: eine vollständig optische Plattform für die zeitliche Charakterisierung mit Einzelimpulsen, Phasenwiederherstellung und Verzögerungsmarkierung mit einer Auflösung von wenigen Femtosekunden, basierend auf der Interferenz mit einem unbekannten externen Feld, in diesem Fall einer Standard-HHG-Quelle.

Zusammen erweitern diese Entwicklungen die Fähigkeiten von Quellen für hochgradige Harmonische und eröffnen neue Szenarien für die Untersuchung und Steuerung ultraschneller Elektronendynamik in Atomen, Molekülen und kondensierter Materie, sowohl mit Tischgeräten als auch bei FELs.

Contents

List of Acronyms

ADK Ammosov-Delone-Krainov. 21–23, 30

ALD Atomic Layer Deposition. 58, 62, 63

ARPES angle-resolved photoemission spectroscopy. 95

BAM Beam Arrival Monitor. 84

BS beam-splitter. 105

CCD Charge-Coupled Device. 37, 81

CEP Carrier-Envelope Phase. 35, 37, 77

CMOS Complementary Metal-Oxide-Semiconductor. 37

CS Compact Support. 73, 75, 78, 79, 88, 89

DBH Double-Blind Holography. vii, ix, 8, 9, 73, 76–79, 81–84, 88, 90, 92, 96, 107

E-ADK Empirically-corrected ADK. 24, 31

FEL Free-Electron Laser. vii, ix, 8, 9, 76, 79, 81–84, 86, 88–92, 95, 96

FFT Fast-Fourier Transform. 78

FLICE Femtosecond Laser Irradiation followed by Chemical Etching. 34, 35

FROG-CRAB Frequency Resolved Optical Gating for Complete Reconstruction of Attosecond Bursts. 77

FT Fourier Transform. 78, 83, 84, 89, 90

FWHM Full-Width Half Maximum. 35, 37, 42, 47, 57, 90, 104, 107

GDD Group Delay Dispersion. 87–89

HH harmonic. 62–67

HHG High-order Harmonic Generation. vii, ix, 5–9, 13, 16, 17, 20, 21, 24, 27, 28, 30, 33, 35, 37, 39, 41, 48, 50, 53–56, 62, 76, 77, 81–84, 86, 90, 92, 95, 96, 99, 103, 105

LAM Laser Arrival Monitor. 84

LB Langmuir-Blodgett. 59, 63

MCP micro-channel plate. 37

MIR mid-infrared. 6, 13, 54, 69

NIR near-infrared. 6, 13, 54, 60, 105

OPA Optical Parametric Amplification. 6, 37

OPCPA Optical Parametric Chirped Pulse Amplification. 6, 57, 82

PPT Perelomov-Popov-Terent'ev. 22

PWA Plane Wave Approximation. 18

QPM Quasi-Phase Matching. 28

QRS Quantitative Rescattering. 30

Ra average surface roughness. 58, 59

RABBITT Reconstruction of Attosecond Beating By Interference of Two-photon Transitions. 92

RDW Resonant Dispersive Wave. 51, 103–105

RSME Root-Mean-Squared Error. 84

SAE Single Active Electron. 17, 24

SASE Self-Amplified Spontaneous Emission. 8, 79, 81, 84, 92, 96

SEM Scanning Electron Microscopy. 69

SFA Strong-Field Approximation. 17, 18, 21, 23, 27, 30, 31, 43

sHHG solid-state High-order Harmonic Generation. vii, ix, 7, 53, 54, 56, 58, 60–63, 69, 95, 96

SPIDER Spectral Phase Interferometry for Direct phase Retrieval. 8

SVEA Slowly Varying Envelope Approximation. 25, 31

TDSE Time Dependent Schrödinger Equation. 13, 17, 30

TL Transform-Limited. 86, 90, 107

UV ultraviolet. 35, 51, 57–60, 69, 103–105

VIS visible. 57, 69

VPR Vectorial Phase Retrieval. 73, 75, 76, 79, 88, 90, 92, 96

VUV vacuum-ultraviolet. 57, 69

XRD X-ray diffraction. 59

XUV extreme ultraviolet. 5, 37, 50, 96

List of Figures

List of Tables

PART I

Introduction

1 | From high-order harmonic sources to applications

From fundamental biological processes to advanced technologies, electron dynamics is central to how matter interacts with its surroundings. Electrons shape the properties of matter and determine how it responds to external stimuli such as light. The spacing between electronic energy levels spans from a few electronvolts to several kilo-electronvolts, which corresponds to characteristic timescales of electronic motion ranging from femtoseconds (fs) down to attoseconds (as), as illustrated in Figure 1.1 from Ref. [1].

Since its first demonstrations [2–4], High-order Harmonic Generation (HHG) has been recognized as a unique light source, combining the spectral range and temporal resolution required to map electronic motion. Over the past three decades, X-ray attosecond pump-probe spectroscopy schemes based on HHG [5–9] have been developed to capture electron dynamics at their natural time scale. These methods employ a pump pulse to initiate electron motion in a target, which is then interrogated by a delayed probe pulse. The experimental observable consists of changes in the optical properties (such as absorption or reflectance) or the emission of photoelectrons as a function of the time delay between the pump and probe pulses. The temporal resolution is dictated by the pulse duration, not by the electronics of the detector, a characteristic that enables real-time tracking of electron motion. Moreover, the developments in laser technology over the last two decades have made HHG sources in the soft X-ray spectral region increasingly accessible [10, 11]. Exploring electron dynamics in the soft X-ray spectral region (100 to 2000 eV) rather than in the extreme ultraviolet (XUV, 10-100 eV) offers access to core-electron dynamics [10, 12, 13], and the corresponding benefits of element selectivity and site specificity. In fact, in the soft X-ray region, each element in a system has a characteristic absorption spectrum that changes depending on its local environment. These aspects are particularly relevant to the study of large molecules in complex environments, *e.g.*, liquid solutions, since they allow for disentangling the contributions of each individual atom

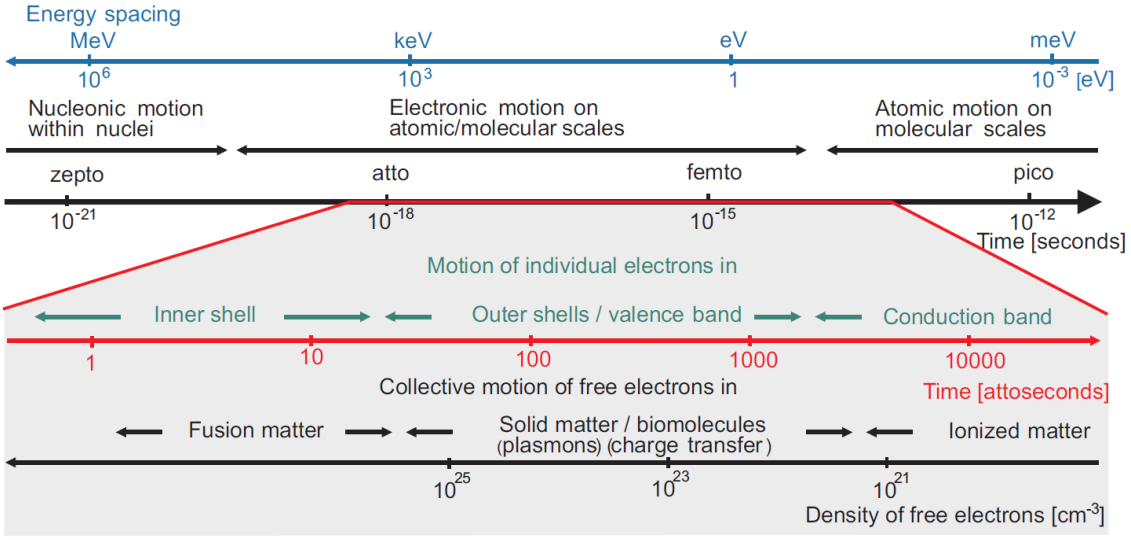

Figure 1.1: *Characteristic time scale of electronic motion in matter. Reproduced and reprinted with permission (Fig. 2) from [1]. Copyright (2025) by the American Physical Society.*

in the system. In particular, the so-called water window spectral region, ranging from the carbon K-edge ($\approx$ 290 eV) to the oxygen K-edge ($\approx$ 530 eV), provides a unique opportunity for element-specific studies in biological systems. In this range, water is transparent, while carbon- and oxygen-containing structures exhibit strong absorption features. For example, metallic complexes in solution are interesting model systems for studying charge-transfer processes, ligand-field effects, and solvation dynamics. Figure 1.2 illustrates the absorption spectra of iron and tellurium metallic complexes measured at the Elettra synchrotron in Trieste, Italy (proposal 20225477). The comparison of Te $N_{4,5}$, Fe $M_{2,3}$, and Fe $L_{2,3}$ edges shows an increasing contrast of the absorption features towards higher photon energies, highlighting the advantage of soft X-ray photons for mapping near-edge shifts induced by electronic processes such as charge transfer [14] or charge migration [15, 16].

Despite the advantages of high-photon-energy HHG sources, their application faces significant challenges due to their limited photon flux. Conventional HHG schemes covering the soft X-ray spectral region [17–19] are driven by high-intensity few-cycle driving pulses centred in the near-infrared (NIR) to mid-infrared (MIR), typically produced by Optical Parametric Amplification (OPA) and Optical Parametric Chirped Pulse Amplification (OPCPA) schemes, and interacting with high-pressure noble gases as targets. These features make the setups notably complex, while at the same time reducing their efficiency, which approximately scales as $\lambda^{-5.5}$ to $\lambda^{-6.5}$ [20, 21]. Nevertheless, they have allowed remarkable achievements, such as the study of sub-fs dynamics at conical intersections [22–24] and of the first steps of ionization dynamics [25–27], and the observation of the interplay between phonon and electron dynamics

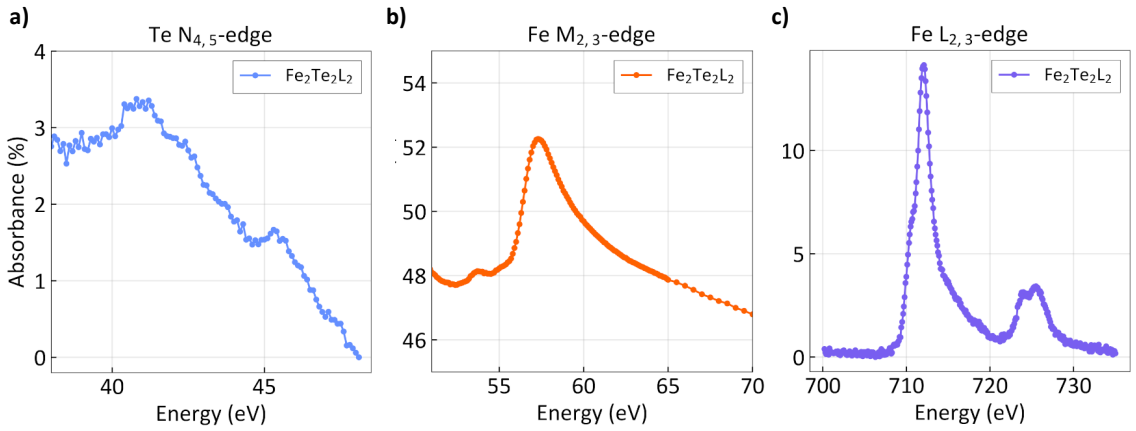

Figure 1.2: *Measured absorption spectra of iron-tellurium clusters. L_2 is a generic carbon-based ligand used to stabilize the complexes.* ***(a)*** *Te $N_{4,5}$,* ***(b)*** *Fe $M_{2,3}$, and* ***(c)*** *Fe $L_{2,3}$ edges.*

in graphite [28]. This thesis proposes an efficient alternative scheme for HHG at high photon energies, overcoming most of the technical challenges mentioned above. First, a theoretical introduction to HHG is reported in Chapter 2. The experimental development of a novel HHG source in the water window spectral region is then presented in Chapter 3. This scheme exploits the so-called *overdriven* regime [29, 30] with multicycle driving pulses at central wavelengths of 800 and 1500 nm. The regime is characterized by driving intensities in the order of 10^{16} W/cm^2 and interactions with the gas targets over sub-mm lengths. The challenges of gas confinement over these short distances have been addressed by designing a differentially-pumped glass chip similar to Ref. [31]. The experimental measurements show an extended photon energy emission towards the soft X-ray spectral region and are supported by three-dimensional propagation simulations. By utilizing the direct output of a commercial laser, this implementation significantly reduces the experimental complexities associated with soft X-ray generation, opening up new perspectives for simpler HHG schemes in both research and industry.

HHG is not only relevant as a source but also as a spectroscopic tool. The first spectroscopic experiments focused on molecular systems, as exemplified by Refs. [32–36]. They demonstrated that harmonic spectra encode information on the structural, nuclear, and electron dynamics initiated by the driving pulse, resulting in intensity modulations and interference features. From the first observation of HHG from bulk crystals [37], the concept of harmonic spectroscopy has been extended to solid samples. Analogously to the molecular case, solid-state High-order Harmonic Generation (sHHG) encodes information about the periodic potential, band structure, and symmetry of the crystal lattice, making it uniquely sensitive to valence electrons' dynamics governing the functional properties of materials [38–42]. Building on these

developments, Chapter 4 reports preliminary experimental results linking HHG emission from different TiO_2 phases to material ordering and spatial confinement. The results have the potential to establish a method for the tomographic reconstruction of the valence electronic potential - an important parameter for tailoring the material functionality.

In recent years, Free-Electron Lasers (FELs) have become increasingly relevant as an alternative to HHG sources in the high-energy attosecond temporal domain. FELs provide extremely high brilliance, yet attosecond pulse generation, characterization, and delay control require complex infrastructures. Several attosecond generation schemes have been proposed and are now operational and accessible to users [43–49]. Notable examples of experiments include mapping Auger-Meitner decay dynamics [50, 51], demonstrating both impulsive stimulated X-ray Raman scattering [52] and X-ray pump/X-ray probe transient absorption [53] in water, and few-femtosecond time-resolved diffraction imaging of Xe nanoparticles [54]. The characterization of FEL attosecond pulses commonly involves the ionization of a gas target, using techniques like plasma gating [55] or angular streaking [48, 56–58]. Alternatively, double-pulse schemes have been proposed, such as Spectral Phase Interferometry for Direct phase Retrieval (SPIDER) [59, 60], which is based on the interference of two equally intense FEL pulses, with precise calibration and control of their relative delay and spectral shearing. These approaches face technical challenges, including precise delay calibration, managing large data volumes, and advanced algorithms and machine learning for pulse reconstruction [61]. Additionally, essential requirements to reliably perform attosecond pump-probe experiments at FELs include sub-femtosecond delay control and single-shot pulse characterization to account for pulse-to-pulse variations caused by temporal jitter. The Double-Blind Holography (DBH) method presented in Chapters 5 and 6 aligns with these needs and has the potential to enhance FEL capabilities of performing attosecond experiments. DBH is a fully optical approach based on the linear interference of two unknown independent fields [62, 63]. In this case, a synchronized auxiliary HHG source has been used as an interfering field to reconstruct Self-Amplified Spontaneous Emission (SASE) FEL pulses delivered by FLASH2 (Hamburg, Germany) on a single-shot basis. Moreover, the interference maps obtained with this method directly encode information on the relative delay between the pulses. As such, this method can also be used as a delay tagging tool with sub-femtosecond precision.

In summary, this thesis reports novel schemes and applications of HHG sources. First, HHG is demonstrated as a source for investigating and controlling ultrafast electron dynamics in matter within the soft X-ray spectral region, utilizing an innovative

approach that overcomes the technical limitations of conventional long-wavelength-driven schemes. Second, the thesis demonstrates the potential of HHG as a spectroscopic tool for the reconstruction of the valence potential in bulk and semi-ordered materials. Finally, HHG is established as an auxiliary tool at FEL facilities for single-shot pulse characterization and delay tagging via DBH, thereby enabling new high-intensity spectroscopy experiments. Chapter 7 concludes with a summary of these results and a perspective on future developments and applications.

PART II

Novel schemes for High-order Harmonic Generation

2 | Fundamentals of High-order Harmonic Generation (HHG) in gases

This first part of this dissertation is dedicated to the design, development, and study of an efficient HHG source operating in the so-called *overdriven* or *nonadiabatic* regime. This first chapter presents an introduction to the theoretical models describing HHG, with particular emphasis on the parameters that lead to optimal generation conditions in the overdriven regime. This introductory chapter is essential for understanding the experimental results presented in Chapter 3.

2.1 Semiclassical model

HHG is a highly non-linear non-perturbative process that allows for the generation of short-wavelength attosecond pulses starting from a short and intense driving field in the NIR to MIR spectral region focused on a gas target [3, 4]. The process was first theoretically described through the Time Dependent Schrödinger Equation (TDSE) [64], which remains the most accurate method for describing harmonic generation. Nevertheless, different approximations and simplified models have been introduced in the last decades to provide a more intuitive explanation of the HHG process. Among these, in 1993, a semi-classical model called *three-step model* or *simple man model* was proposed [65–67]. In the first step, under the effect of the external driving field, the (atomic) gas undergoes ionization; secondly, the free electrons in the continuum are periodically accelerated and decelerated by the field, having a non-zero probability of finally recombining with the parent ion. When recombination occurs, the kinetic energy accumulated during electronic motion is released in the form of a burst of high-energy photons with sub-cycle duration. The emitted radiation can be described as the radiation emitted by an oscillating dipole, given by the coherent superposition of an oscillating component in the continuum (free electrons) and a

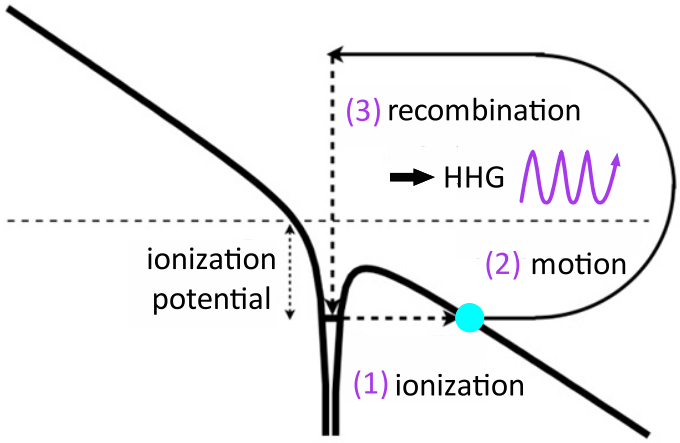

Figure 2.1: *Three-step model schematic representation. The process consists of a first step in which ionization occurs (here represented by tunneling ionization through a bent atomic potential in the presence of an intense external electromagnetic field), followed by electronic motion in the continuum, and concluded by the recombination and conversion of the electron's kinetic energy into emitted harmonic light. Adapted from [68] under the Creative Commons Attribution-NonCommercial-ShareAlike-3.0 License.*

component bound to the parent ion. A schematic of the three steps is reported in Figure 2.1 from [68]. The model is semi-classical, as the mechanism of ionization (tunneling, multiphoton, or above-barrier ionization) is purely described by quantum mechanics, while the electronic motion can be treated classically through Newton's second law. For symmetry reasons, the three steps are repeated at every crest of the driving field, *i.e.* every half optical cycle, thus leading to the generation of a train of attosecond pulses separated by half an optical cycle of the driving field, and to a comb of odd harmonics only. The typical spectral structure is characterized by intensity of the first few harmonic scaling perturbatively with the driving field, *i.e.* $\propto I^n$, where n is the harmonic order, followed by a so-called *plateau* region where the harmonic yield is roughly constant, and finally the so-called *cutoff* region where the yield drops to zero [69].

The classical description of electronic motion provides insight not only into electron trajectories but also into emission and recombination times, and thus into the released photon energy. Starting from a monochromatic driving field of frequency ω_0 and linearly polarized along x

$$\mathbf{E}(t) = E_0 \cos(\omega_0 t)\mathbf{u}_x \tag{2.1}$$

The second law of dynamics applies as

$$\ddot{x}(t) = -\frac{e}{m}\mathbf{E}(t) \tag{2.2}$$

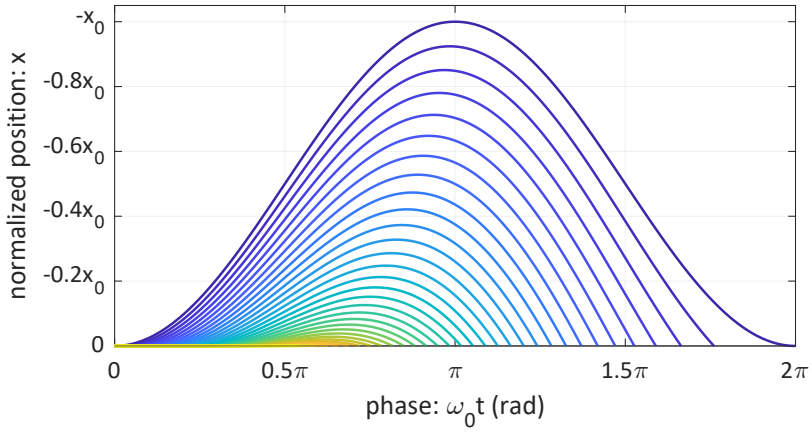

Figure 2.2: *Classical electron trajectories as per Eq. 2.3 calculated over one optical cycle for ionization phases $\omega_0 t'$ from 0 (blue) to $\pi/2$ (yellow) and with $x = 0$ the position of the parent ion.*

with e and m the electron charge and mass, respectively. Integrating the equation, the velocity and position of the freed electrons can be obtained, respectively, as

$$\dot{x}(t) = -\frac{eE_0}{m\omega_0}[\sin(\omega_0 t) - \sin(\omega_0 t')]\mathbf{u}_x \tag{2.3}$$

$$x(t) = \frac{eE_0}{m\omega_0^2}[\cos(\omega_0 t) - \cos(\omega_0 t') + \omega_0(t - t')\sin(\omega_0 t')] \tag{2.4}$$

where t' is the ionization time, with $\dot{x}(t') = 0$ and $x = 0$ the position of the parent ion. The instants of time t for which the equation $x(t) = 0$ is solved correspond to the recombination times. The equation can be solved numerically, and the solution can be fitted by the following analytical function

$$\omega_0 t = \frac{\pi}{2} - 3\arcsin\left(\frac{2}{\pi}\omega_0 t' - 1\right) \tag{2.5}$$

It is important to note that only the electrons freed at particular phases $\omega_0 t'$ can return to the parent ion. Figure 2.2 reports the trajectories calculated for $0 \leq \omega_0 t' \leq \pi/2$ over one optical cycle, the maximum round-trip an electron can have in the driving field obtained at $\omega_0 t' = 0$. From the conservation of energy, the photon energy released after recombination is given by the sum of the ionization potential I_p of the gas medium and the kinetic energy E_k accumulated by the electron during the motion:

$$\hbar\omega_X(t) = I_p + E_k(t) = I_p + \frac{1}{2}m\dot{x}^2(t) = I_p + 2U_p[\sin(\omega_0 t) - sin(\omega_0 t')]^2 \tag{2.6}$$

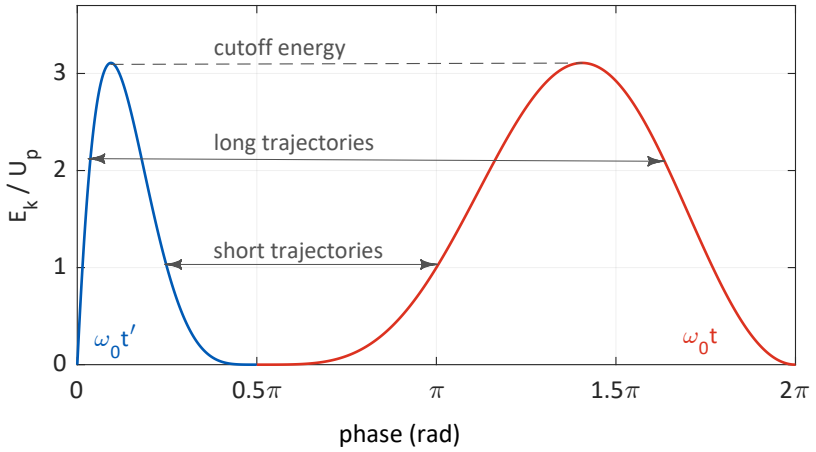

Figure 2.3: *Kinetic energy of the free electrons in the driving field normalized to the ponderomotive energy and plotted as a function of the ionization phase $\omega_0 t'$ (blue) and recombination phase $\omega_0 t$ (red). The maximum reachable energy is defined as the cutoff energy and is obtained for an ionization phase of approximately 0.1π (or $t' = 0.05T_0$). The same kinetic energy can be obtained for two different ionization times: one before the maximum energy at $0.05T_0$ and one after. This allows for categorizing the possible trajectories into two subgroups, called, respectively, long and short trajectories, as the sooner the electron ionizes, the later it recombines.*

with U_p the ponderomotive energy, *i.e.* the mean kinetic energy of an electron oscillating in a laser field, defined as

$$U_p = \frac{(eE_0)^2}{4m\omega_0^2} \tag{2.7}$$

With the use of Eq. 2.5, the kinetic energy $E_k(t)$ can be plotted (Fig. 2.3) both as a function of the ionization phase $\omega_0 t'$ (blue) and of the recombination phase $\omega_0 t$ (red). The maximum reachable energy, called *cutoff energy*, is obtained for an ionization phase of about 0.1π ($t' = 0.05T_0$) and corresponds to $\sim 3.17U_p$. Given this relation and the definition of ponderomotive energy (Eq. 2.7), the cutoff scales as $I\lambda_0$; therefore, when aiming at high cutoff energies, longer wavelengths and higher intensity are typically chosen. Figure 2.3 also shows that an electron released at $t' < 0.05T_0$ has the same energy as another electron released at $t' > 0.05T_0$. However, the electron released earlier will return later. For this reason, electron trajectories can be categorized as *long*, *i.e.* released before $0.05T_0$ and recombining within one optical cycle, and *short*, *i.e.* released after $0.05T_0$ and recombining in half an optical cycle. Moreover, since the ultimate kinetic energy depends on the return time, this leads to an intrinsic chirp in the generated attosecond pulses, referred to as *atto-chirp*. In fact, from the figure it can be observed that the degree of chirp, $d\omega_X(t)/dt \propto dE_k(t)/dt$, is positive for short trajectories, and negative for long ones.
Even though this semiclassical representation has some limitations, it still provides an intuitive picture of the HHG process that holds also under more complex scenarios.

2.2 Strong-Field Approximation (SFA)

Even though the three-step model provides an intuitive and effective description of the HHG process, the most accurate way of describing the single-atom response to a strong driving field makes use of numerical solutions to the TDSE. In 1994, Lewenstein *et al.* [70] proposed an approximate solution to the equation based on the so-called *Strong-Field Approximation (SFA)*. The approximation consists of assuming that the harmonic field is radiated by electric dipoles: the electron is treated as a free particle moving in the continuum around the stationary nucleus, neglecting any effect of the atomic potential and of bound states other than the ground state. Moreover, the Single Active Electron (SAE) approximation applies too, assuming that only one electron in the atom responds to the external driving field. Additionally, since the wavelength of the driving field is always much larger (hundreds of nanometers to a few microns) than the Bohr radius ($a_0 = 5.29 \cdot 10^{-11}$ m), the *dipole approximation* applies too: the driving field is considered spatially homogeneous, therefore only its time variation is taken into account. The TDSE can be written as

$$i\hbar\frac{\partial}{\partial t}\left|\psi(t)\right\rangle = \widehat{H}\left|\psi(t)\right\rangle \tag{2.8}$$

where the Hamiltonian $\widehat{H}$ is given by

$$\widehat{H} = \widehat{H}_0 + \widehat{H}' \tag{2.9}$$

with $\widehat{H}_0$ the unperturbed (laser-free) Hamiltonian of the atomic system

$$\widehat{H}_0 = -\frac{\hbar^2}{2m}\nabla^2 + V(\mathbf{r}) =_{a.u.} -\frac{1}{2}\nabla^2 + V(\mathbf{r}) \tag{2.10}$$

and $V(\mathbf{r})$ the effective SAE atomic potential. The perturbation Hamiltonian $\widehat{H}'$ in the dipole approximation is given by

$$\widehat{H}' = -\mu \cdot \mathbf{E}_L(t) = -q\mathbf{r} \cdot \mathbf{E}_L(t) =_{a.u.} -\mathbf{r} \cdot \mathbf{E}_L(t) \tag{2.11}$$

Based on the dipole approximation, the trajectory of the free electron is much smaller than the wavelength of the driving field; therefore, the spatial dependence of the vector potential is neglected. As a consequence, the effect of the magnetic field present within the electric pulse is neglected. Moreover, the SFA implies that, in the spatial region where the electron is accelerated by the driving field, the Coulomb potential of the atom is negligible with respect to the laser field itself. This means

that the effects of the atomic potential on the free electrons in the continuum are assumed to be small and are treated by using perturbation theory. The SFA model holds when the Keldysh parameter is $\gamma \ll 1$ and the photon energy of the dipole radiation is much larger than the ionization potential of the atom (see next Section). Moreover, the SFA assumes that the intense laser field promotes the ground-state electron directly to the continuum states, by-passing any other excited states (no resonance processes). This means that the electronic state $|\psi(t)\rangle$ representing the temporal evolution of the atomic system can be expanded on the basis set including only the ground state $|0\rangle$ and the continuum states $|\mathbf{k}\rangle$. The continuum states are approximated by a plane wave, *i.e.* Plane Wave Approximation (PWA). The ground state wavefunction is given by

$$|\psi_g\rangle = |0\rangle\, e^{-iI_p t/\hbar} =_{a.u.} |0\rangle\, e^{-iI_p t} \tag{2.12}$$

where $|0\rangle$ is the ground state function of a hydrogen-like atom. Its space-dependent part is

$$\langle \mathbf{r}|0\rangle =_{S.I.} \frac{1}{\sqrt{\pi}} \left(\frac{1}{a_0}\right)^{3/2} e^{-r/a_0} =_{a.u.} \frac{1}{\sqrt{\pi}} e^{-r} \tag{2.13}$$

The electron in the continuum can be described by the eigenstates of $\widehat{H}_0$

$$\widehat{H}_0\, |\mathbf{k}\rangle = \frac{k^2}{2}\, |\mathbf{k}\rangle \tag{2.14}$$

where $\mathbf{k}$ is the kinetic momentum of the outgoing electron. The wavefunction of the system can therefore be expressed as

$$|\psi(t)\rangle = e^{iI_p t} \left[a(t)\, |0\rangle + \int d^3k\, b(\mathbf{k}, t)\, |\mathbf{k}\rangle \right] \tag{2.15}$$

with $a(t)$ corresponding to the amplitude of the wavefunction of the ground state $|0\rangle$, which can be calculated from the ionization rate model of choice, and $b(\mathbf{k}, t)$ the amplitudes of the corresponding continuum states $|\mathbf{k}\rangle$, both ruling the temporal evolution of the system. Inserting 2.15 in 2.8 one obtains

$$\begin{aligned} \langle \mathbf{r}(t)\rangle = \langle 0|\mathbf{r}|0\rangle + \int d^3k\, b(\mathbf{k}, t)\, \langle 0|\mathbf{r}|\mathbf{k}\rangle + \int d^3k\, b^*(\mathbf{k}, t)\, \langle \mathbf{k}|\mathbf{r}|0\rangle \\ + \iint d^3k\, d^3k'\, b^2(\mathbf{k}, t)\, \langle \mathbf{k}|\mathbf{r}|\mathbf{k}'\rangle \end{aligned} \tag{2.16}$$

Using the notation of the dipole transition-matrix element from the ground state to the continuum states

$$\mathbf{d}(\mathbf{k}) = \langle \mathbf{k}|\mathbf{r}|0\rangle \tag{2.17}$$

$$\mathbf{d}(\mathbf{k})^* = \langle \mathbf{k}|\mathbf{r}|0\rangle^* = \langle 0|\mathbf{r}|\mathbf{k}\rangle \tag{2.18}$$

and ignoring the continuum-continuum contribution $\langle \mathbf{k}|\mathbf{r}|\mathbf{k}'\rangle$ as well as the static dipole moment $\langle 0|\mathbf{r}|0\rangle$, one obtains:

$$\langle \mathbf{r}(t)\rangle = \int d^3k\, b(\mathbf{k},t)\, \mathbf{d}^*(\mathbf{k}) + c.c. \tag{2.19}$$

The dipole elements have been extensively studied for atom-synchrotron interactions and are considered known elements of the equation. On the other hand, $b(\mathbf{k},t)$ is unknown, but can be rewritten considering the canonical momentum $\mathbf{p}$. Neglecting the effect of the Coulomb potential, the canonical momentum is constant during the interaction with the laser field, and it is classically defined as

$$\mathbf{p} = m\mathbf{v}(t) + q\mathbf{A}_L(t) =_{a.u.} \mathbf{v} + \mathbf{A}_L = \mathbf{k} + \mathbf{A}_L \tag{2.20}$$

where $\mathbf{A}_L(t)$ is the vector potential of the laser field, $\mathbf{E}_L(t) = -\partial\mathbf{A}_L(t)/\partial t$. Moreover, due to the conservation law of the canonical momentum, $\mathbf{p}(t') = \mathbf{p}(t)$, with t' the ionization instant and t any later time instant. The dipole moment in equation 2.19 can therefore be rewritten as

$$\langle \mathbf{r}(t)\rangle = \int d^3\mathbf{p}\, b(\mathbf{p},t)\, \mathbf{d}^*[\mathbf{p} - \mathbf{A}_L(t)] + c.c. \tag{2.21}$$

with $b(\mathbf{p},t)$ given by

$$b(\mathbf{p},t) = i\int_0^t dt' \mathbf{E}_L(t')\cdot\mathbf{d}[\mathbf{p} - \mathbf{A}_L(t)]e^{-iS(\mathbf{p},t,t')} \tag{2.22}$$

and $S(\mathbf{p},t,t')$ the classical action

$$S(\mathbf{p},t,t') = \int_t^{t'} dt'' \left(\frac{[\mathbf{p} - \mathbf{A}_L(t'')]^2}{2} + I_p\right) \tag{2.23}$$

in the end obtaining

$$\langle \mathbf{r}(t)\rangle = i\int_0^t dt' \int d^3\mathbf{p}\, \mathbf{d}^*[\mathbf{p} - \mathbf{A}_L(t)]e^{-iS(\mathbf{p},t,t')}\mathbf{E}_L(t')\cdot\mathbf{d}[\mathbf{p} - \mathbf{A}_L(t')] + c.c. \tag{2.24}$$

This is the final relation describing the dipole moment of an atom in time as a sum of probability amplitudes. These correspond to the following physical processes, which are closely related to the three-step semiclassical model:

1. $\mathbf{E}_L(t') \cdot \mathbf{d}[\mathbf{p} - \mathbf{A}_L(t')]$ describes the probability amplitude for an electron to ionize to the continuum at time t' under the effect of the driving field $\mathbf{E}_L$;

2. $e^{-iS(\mathbf{p},t,t')}$ describes the phase accumulated by the electron moving freely in the continuum with a constant momentum $\mathbf{p}$ from the time instant t' of ionization to the time instant t of recombination, with the kinetic energy of the electron expressed by the quasi-classical action S, accounting for some effect of the binding potential through I_p;

3. $d^*[\mathbf{p} - \mathbf{A}_L(t)]$ describes the probability of recombination at time t with the parent ion, thus leading to the generation of the XUV photons.

Equation 2.24 is typically solved through the so-called *saddle-point* method, which offers an approximated solution to the momentum integral by applying the Taylor polynomial expansion to the action $S(\mathbf{p}, t, t')$ near the point where it is stationary with respect to $\mathbf{p}$. Indeed, if the phase term oscillates rapidly with $\mathbf{p}$ with respect to the dipole element $\mathbf{d}$, its contribution to the integral is an oscillating function with zero average value, where the dominant contribution to the integral originates from the $\mathbf{p}$ values where the action is stationary, *i.e.* $\nabla_{\mathbf{p}} S(\mathbf{p}, t, t') = 0$. These assumptions reduce Eq. 2.24 to a time integral only, which is expressed as follows:

$$\langle \mathbf{r}(t) \rangle = i \int_0^\infty d\tau \left(\frac{\pi}{\epsilon + i\tau/2} \right)^{3/2} \mathbf{d}^*[\mathbf{p}_s(t,\tau) - \mathbf{A}_L(t)]\, e^{-iS(\mathbf{p}_s,t,\tau)} \cdot \\ \cdot \mathbf{E}_L(t-\tau)\, \mathbf{d}[\mathbf{p}_s - \mathbf{A}_L(t-\tau)] + c.c. \qquad (2.25)$$

with $\tau = t - t'$ the excursion time. The first factor $\left(\frac{\pi}{\epsilon + i\tau/2}\right)^{3/2}$ represents the quantum diffusion, *i.e.* the spreading of the returning electronic wave packet in the continuum, whose effect is to strongly reduce the efficiency of the successive recollisions, that are therefore neglected in HHG. The factor also contains the infinitesimal ϵ coming from the regularized Gaussian integration of the classical momentum $\mathbf{p}$ around the saddle point, introduced to eliminate the singularity in $\tau = 0$.
Moreover, from Eq. (2.23), $\nabla_{\mathbf{p}} S(\mathbf{p}, t, t')$ is nothing else but $x(t) - x(t')$, *i.e.* the difference between the position of the electron at time t, the recombination instant, and the position of the electron at time t', the ionization instant. This means that the stationary points of the classical action ($\nabla_{\mathbf{p}} S(\mathbf{p}, t, t') = 0$) correspond to those momenta $\mathbf{p}$ for which an electron freed at time t' returns to the same position at time

t, and therefore that the dominant contribution to the harmonic generation is given by electrons that recombine in the same position as they are generated.

2.3 Ionization models

As discussed in the previous sections, the single-atom modelling of the HHG process relies on the proper description of (1) the ionization, (2) the motion of the freed electron in the continuum from the instant of ionization to the instant of (3) recombination. The motion of the electron is described by the SFA and saddle-point method; however, in this formulation, a description of the ionization (and recombination) processes is still missing.

Using first-order perturbation theory, the photoionization probability for a single-electron atom undergoing a direct transition from the ground state to the continuum under a strong laser field, where the photon energy is much smaller than the ionization potential, can be directly derived. This forms the basis of Keldysh theory [71], which identifies two main ionization mechanisms under such conditions: *multiphoton* ionization and *tunnelling* ionization. The so-called Keldysh parameter, $\gamma = \sqrt{\frac{I_p}{2U_p}}$, helps identify which mechanism is dominant under the experimental conditions. In fact, for $\gamma \ll 1$, we are in the regime of tunnel ionization, while for $\gamma \gg 1$, the regime of multiphoton ionization applies. The tunnelling condition corresponds to a situation in which the Coulomb potential barrier can be considered stationary, *i.e.* the field applied is sufficiently strong to bend the potential barrier within a half laser cycle. On the contrary, multi-photon ionization describes a situation in which the Coulomb potential barrier is altered into an oscillatory potential by the external field, and ionization can happen only under non-linear photon absorption. The conditions under which $\gamma \approx 1$ cannot be purely described either by multiphoton absorption or tunnelling ionization. In this case, the ionizing field is strong enough to bend and modify the barrier, but not fast enough to consider the barrier static. Under these conditions, a third ionization regime named *above-barrier* ionization can be defined. It describes the situation in which the potential barrier is fully suppressed by the external field, and the electron can escape directly from the potential well without tunnelling. A schematic representation illustrating the difference between tunnelling and above-barrier ionization is reported in Fig. 2.4.

Considering the extremely high intensities required by HHG, the ionization step is typically dominated by tunnelling and above-barrier ionization regimes. The first can be well modelled by the so-called Ammosov-Delone-Krainov (ADK) model, from the names of its developers [72], or alternatively by the Perelomov-Popov-Terent'ev

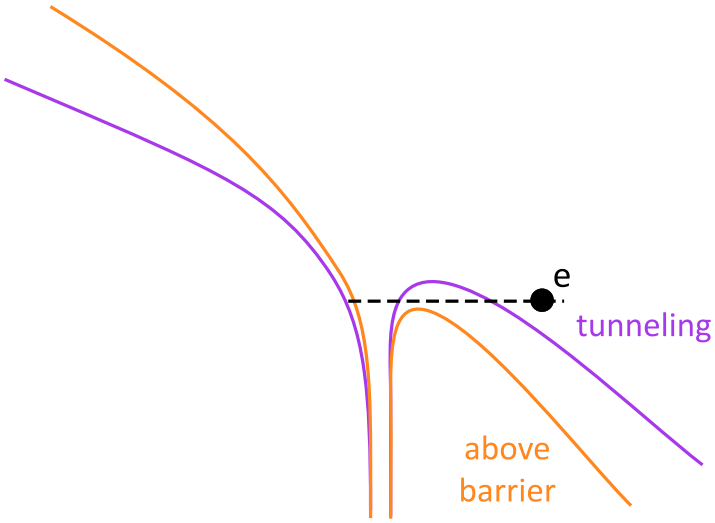

Figure 2.4: *Schematic of tunnelling (purple) and above-barrier (orange) ionization under the effect of a strong external field bending the atomic potential.*

(PPT) model [73], which is more broadly suitable to describe regimes for which $\gamma \leq 1$. In the limit of $\gamma \ll 1$, ADK and Perelomov-Popov-Terent'ev (PPT) models present identical expressions. The latter, instead, is accurately described only by the exact static ionization rates, which, however, are highly computationally demanding to calculate [74]. To overcome this complexity, several approximation or numerical methods have been developed in the years [75–79]. In the following, the focus will be on the ADK model, more widely used in the community due to its simpler expression. Subsequently, a modified version of the ADK model [79], capable of capturing the above-barrier ionization regime, will be presented.

2.3.1 Ammosov-Delone-Krainov (ADK) model

The ADK model is based on the assumption that the ionization event happens in a fraction of an optical cycle around the peaks of the driving field $E_L(t)$, so that the field can be treated as *quasi-static*. Moreover, it takes into account that the electronic states of the ionizing atoms are characterized by (1) the effective principal quantum number

$$n^* = Z_c \sqrt{\frac{I_{p,H}}{I_p}} \tag{2.26}$$

with Z_c the charge of the remaining atom, $I_{p,H}$ the hydrogen ionization potential (13.6 eV), and I_p the ionization potential of the atom, and (2) the effective orbital quantum number $\ell^* = n_0^* - 1$, with n_0^* the effective principal quantum number of the ground state. Before excitation, the electron is in a state defined by the quantum numbers

n, ℓ, m, respectively, the principal quantum number (or state), the orbital quantum number, and the magnetic quantum number. For an electron in an arbitrary bound state (n, ℓ, m), with $n^* \neq n$, the ADK ionization rate can be written as

$$w_{ADK_{lm}}(t, E_L) = \omega_p \left|C_{n^*l}\right|^2 \left(\frac{2\omega_p}{\omega_t}\right)^{2n^*-|m|-1} \frac{(2l+1)(l+|m|)!}{2^{|m|}|m|!(l-|m|)!} \exp\left(-\frac{2}{3}\frac{(2I_p)^{3/2}}{|E_L(t)|}\right) \tag{2.27}$$

where

$$\omega_p = \frac{I_p}{\hbar}, \quad \omega_t = \frac{e|E_L(t)|}{\sqrt{2m_e I_p}}, \quad |C_{n^*\ell^*}|^2 = \frac{2^{2n^*}}{n^*\,\Gamma(n^*+\ell^*+1)\,\Gamma(n^*-\ell^*)} \tag{2.28}$$

with m_e the electron mass.
When considering a single electron in the ground state ($n = 1$, $\ell = 0$, $m = 0$) subject to ionization, the expression simplifies into:

$$w_{ADK00}(t, E_L) = \omega_p \left|C_{n^*}\right|^2 \left(\frac{4\omega_p}{\omega_t}\right)^{2n^*-1} \exp\left(-\frac{4\omega_p}{3\omega_L}\right) \tag{2.29}$$

with

$$|C_{n^*}|^2 = \frac{2^{2n^*}}{n^*\,\Gamma(n^*+1)\,\Gamma(n^*)} \tag{2.30}$$

The ionization rate is introduced in the SFA representation as a weighting factor to the dipole moment in Equation (2.25) and it is expressed in the following form:

$$\exp\left[-\int_{-\infty}^{t-\tau} w_{ADK_{lm}}(t')dt'\right] \tag{2.31}$$

Additionally, the density of free electrons, an important quantity governing plasma effects along propagation in the medium (see Section 2.4), is expressed, in the case of first ionization only, as

$$n_e = n_0 \left\{1 - \exp\left[-\int_{-\infty}^{t-\tau} w_{ADK_{lm}}(t')dt'\right]\right\} \tag{2.32}$$

with n_0 the initial density of neutral atoms.

2.3.2 Empirically-corrected ADK (E-ADK) model

The exponential term in the ADK ionization rate in Eqs.(2.27) and (2.29) exhibits a strong dependence on the driving field amplitude and therefore on the intensity. It has been shown that, for high intensities in the order of 10^{15} to 10^{16} W/cm^2, the ADK model overestimates the actual ionization degree of the medium [76, 77]. In

particular, the threshold field amplitude for which the perturbation theory breaks down is $\sqrt{2I_p}/(16Z_c)$, with I_p the ionization potential, and Z_c the charge of the remaining atom. More accurate models are required to describe the above-barrier ionization regime. In Ref. [79], a simple exponential correction is presented as an alternative to handle these cases.

The correction is based on experimental observations; therefore, the model is generally referred to as the Empirically-corrected ADK (E-ADK) model. In this formulation, the ionization rate is expressed as follows:

$$w_{E-ADK}(t, E_L) = w_{ADK}(t, E_L) \exp\left[-\alpha \frac{Z_c^2}{I_p} \frac{E_L(t)}{(2I_p)^{3/2}}\right] \tag{2.33}$$

The notation follows the same adopted above, with the parameter α obtained by fitting the formula to the ionization rates calculated for a number of atoms and ions within the SAE approximation. The values are 9.0 for argon and neon, and 7.0 for helium. It is generally advised to use $\alpha = 6.0$ for electrons ionized from the s-wave and $\alpha = 9.0$ for ionization from the higher partial waves. With these values, the rate agrees within 50% of the numerically calculated ones [77], thus significantly improving the accuracy of the model. In the simulations performed in this work (see Sections 2.5 and 3.3), this factor has been taken into account, rewriting the ionization rate as

$$w'_{E-ADK}(t, E_L) = w_{ADK}(t, E_L) \frac{1}{2} \exp\left[-\alpha \frac{Z_c^2}{I_p} \frac{E_L(t)}{(2I_p)^{3/2}}\right] \tag{2.34}$$

finding a good agreement with the experimental results.

2.4 Macroscopic description of HHG: phase matching

The previous sections have focused on the single-atom description of HHG. However, the harmonic yield observed in experiments results from the macroscopic response of the medium. The total harmonic field is the coherent superposition of the fields emitted by all atoms in the gas target. Therefore, to accurately describe the HHG signal, one must solve the Maxwell wave equations for both the driving field and the harmonic field, where the single-atom response is used as a source term. To simplify the formulation, the time-dependent fields are typically expressed in radial coordinates (transverse axis, r) and propagate with cylindrical symmetry along the z-axis.

For the fundamental field, the equation is written as follows

$$\nabla^2 E_L(r,t,z) - \frac{1}{c^2}\frac{\partial^2 E_L(r,t,z)}{\partial t^2} = \frac{\omega_p^2(r,t,z)}{c^2} E_L(r,t,z) \tag{2.35}$$

with ω_p the plasma frequency defined as

$$\omega_p(r,t,z) = \left[\frac{e^2\, n_e(r,z,t)}{\varepsilon_0\, m_e}\right]^{1/2} \tag{2.36}$$

where $n_e(r,z,t)$ is the free-electron density defined by Eq. 2.32 (if necessary, modifying the expression of the ionization rate), and e, m_e are respectively the electron charge and mass, and ε_0 the vacuum permittivity. This expression accounts for plasma-induced effects on the fundamental beam, affecting both its phase, *i.e.* blue-shifting, self-steepening, and chirping, as well as its spatial properties, *i.e.* lensing and defocusing. The equation is generally solved in the moving coordinate frame ($t' = t - z/c$) and in paraxial approximation, *i.e.* neglecting $\partial^2 E_L/\partial z^2$.
For the harmonic beam, the wave equation is expressed as

$$\nabla^2 E_h(r,t,z) - \frac{1}{c^2}\frac{\partial^2 E_h(r,t,z)}{\partial t^2} = \mu_0 \frac{\partial^2 P_{nl}(r,t,z)}{\partial t^2} \tag{2.37}$$

where μ_0 is the vacuum magnetic permeability and P_{nl} is the non-linear polarization field generated in the gas medium and defined as

$$P_{nl}(r,t,z) = [n_0 - n_e(r,t,z)]\, d_{nl}(r,t,z) \tag{2.38}$$

with d_{nl} the dipole moment defined by equation 2.25 weighted by the ionization rate in 2.31. Both equations can be solved either using the Slowly Varying Envelope Approximation (SVEA), *i.e.* second order derivative is neglected, which, however, would not allow to capture the sub-cycle variations of the fields under the effect of strong plasma, or via calculation routines, such as the Crank-Nicholson [80], which averages close-neighbouring time steps to provide a more accurate solution.
Physical insights from these equations are obtained in the simplified case of a monochromatic and linearly polarized driving field, by applying the paraxial and SVEA approximations. Equation (2.37) simplifies as follows

$$\nabla_r^2 \tilde{E}_q(r) - 2ik_q \frac{\partial \tilde{E}_q(r)}{\partial z} = -\mu_0 q^2 \omega_L^2 \tilde{P}_q(r) e^{-i(qk_L - k_q)z} \tag{2.39}$$

with $E_q = \tilde{E}_q(r)\exp(-ik_q z)$ and $P_q(r) = \tilde{P}_q(r)\exp(-iqk_L)$, and the wave-vectors $k_q = n_q\omega_q/c$ and $k_L = n_L\omega_L/c$, with n_L and n_q the refractive indices of the gas

medium respectively for the fundamental frequency and q-th harmonic frequency of the fundamental. This equation explicitly defines the phase mismatch $\Delta k = qk_L - k_q$ between the harmonic field and the polarization field in the medium. The efficient generation of harmonics thus requires minimizing this phase mismatch. Typical phase contributions are: the dispersion from the neutral atoms Δk_n, the dispersion from the free electrons (plasma), Δk_e, the spatial or geometrical phase Δk_g, and the dipole phase Δk_d, *i.e.* the phase Φ accumulated by the freed electron in the continuum before recombining. When considering on-axis emission only ($r = 0$), the terms can be expressed as follows

1. *neutral atom dispersion*:

$$\Delta k_n = (n_L - n_q)\frac{q\omega_L}{c} \tag{2.40}$$

   Exploiting the definition of polarizability ($\alpha = 2\varepsilon_0(n-1)/\rho$, with ρ the density of gas), this term can be rewritten as:

$$\Delta k_n = \frac{q\omega_L}{2\varepsilon_0 c}(n_0 - n_e)(\alpha_L - \alpha_q) > 0 \tag{2.41}$$

   By approximating the polarizability at the fundamental frequency with the static one α_0 and considering that it is greater than α_q (polarizability of the q-th frequency) this term always contributes positively to the phase mismatch [81].

2. *plasma dispersion*:

$$\Delta k_e = -\frac{q\omega_L}{2\varepsilon_0 c}\frac{n_e e^2}{m_e}\left(\frac{1}{\omega_L^2} - \frac{1}{q^2\omega_L^2}\right) < 0 \tag{2.42}$$

   This term is negative by definition. The second term in parentheses can be neglected for higher orders.

3. *spatial phase*:

$$\Delta k_g = -\frac{qz_R}{z^2 + z_R^2} < 0 \tag{2.43}$$

   for free-space propagation of a Gaussian beam with z_R being the Rayleigh range and $z = 0$ corresponding to the position of the focus (Gouy phase), or in the case of guided geometry in a capillary

$$\Delta k_g = -q\frac{u_{nm}^2\lambda_L}{4\pi a^2} \tag{2.44}$$

with u_{nm} being a coefficient depending on the propagation mode in the capillary (e.g., for J_{11}, the Bessel function of the first kind and first order, $u_{11} = 2.4$), and a being the core radius of the capillary.

4. *dipole phase*:

$$\Delta k_d = \frac{\partial \Phi}{\partial I_L} \frac{\partial I_L}{\partial z} \tag{2.45}$$

where Φ generally indicates the phase cumulated by the electron in the continuum, which, within the SFA approximation, is expressed through the exponential of the action S (see eq. 2.24). To highlight the dependence on the on-axis propagation z, the dipole phase can be rewritten in the following form:

$$\Delta k_{\mathrm{d}} = -\frac{2z\beta_1(z)}{z^2 + z_R^2} \tag{2.46}$$

with $\beta_1(z)$ being an always negative coefficient depending on the ionization potential I_p, on the harmonic order q, on the electron trajectory and excursion time ($\tau \propto \lambda_L$), and, most importantly, on the intensity and position of the driving field $I_L(z)$ along the propagation axis. The sign of this term depends on the position with respect to focus, and it is positive for $z > 0$, *i.e.* medium after the focus.

As discussed in the next section, depending on the experimental configuration and geometry used for HHG, some terms can be neglected, while others become more significant. This description of phase matching can also be extended to off-axis, as in Ref. [82]. For example, this analysis has shown that non-collinear phase matching is obtained for points before the focus, $z < 0$. It is essential to note that Ref. [82] does not account for the temporal and spatial reshaping of the driving field, which can drastically alter the phase matching landscape, as it will be discussed in the following section for the overdriven regime.

2.4.1 Conventional regime, quasi-phase matching, overdriven regime: a comparison

The generation geometry and driving laser parameters dictate the regime of generation. As a consequence, schemes can be grouped under three categories: conventional, quasi-phase matching, and overdriven. This section presents the main characteristics and implementations of each category.

Conventional regime

The conventional regime is generally targeted through loose focusing geometries, for which the electric field varies slowly (or not at all, as in the guided geometry) along the propagation direction. Under these geometries, sub-cycle changes to the field and the corresponding free-electron density modulations are negligible. This regime of generation is also called *adiabatic* and typically features moderate to low intensities in the range of 10^{14} W/cm^2 and low ionization levels. Under these conditions, both the spatial phase (unless in guided geometry) and the dipole phase can be neglected. Perfect phase matching is then obtained when the neutral atom and free-electron phase contributions balance out. This condition corresponds to the so-called critical ionization level η_{cr}, which determines a critical driving intensity I_{cr} [83, 84]. The critical ionization degree is typically below 10%. The cutoff energy is therefore defined as $E_{\mathrm{cutoff}} = I_p + 3.17\,U_{p,cr}$, with $U_{p,cr} \propto I_{cr}\lambda_L^2$. Fig. 2.5 shows the cutoff energy in the conventional regime (dashed lines) calculated from [85] as a function of the driving wavelength for three noble gases generally used in HHG to cover the water-window spectral region: argon (Ar) in orange, neon (Ne) in purple, helium (He) in light blue. To reach photon energies exceeding 100 eV, these schemes rely on the use of high-intensity mid-infrared driving fields. However, this strategy comes at the expense of the harmonic yield, which scales as $\lambda_L^{-5.5}$ to $\lambda_L^{-6.5}$ [20, 21].

Quasi-Phase Matching (QPM)

From theory, the higher the intensity, the higher the harmonic order, but also the more rapid the phase slip between polarization field and harmonic field introduced by the propagation in the plasma. Under these conditions, Quasi-Phase Matching (QPM) schemes are often considered as alternatives. In QPM the phase mismatch is compensated along the propagation either by modulating the driving laser phase and intensity or the medium density [86–92]. This allows going beyond the conventional phase matching cutoffs reported in Fig. 2.5, but it comes at a price of a complex technical implementation, *e.g.* working with modulated guided media or multi-beam schemes.

Overdriven regime

The overdriven regime [29, 30, 85, 93–98] is defined by high intensities in the order of 10^{15} to 10^{16} W/cm^2 and a tight focusing geometry where the gas medium length significantly exceeds the Rayleigh range. Unlike in conventional high-harmonic generation setups, the tight focusing geometry introduces a pronounced dipole phase

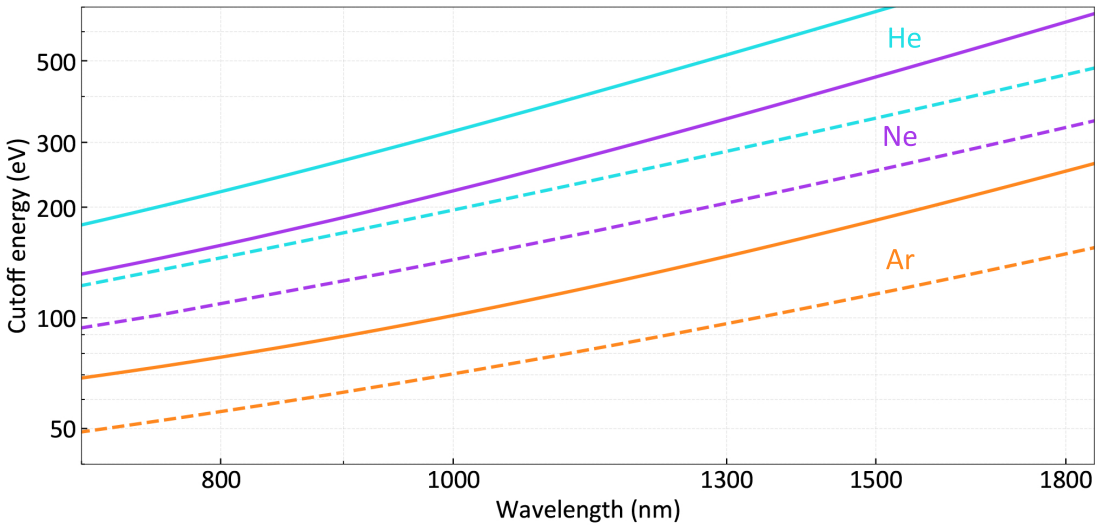

Figure 2.5: *Cutoff energy as a function of the driving wavelength (log-log scale) for the generation in argon (orange), neon (purple), and helium (light blue) in the overdriven regime (solid lines) and the conventional regime (dashed lines) as from Ref. [85], adapted under a Creative Commons Attribution NonCommercial License 4.0 (CC BY-NC).*

contribution ($\propto \nabla I_L(t, r, z)$) that can counterbalance the strong plasma contribution arising from the high driving field intensity. As the intense driver propagates through the highly ionized gas, it undergoes pronounced sub-cycle reshaping in time, frequency, and space [29, 30]. Rather than being a mere side effect, this reshaping plays a central role in the regime, transiently altering the generation conditions and enabling the extension of the harmonic cutoff. However, effective phase matching at these high energies can only be maintained over short distances (less than 1 mm), making gas confinement a key limitation in further extending the cutoff. Fig. 2.5 reports the theoretical expectations for the overdriven cutoff (solid lines) for Ar (orange), Ne (purple), and He (light-blue) as a function of the driving wavelength as modelled in [85].

In this regime, the phase matching is governed by plasma, dipole, and Gouy phases. Whilst the first is ruled by the field intensity and medium pressure, the latter two are strongly dependent on the medium position. For the Gouy phase, the farther it is from the focus, the smaller this contribution; for short interactions, it approaches its maximum value of $-q/z_R$, while the dipole phase remains positive only after the focus. Precise control of the medium position is therefore key to optimal phase matching. Moreover, the strong plasma reshaping prevents an accurate description of the beam as purely Gaussian, and its spatial phase cannot be merely defined as Gouy phase [99].

In the next chapter, experimental results in this regime will be presented and dis-

cussed together with simulations for different drivers and gas targets.

2.5 Simulation methods

HHG simulation methods involve a variety of models and approximations, most of which are reported in this chapter. The following list highlights the key aspects that can be used to categorize and compare these approaches:

1. *TDSE* vs *SFA*:
   Solving the TDSE implies a full calculation without approximations and can be highly computationally demanding. It is generally applied only for limited cases in which the SFA is considered not valid, *e.g.* when the intensity approaches relativistic regimes and magnetic effects are relevant, or when electron correlations or the effect of the Coulomb potential and other bound states are non-negligible. However, SFA is sometimes preferred even in these extreme scenarios, as the computational advantages it offers outweigh the benefits of a full TDSE calculation. To some extent, the inaccuracies of the SFA can be mitigated by a more refined ionization model (see case for high intensities) or by the use of complementary theories, such as Quantitative Rescattering (QRS) [100]. The latter models the recombination step using accurate scattering wavefunctions of the continuum states, thereby including the effects of the Coulomb potential and bound states. This model leads to a better representation of the HHG yield, especially at the plateau, allowing, for example, the simulation of the Cooper minima [101], which are generated by the structural destructive interference between the wavefunctions of the states involved in the photoionization.

2. *Ionization model*:
   As previously discussed, the ADK model is the most commonly used. Despite the approximations it involves, it still offers a good agreement between theory and experiment for most generation scenarios; however, it generally fails for high intensities at which barrier suppression occurs. Among the others mentioned in the previous sections, another relatively standard ionization model is the Yudin-Ivanov nonadiabatic tunnelling [102], which implements a time-dependent correction to the ADK model to handle the case of rapidly varying fields.

3. *Dimensionality*:
   In order to reduce the computational time and complexity of the simulations,

one-dimensional (on-axis) propagations are often considered-*e.g.* in Refs. [76, 96, 97]. Nonetheless, especially to capture spatial plasma-induced effects, three-dimensional models are generally adopted and implemented in cylindrical coordinates [80, 103–105].

4. *Re-absorption of the harmonic field*:
   Absorption is particularly relevant at low energies (< 100 eV), as it is the primary destructive mechanism affecting the harmonic yield; conversely, for higher energies, it plays a minor role. Generally the optimization of harmonic yield in conventional regimes requires adequate choice of the medium length based on the coherence length $L_{coh} = \Delta k^{-1}$ and the absorption length $L_{abs} = (n_0 \sigma_{abs})^{-1}$, with σ_{abs} the absorption coefficient of the medium. The optimal harmonic yield [106] corresponds to a medium length $L_{med} > 3L_{abs}$, and to a coherence length of $L_{coh} > 5L_{abs}$. For the overdriven regime, due to the strong spatio-temporal reshaping of the driving field, this description fails to represent the actual optimized conditions for efficient generation, as commented in the following chapter.

The simulation code adopted in this work is based on a modified version of the one used in Ref. [80]. The code, contrary to the SVEA, considers the full electric field in time (*nonadiabatic* representation) and its three-dimensional propagation in cylindrical coordinates (r,z). It employs the SFA with the E-ADK ionization model (corrected formula in Eq. 2.34) to better describe the barrier suppression ionization dominating at the high intensity (10^{16} W/cm^2) used in the experiments. This choice leads to a good match of the experimental results without the need to include contributions from multiple ionizations typically considered for similar experimental conditions [98, 103, 107, 108]. The propagation equations are solved in a split-step fashion, employing a Crank-Nicholson routine. The code includes also the re-absorption of the harmonic field in the gas-medium, applied to the harmonic electric field at each step of the propagation as a factor $\exp(-\frac{\Delta z}{2L_{abs}}) = \exp(-\frac{1}{2}\Delta z\, \sigma_{abs}\, n_0)$, with Δz the length of each step. The absorption coefficients have been calculated using the tabulated scattering factors (f_1, f_2) [109], first defining the refractive index $n_x = 1 - \frac{n_0\, r_e \lambda_x^2 (f_1 - i f_2)}{2\pi}$ at each energy, then the corresponding absorption coefficient $\sigma_x = \frac{4\pi\, \Im\{n_x\}}{\lambda_L\, n_0}$.
In the next chapter, both experimental results and simulations in the overdriven regime will be presented and discussed in detail, with support from the theory presented in this chapter.

3 | High-order Harmonic Generation in the overdriven regime

This chapter presents the experimental and simulation results for HHG in the overdriven regime with the ultimate goal of covering the soft X-ray spectral region between 200 and 500 eV. The experimental results presented here cover the generation with 800-nm and 1500-nm driving fields in Ar, Ne, and He. Each case has been fully optimized in driving intensity, pressure, and medium position to achieve efficient cut-off extension in the overdriven regime. The key aspects of this optimization will be discussed in detail in the following. Particular care has been taken in designing a differentially pumped chip for effective gas confinement. The details regarding its design and implementation are discussed in the first sections of this chapter, followed by the experimental results. Section 3.3 reports instead on the simulations performed with the code previously introduced in Section 2.5. The analysis focuses on the exemplary case of generation in neon with an 800-nm driving field. The analysis supports the experimental results, additionally providing key elements to fully understand the phase-matching dynamics in the overdriven regime.

3.1 Key aspects for optimal generation in the overdriven regime

As introduced in Section 2.4.1, once the tight focusing geometry is set and peak intensities on the order of 10^{16} W/cm^2 achieved, the key parameters to control HHG in the overdriven regime are (1) gas confinement, (2) pressure, and (3) medium position. Early works [29, 30] identified also the few-cycle duration of the driving field as a key requirement for accessing the overdriven regime. However, the experimental

results presented below indicate that this condition is not strictly necessary. On the one hand, the laser developments of the last couple of decades have enabled reaching high peak intensities even with multicycle pulses. On the other hand, a significant improvement in gas confinement capability and fine control of the inlet gas pressure have allowed the optimization of the process even with long pulses.
The strong reshaping that the driving field undergoes due to the high plasma density is key to efficient phase matching under overdriven conditions. However, an excessively long propagation in the ionized medium can be detrimental. Typical medium lengths are in the order of a few hundred microns. This makes gas confinement over short lengths crucial for efficient phase matching, with the ideal gas profile being a step function, where gas is present only at interaction with the laser focus and zero outside. More realistically, the gas profile is considered as a Lorentzian [18, 96, 110], including a gradual decrease at the edges. In this work, the challenge of achieving efficient gas confinement over short propagation distances was addressed by designing and adopting a differentially pumped chip similar to Ref. [31].
The other two critical parameters for phase matching, namely pressure and medium position, are finely tuned during the experimental optimization process. In the overdriven regime, the gas pressures are generally lower than in the conventional regime, in order to avoid excessive plasma generation, and the medium is located one to two Rayleigh lengths after the focus, so as to ensure a positive and sufficiently strong dipole contribution to balance out the plasma phase shift. All these aspects will be further discussed throughout this chapter based on experimental results.

3.1.1 Design of a differentially pumped glass chip for efficient HHG in the soft X-ray spectral region

The cell design is based on an on-chip differential pump scheme, thus miniaturizing often bulky and complex setups. It consists of a central channel where the gas is injected, and two symmetrical pumping stages (areas) directly connected to vacuum pumps. The chip is manufactured through the so-called *Femtosecond Laser Irradiation followed by Chemical Etching (FLICE)* technique [111–113], mastered and performed by our collaborators at CNR Milano, namely Dr. Rebeca Martínez-Vázquez, Prof. Roberto Osellame, and their team. Here, we adapted the design from [31] to optimize the generation of high photon energies in the soft X-ray spectral region between 100 and 500 eV. This implies shortening the interaction region, *i.e.* the region in which the gas has sufficiently high density and the driving laser sufficiently high intensity to generate harmonics, while also making the pumping more effective. The

final design is the result of a careful optimization of propagation channel lengths and diameters, as well as pumping areas, based on COMSOL Multiphysics simulations in the Free-Molecular Flow regime [114]. This regime is particularly suitable for describing low-pressure regions, while failing to accurately describe high-pressure volumes. In our case, we experimentally observed good agreement between the estimated pressure at the chip's output and the actual pressure measured in the vacuum chamber during generation. The main features of the newly designed chip are: (1) interaction channel (centre) of only 900 μm, with a diameter of 300 μm tapered at input and output to 200 μm, and (2) larger pumping areas of ca. 1 cm^2. The length and output diameters of the propagation channels have been carefully optimized to find a trade-off between pumping efficiency and gas confinement. Figure 3.1 reports the final parameters from the COMSOL sketch, where the illustrated volumes are etched from the bulk silica used as substrate for the fabrication of the chip through FLICE. The chemical etching phase of the fabrication resulted in an actual length of the interaction channel of 960 μm with an inner diameter of 300 μm, without tapering. These small modifications result in no impact on the simulation outcome. The chip has a total length of 41 mm and a thickness of 3 mm, made from a 2-mm-thick silica slab that is actually etched and covered on one side with an additional 1-mm-thick slab glued on top, resulting in a very compact design. The fabrication of the chip has been fully discussed in [115, 116]. With this configuration of parameters, introducing three vacuum pumps, two at 12 l/s pumping speed directly connected to the chip itself and one at 138 l/s pumping the chamber surrounding the chip, one obtains a pressure drop of four orders of magnitude between the gas injection point and the output, independently of the input pressure. The values closely match the experimental pressure measured in the vacuum chamber. Figure 3.2 reports the on-axis pressure along the chip when neon is injected at 250 mbar. Additional simulation outputs from the design process are reported in Appendix A.

3.1.2 Experimental setup

The development of this HHG source has been part of the optical design of a beamline for transient absorption spectroscopy of solvated molecules. The details of the beamline, its interferometer scheme, and the design of the ultraviolet (UV) pump arm are reported in App. B. In the following, this section will solely focus on the harmonic branch and on the performances of the differentially-pumped chip.
The chip performances have been tested using both the direct output of a commercial Carrier-Envelope Phase (CEP)-stable Ti:Sapphire laser at 1 kHz, 800 nm central wavelength and 30 fs Full-Width Half Maximum (FWHM) pulse duration

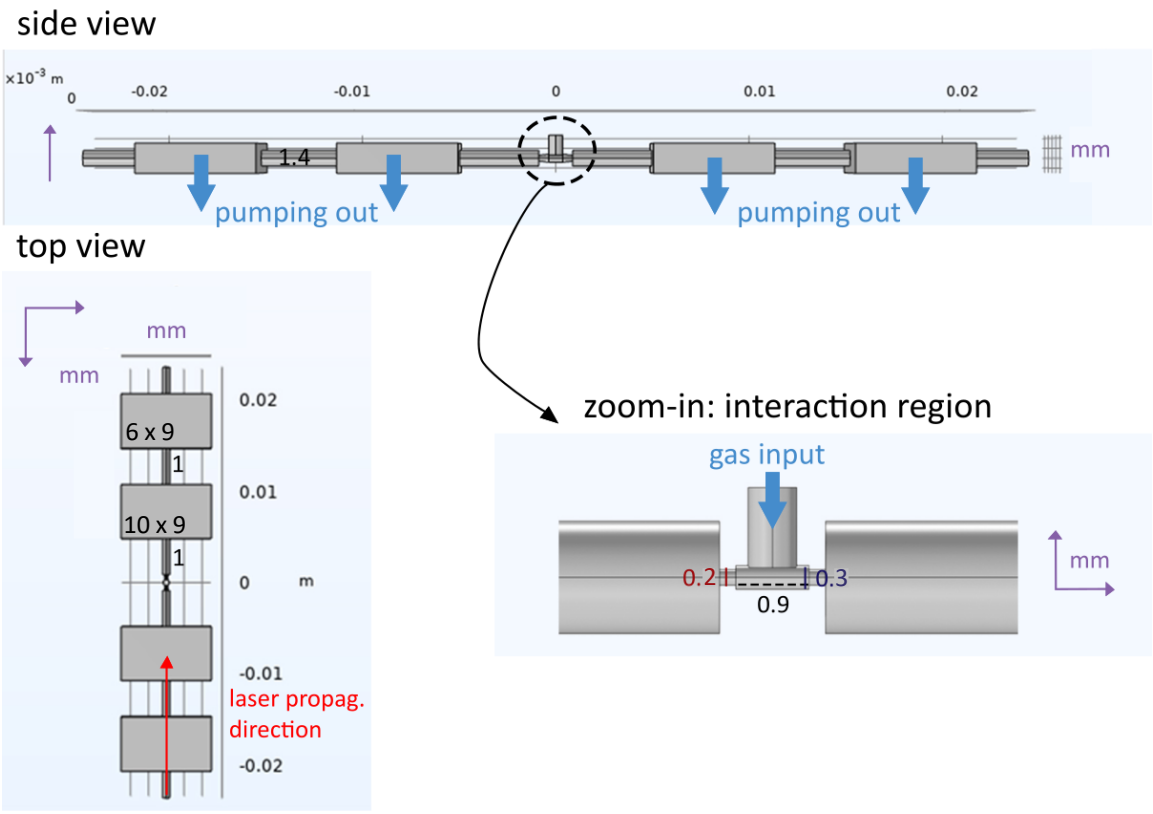

Figure 3.1: *Chip dimensions employed in the COMSOL Multiphysics simulation software. The total length of the chip is 41 mm and its thickness is 3 mm.*

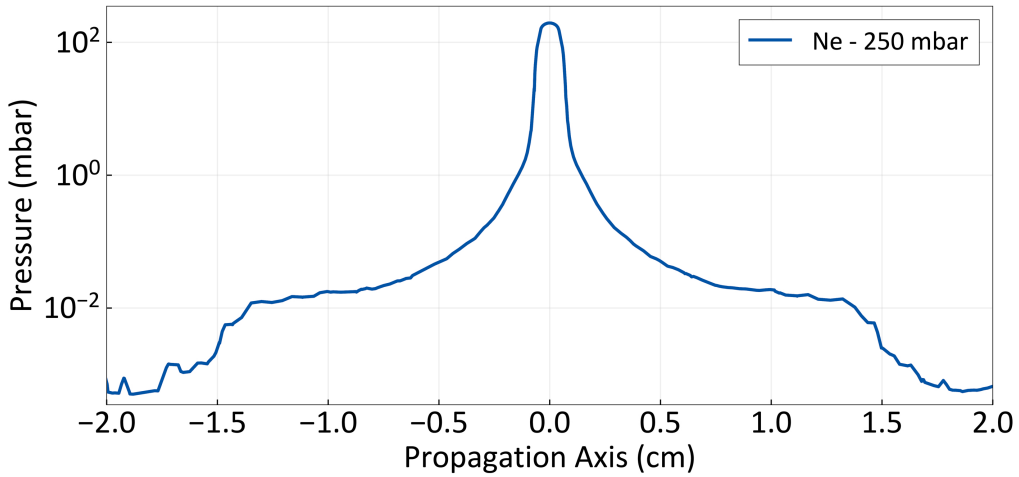

Figure 3.2: *Pressure profile along the differentially-pumped chip for the case of 250 mbar neon at input, when pumped by two vacuum pumps (12 l/s each) together with an additional pump for the chamber running at 138 l/s.*

(Femtopower), delivering up to 1.5 mJ at the generation point, and the output of a custom-built two-stages CEP-stable OPA [32] at 1500 nm central wavelength, with 30 fs FWHM pulse duration, providing up to 500 µJ at the generation point. The driving beams are tightly focused through the chip on the gas target using a 15 cm focal length lens (beam diameter at $1/e^2$ of 40 µm), resulting in a peak intensity of 0.8-1·10^{16} W/cm^2 and 4-5·10^{16} W/cm^2, respectively. Metallic filters (Al, Zr, In, 100–200 nm-thick films on Ni meshed grid, 15 mm aperture) can be optionally used to filter out the residual fundamental beam after generation. The harmonics are refocused in a 1:1 geometry (90 cm arm) through a toroidal mirror (15 x 130 mm), such as to allow the installation of an eventual sample target for further experiments (see Appendix B). The extreme ultraviolet (XUV) radiation is then dispersed through an aberration-corrected concave grating (Hitachi, central groove density 1200 grooves/mm, 5-25 nm wavelength range). The signal is collected using a chevron-stack of micro-channel plate (MCP) in combination with a phosphor screen (P43), followed by a Complementary Metal-Oxide-Semiconductor (CMOS) camera placed in air. The calibration of the spectrometer is based on geometrical considerations starting from the diffraction grating equation (order -1), knowing that the nominal angle of incidence (grazing) is 3°. An optimization of the angle of incidence is performed through least-squares minimization combining the information on the expected harmonic spacing ($2\omega_L$) and known filter edges, *e.g.* the Al $L_{2,3}$ edge at 72.5 eV. Planned upgrades to the setup include the installation of an additional aberration-corrected concave grating for high energies (Hitachi, central groove density 2400 grooves/mm, 1-6 nm wavelength range) and the replacement of the detection system with an X-ray Charge-Coupled Device (CCD) Camera (Andor Newton).

To achieve full control over the cell position with respect to the driving beam focusing, the cell is placed on a motorized stage with three translation axes and one in-plane rotation axis. The input pressure is finely tuned through a needle valve mounted in the gas line before the chip, providing control at the mbar level. In this scheme, optimal conditions are achieved with the medium placed approximately one Rayleigh length beyond the focus and at gas pressures of a few hundred millibars. Positioning the medium further downstream reduces the intensity below the threshold for effective overdriven generation, while higher pressures and shorter distances cause excessive ionization early in the medium, preventing phase matching and suppressing the harmonic yield at high photon energies. A schematic layout of the HHG setup is shown in Figure 3.3. The actual generation setup is instead reported in Figure 3.4: panel *a* shows the chip installed in its custom designed mount developed in-house with technical support, with the blue tube used for gas injection and the transparent

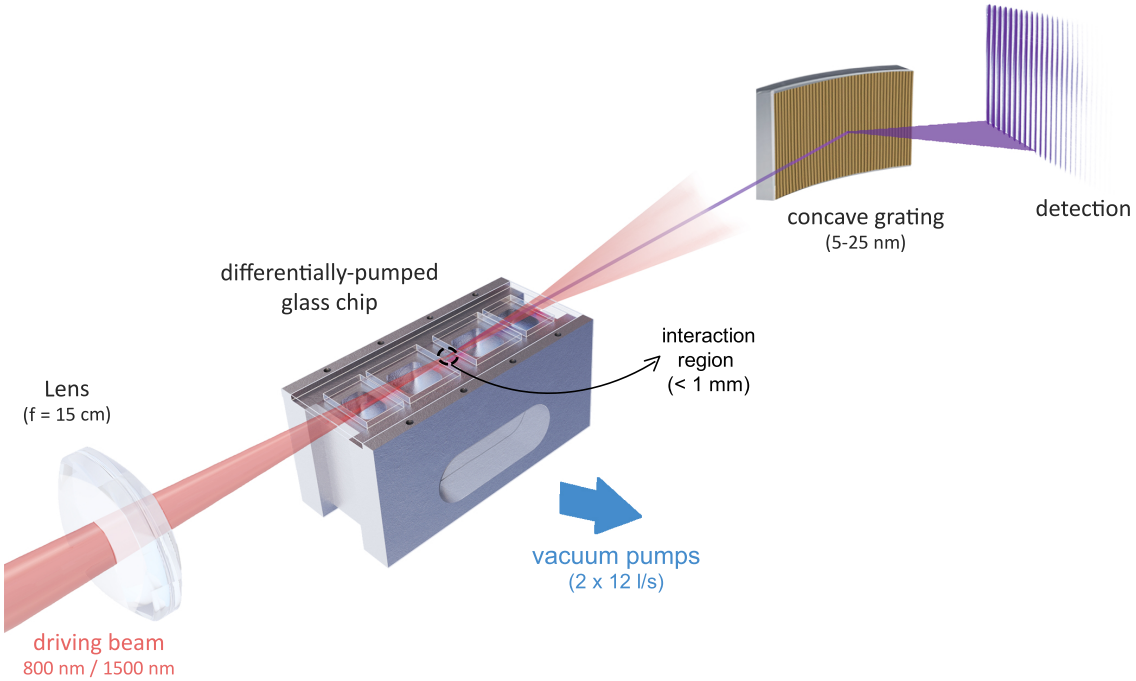

Figure 3.3: *Schematic layout of the HHG setup. Near infrared light (800 nm or 1500 nm) is tightly focused into the differentially pumped glass chip using a 15 cm lens, resulting i intensities in the order of 10^{16} W/cm^2. The harmonic field is then refocused by a toroidal mirror (not shown), and the HHG radiation is ultimately dispersed at the detector via an aberration-corrected concave grating.*

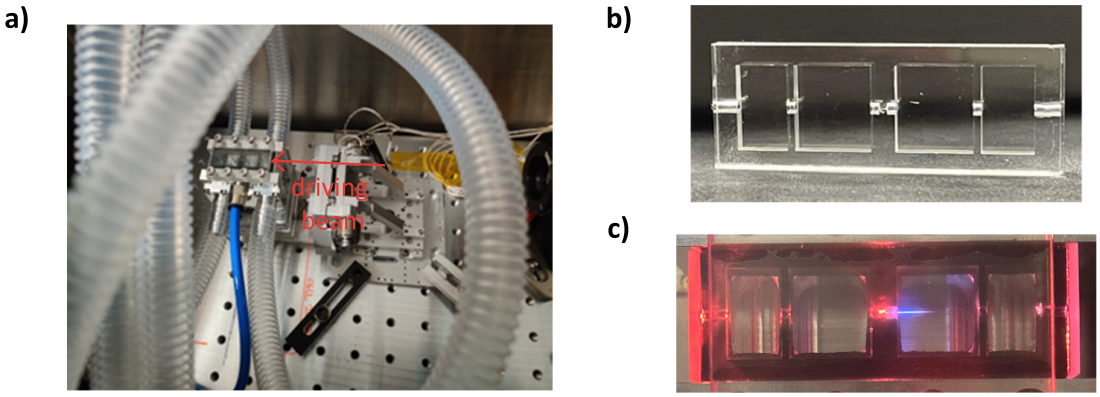

Figure 3.4: ***(a)*** *Chip installed on a custom-designed mount holder. The blue tube is the gas inlet connected to the centre of the chip, whilst the transparent tubes (12 mm inner diameter) are connected to the vacuum pumps. The holder is a custom mount developed in-house with technical support.* ***(b)*** *Chip after fabrication, total length 41 mm, thickness 3 mm.* ***(c)*** *Top-view of the chip during the generation in argon (200 mbar) with plasma generated at the entrance of the interaction region (the driving beam is coming from the right).*

tubes (12 mm inner diameters) used for pumping; panel *b* shows the top-view of the chip out of fabrication; and panel *c* shows the chip during the generation in argon with 800-nm (laser is entering from the right) where the plasma is shifted downstream with respect to the interaction region.

3.2 Experimental Results

Harmonic spectra generated in argon (top), neon (middle), and helium (bottom) with either the 800-nm (panels *a-c*) or the 1500-nm (panels *d-f*) driving field are reported in Figure 3.5. The full spectra are obtained by stitching separate images acquired at different positions of the detector. In some cases, a mild smoothing has been applied to mitigate artifacts arising from the stitching procedure at the image boundaries. The optimal gas pressures are reported for each case in the legends of the figure, and range from 200 to 1800 mbar. This is consistent with the values reported in [85, 93, 98], but contrasts with other works reporting pressures in the order of bars [94, 95]. As in similar cases, a further increase in pressure worsens the phase matching, thus producing less extended and less brilliant spectra. We define the cutoff energy as the photon energy at which the HHG intensity decreases to 1% with respect to its maximum, *i.e.*, plateau. In all media, the spectra span an energy range almost two times as broad as in the conventional regime, indicated by the shaded areas in Figure 3.5 panels *a-f*. For the 800-nm driver, the highest increases are obtained in argon and neon, whilst the performances in helium are very similar to those in neon. The HHG source driven with 800-nm pulses in argon and neon has also been characterized in terms of flux. Experimentally, the condition yielding the maximum cutoff extension does not coincide with the condition of maximum brilliance. The spectra presented here have been obtained by solely maximizing the cutoff energy; however, further optimization of the gas pressure and medium position could enable a trade-off between cutoff extension and brilliance. For argon, at maximum cutoff extension, the total pulse energy is 6.5 pJ, corresponding to $6.8 \cdot 10^8$ photons/s at a central energy of 60 eV within the 50-70 eV range. For neon, at maximum cutoff extension, the pulse energy is 0.3 pJ, corresponding to an average of $1.1 \cdot 10^7$ at a central energy of 150 eV within the 50-200 eV range. These values underestimate the total flux of the source, as the toroidal mirror did not accommodate the beam's full vertical extent. It is therefore expected that the actual flux could closely match the values reported in literature for similar cases [30, 98].

The HHG spectra obtained with the 1500-nm driving field are characterized by a small contrast between consecutive harmonics, forming a quasi-continuum (Fig. 3.5d-

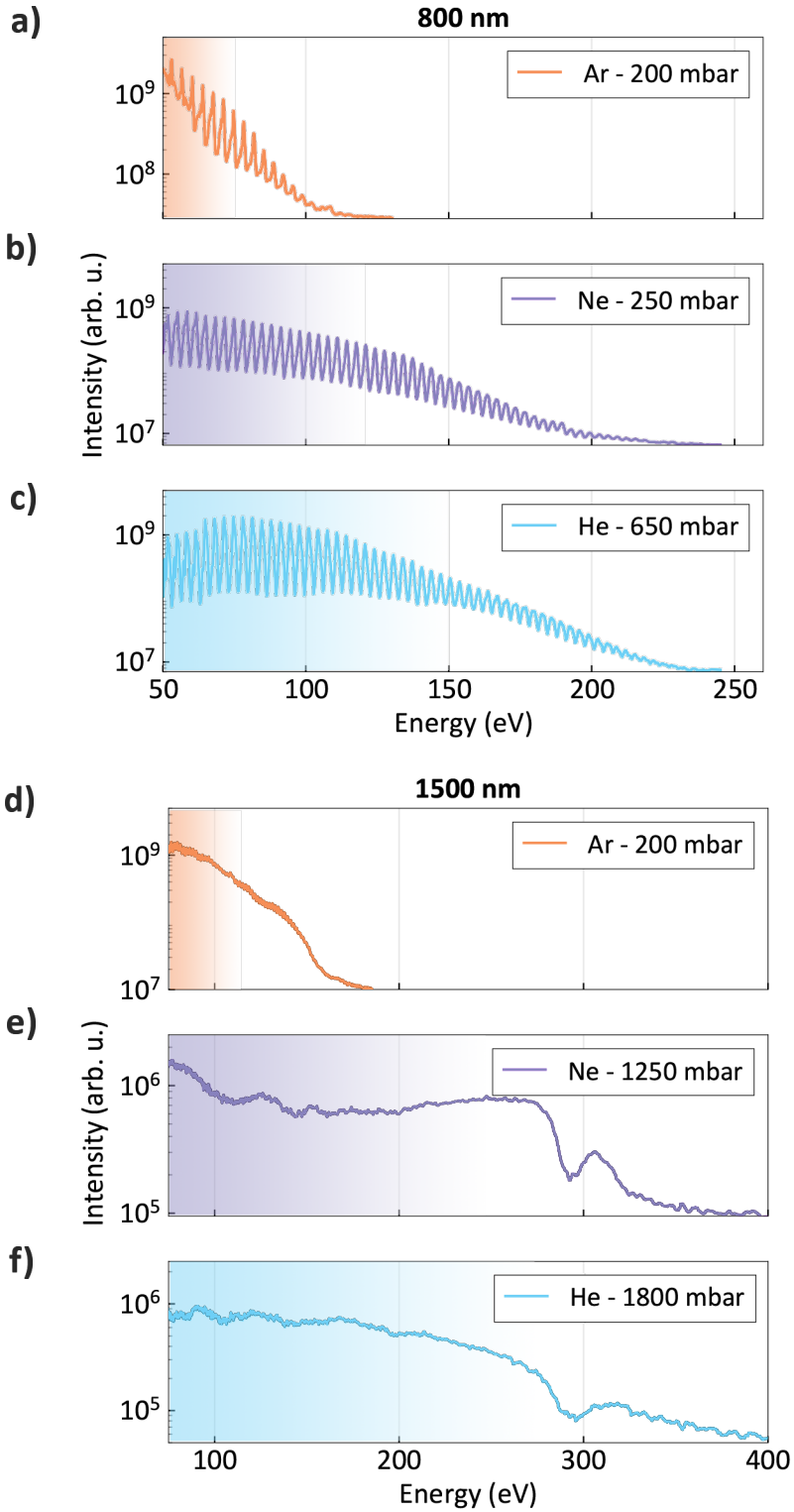

Figure 3.5: ***(a-f)*** *HHG spectra obtained in Ar (orange), Ne (purple), and He (light blue) with 800 nm (left) and 1500 nm (right) driving fields. The optimal pressures range between 200 and 1800 mbar and are indicated in the legend labels. The shaded areas indicate the expected cutoff in the conventional regime (see dashed lines in Fig 2.5). All the cases exhibit an extension of nearly a factor of 2 compared to the conventional regime.*

e). HHG with longer-wavelength drivers is characterized by longer electron excursion times, inducing stronger dipole phase contributions that favour long trajectories, combined with a higher degree of ionization resulting from the longer driving cycles, which in turn induce even stronger sub-cycle temporal reshaping. These effects prevent the emission from different half-cycles from rephasing coherently in the frequency domain, leading to spectral smearing and the appearance of a quasi-continuum spectrum [11, 117]. The spectra in neon and helium exhibit an absorption feature around 285 eV, corresponding to the C K-edge, which is attributed to carbon contamination of the beamline optics. Moreover, their measured cutoff was limited by the spectrometer grating geometry. In fact, the grating used allows for the efficient detection of spectral components up to 250 eV [118]. Higher energies (up to 400 eV) can still be measured, but they are strongly affected by decreased sensitivity be. If higher photon energies were recorded, most likely the cutoff would extend even further, as only a $\sim$10% decrease relative to the intensity maximum is observed. These results indicate the possibility of entering the water window without the need of using driving fields of 1800 nm or even longer wavelengths, so far privileged in the literature [17–19, 119], making it accessible even with standard out-of-the-box laser systems.

Recalling Fig. 2.5, the same overview of the cutoff energies as a function of the driving wavelength in argon, neon and helium for both conventional and overdriven regimes is reported in Figure 3.6 together with these experimental results (diamonds) and relevant literature data (circles) [17, 18, 85, 93–96, 119]. In all cases, our generation conditions largely exceed the cutoff energies of the conventional regime, and either match or even surpass the expected values for the overdriven regime at 800 nm by 25 to 50%, reaching 120 eV, 225 eV and 240 eV for Ar, Ne, He, respectively. In particular, the 800 nm spectral cutoff in argon is the highest ever reported in literature, while neon and helium reached extended cutoffs similar to Ref. [93], where the authors though employed few-cycle pulses. In this respect, this work demonstrates the notable advantage of exceeding 200 eV using the direct output of the Ti:Sapphire laser (30 fs), which significantly simplifies the generation scheme for these photon energies. These results also demonstrate that the overdriven regime does not imply strong constraints on the temporal duration of the driver, contrary to what was initially reported as a strict requirement from theory [29, 30].

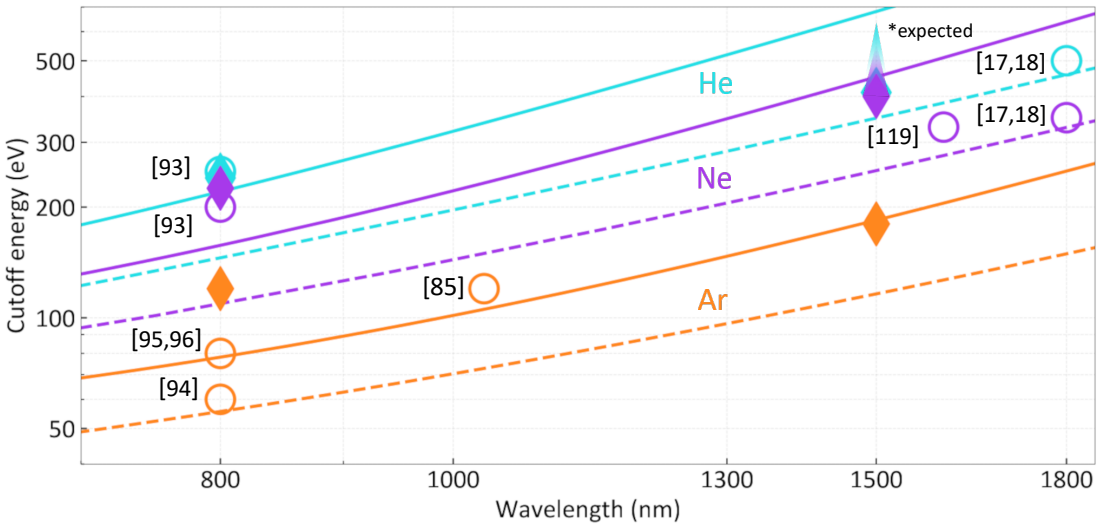

Figure 3.6: *Theoretical curves (log-log scale) of the cutoff energies as a function of the driver laser wavelength in Ar (orange), Ne (purple), and He (light blue) in the conventional (dashed lines) and in the overdriven regime (solid lines) from Ref. [85]. The circles mark the cutoff energies reported in literature, while the diamonds represent the results obtained in the current work. The markers for He and Ne with the 1500 nm driver underestimate the actual cutoff (see main text) and are reported as shaded areas towards higher energies to indicate the expected values. Figure adapted from Ref. [85] under a Creative Commons Attribution NonCommercial License 4.0 (CC BY-NC).*

3.3 Simulation Results

Parameters	
distance focus-medium z_0	-900 µm
medium length z_{max}	900 µm
spot size (focus) w_0	20 µm
Rayleigh range z_R	1.5 mm
FWHM duration	30 fs
field amplitude	0.5338 a.u.
number gas density	$9{\cdot}10^{-7}$ a.u.

Table 3.1: *Input parameters for the simulations of the harmonic generation in neon with 800-nm driver;* a.u. *stands for atomic unit. The field parameters correspond to an intensity at focus of ca. 10^{16} W/cm^2. The number gas density reported corresponds instead to 250 mbar at ambient temperature. The medium is located 900 µm* after *the focus of the beam, corresponding to approximately two-thirds of the Rayleigh length.*

The simulations performed with the code illustrated in Sect. 2.5 are key to the understanding of the phase matching dynamics in the overdriven regime. A wide range of parameters, namely gas species, driving wavelength, medium length, and position, have been explored to confirm the robustness of the model. The following

text will focus on the generation in neon with an 800-nm driver. The observations derived for this case can be extended without loss of generality to other cases. Table 3.1 reports the parameters used in the simulation, where *a.u.* stands for atomic unit and z is the laser propagation direction with 0 at the entrance of the medium, *i.e.* a negative distance focus-medium means that the medium is placed after the laser focus. The gas profile is considered constant along the whole propagation. What is crucial in assessing the correct description of the overdriven regime is the driving field spectral, temporal, and spatial reshaping due to plasma, together with the cutoff extension of the harmonic field. These aspects are fully captured by the simulation. In fact, Figure 3.7a reports the integrated harmonic spectral intensity over the radial coordinates, showing a cutoff of more than 250 eV, closely matching our experimental observations. Notably, the use of SFA leads to an inaccurate estimation of the intensity up to a factor of ten [76]. Panels b and c in the same figure report, respectively, the driving field spectral intensity at the entrance and the exit of the medium as a function of the radial coordinate, showing a pronounced blue shift of the field and overall defocusing. Finally, panel d shows the on-axis driving field temporal profile at the entrance (red) and end (blue) of the medium, highlighting the self-steepening of the field and its chirping.

In the framework of the overdriven regime, understanding the spatial dependence of the harmonic field is crucial. Figure 3.8 shows the squared modulus of the harmonic field at the end of the medium as a function of the radial coordinate. From this plot, the cutoff extension is happening only at specific radial coordinates, namely between 5 and 15 µm. This provides insight into the off-axis dynamics of phase matching. More details on this aspect are retrieved through Gabor analysis in the following Section 3.3.1.

Further observations regarding the phase matching length can be instead made starting from Figure 3.9a, which reports the harmonic spectrum integrated over the radial coordinate as a function of the propagation distance z. Lower photon energies ($<$ 100 eV) experience an intensity increase throughout the entire propagation, whereas higher photon energies saturate early in the medium, without, however, experiencing significant reabsorption. Figure 3.9b reports the line cuts of the harmonic intensity for three selected energies in the cutoff region, namely 180, 200, and 220 eV. From this plot, the higher the photon energy, the earlier the saturation is reached, with differences in the order of tens of microns, as indicated by the vertical dashed lines. Lower energies reach saturation only later in the medium and are then strongly affected by reabsorption. Figure 3.10a reports for the same generation conditions of Table 3.1 the integrated harmonic spectral intensity over an extended propagation

of 2700 µm, with intensity line cuts (panel *b*) corresponding to 80, 100, and 120 eV. Intensity saturation is reached for propagations longer than 1 mm, whilst the reabsorption reduces the final yield of these photon energies by almost an order of magnitude.

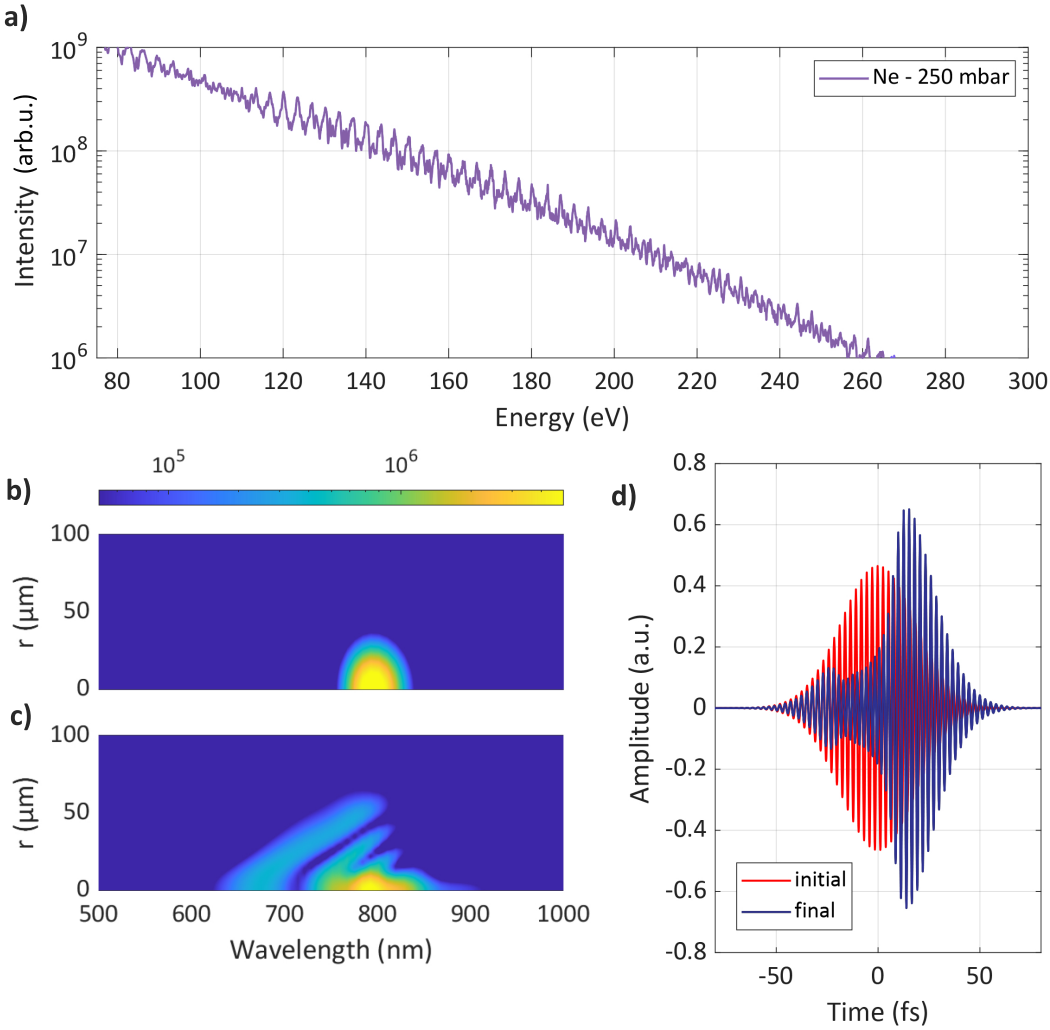

Figure 3.7: *Simulated three-dimensional space generation and propagation of the 800 nm driving field and HHG field in Ne.* ***(a)*** *Integrated harmonic spectrum over the radial coordinate.* ***(b),(c)*** *Spectral intensity (squared module) of the driving field, respectively, at the beginning, and at the end of the propagation medium as a function of the radial coordinate r and the driving wavelength.* ***(d)*** *On-axis (r=0) temporal amplitude of the driving field at the beginning (red) and at the end (blue) of the propagation medium.*

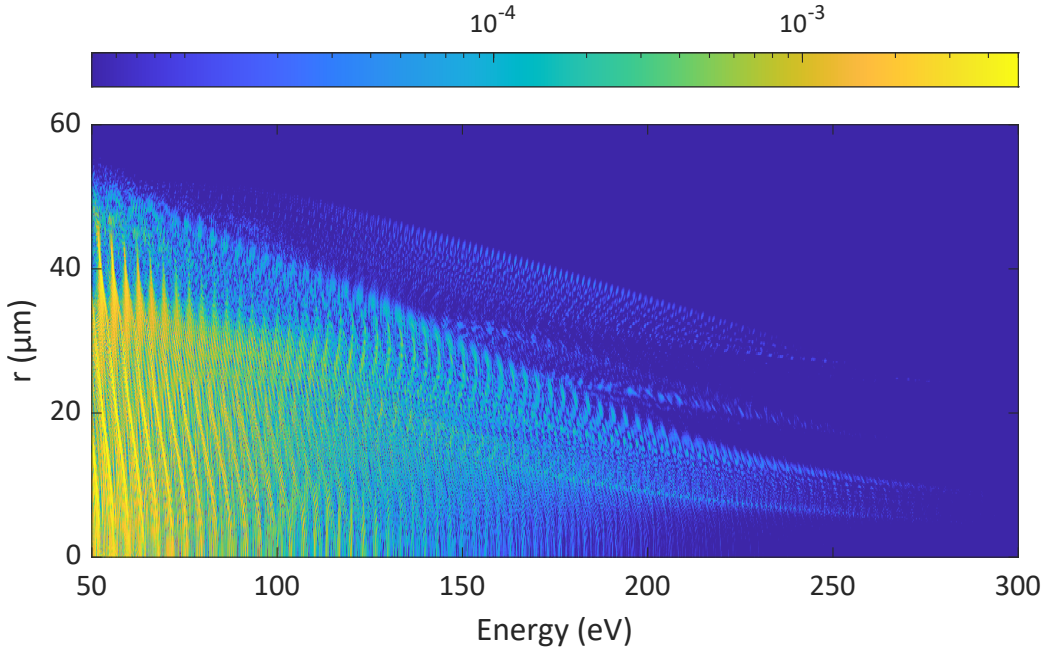

Figure 3.8: *Squared modulus of the HHG spectral amplitude (a.u.) at the end of the gas medium as a function of the radial coordinate and photon energy. The high-energy extended cutoff typical of the overdriven regime is confined to radial coordinates between 5 and 15 μm.*

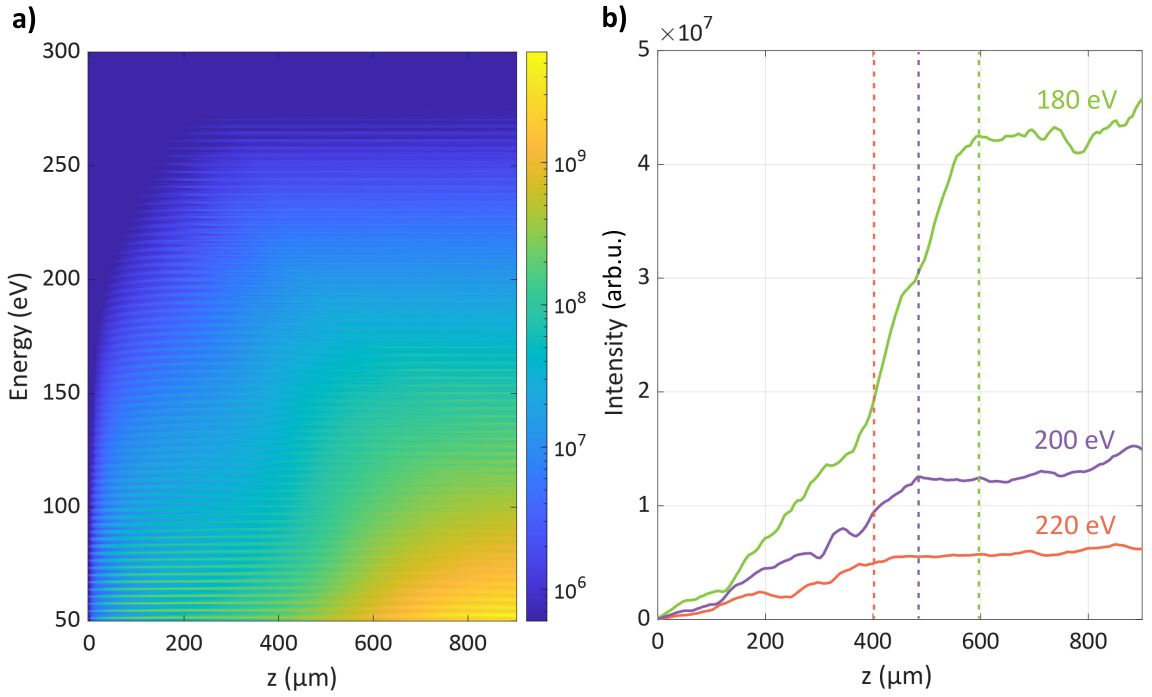

Figure 3.9: ***(a)*** *HHG spectral intensity (arb.u.) integrated over the radial coordinate as a function of the propagation (900 μm) in the gas medium.* ***(b)*** *Intensity line-cuts at energies 180 (green), 200 (purple), and 220 (orange) eV as a function of the propagation distance in the medium. Intensity saturation (vertical dashed lines) is progressively reached at shorter propagation distances, with higher HHG photon energies.*

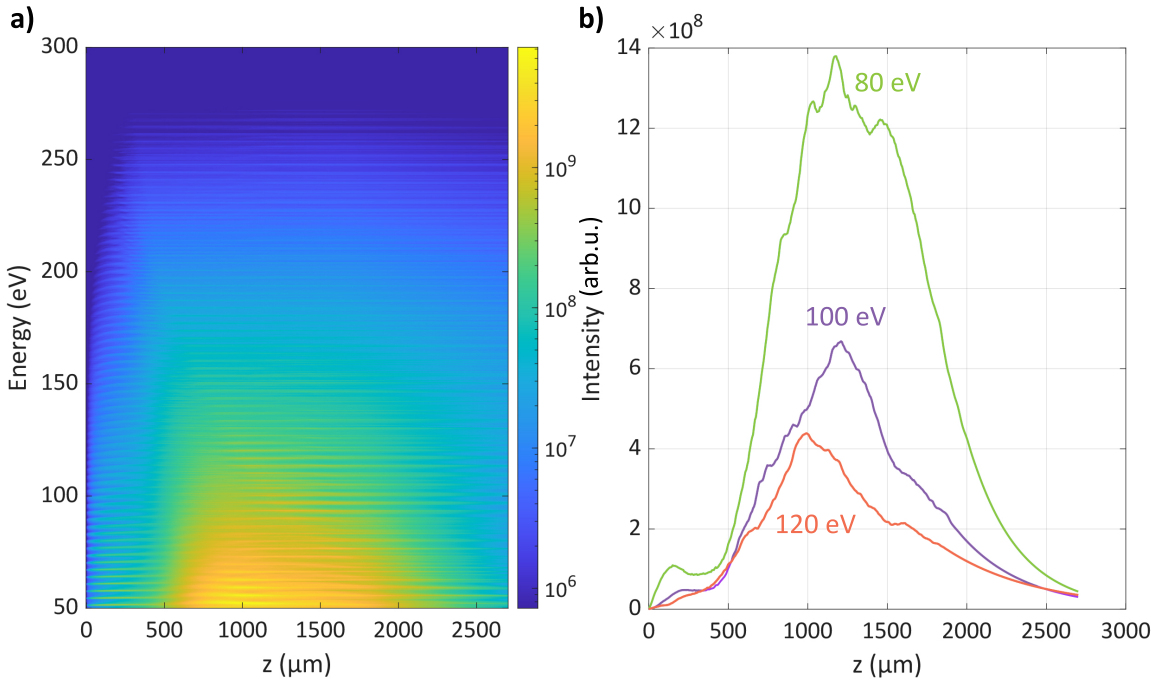

Figure 3.10: ***(a)*** *HHG spectral intensity (arb.u.) integrated over the radial coordinate as a function of the propagation (2700 μm) in the gas medium.* ***(b)*** *Intensity line-cuts at energies 80 (green), 100 (purple), and 120 (orange) eV as a function of the propagation distance in the medium. Intensity saturation (peak) is reached after more than 1 mm of propagation, then the final yield is affected by reabsorption, which reduces it by almost an order of magnitude.*

3.3.1 Gabor analysis

To further investigate the temporal and spatial dynamic dependence of the extended cutoff generation, a Gabor analysis [120] of the harmonic spectra has been performed. Following the procedure in [121], this analysis allows for determining the energy content of the harmonic field evolving in time. Additionally, this information can be combined with the evolution along the propagation direction and the radial coordinate.

In this work, the gating function has been chosen as purely Gaussian with $\sigma = 1/3\omega_L$ and applied sequentially for each radial coordinate directly to the harmonic field in the temporal domain with a time-step of 0.03 fs. By applying a Gabor analysis to the harmonic field, one obtains a time–frequency representation that reveals the spectral content of the harmonic emission as a function of the electron recombination time. The Gabor field is therefore defined as

$$E_G(\Omega, t) = \int dt' E_h(t') \frac{\exp\left[-(t' - t_0)^2 \,/\, 2\sigma\right]}{\sigma\sqrt{2\pi}} \exp(-i\Omega t') \tag{3.1}$$

Alternatively to the Gaussian function, the Hann window can be used as a gating function, providing analogous results. The analysis reported here focuses on the cut-

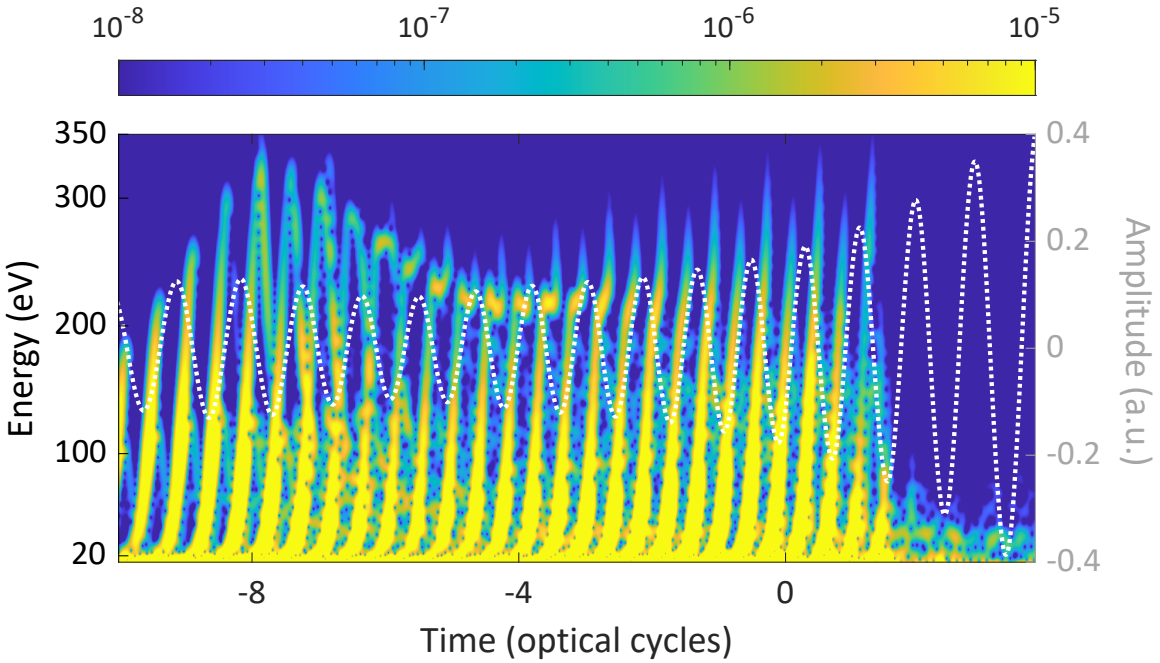

Figure 3.11: *Gabor field (squared modulus) as a function of the photon energy and optical cycle for a radial coordinate of 8* μm *corresponding to the condition of maximum cutoff extension.*

off energies between 200 and 220 eV, which are also observed experimentally. Figure 3.11 shows the Gabor field at the end of the propagation in the gas medium for a radial coordinate of 8 μm as a function of the photon energy and optical cycle of the driving field, where 0 corresponds to the peak of the initial driving field. The generation involves only the first few cycle of the pulse (∼15 cycles FWHM duration), thus highlighting that high photon energies are generated only at the leading edge of the pulse. This can be understood considering the driving field reshaping and defocusing through the plasma: the trailing edge, as shown in Fig. 3.7d is strongly chirped, thus creating unfavourable conditions for efficient phase matching. For this generation case, *short* trajectories are clearly dominant around time zero. In a simple picture, the higher ionization potential of neon (21.6 eV) induces a lower ionization level with respect, for example, to argon (15.7 eV), thus favouring short trajectories that exhibit a weaker dipole phase sensitivity with respect to long trajectories, ultimately being more robust against phase mismatch at high orders. On the other side, for early cycles (-8 to -6), and for energies above 250 eV, short and long trajectories coexist with similar intensity. For later cycles (-6 to -3), the dichotomic simple description of long/short trajectories seems to fail, with non-trivial paths around 200 eV. These structures could be explained in light of the plasma-induced chirping of the driving

field (see Fig. 3.7d), ultimately giving rise to a complex generation dynamics characteristic of the overdriven regime that could be observed also for other cases, *e.g.*, in argon, where, however, long trajectories dominate.

Moreover, a propagation-dependent Gabor analysis of the cutoff region provides further insights into the dynamic build-up of the harmonic field from different temporal and spatial regions across the medium. The results of this analysis are reported in Figure 3.12. The colourmaps show the intensity of the Gabor field integrated between 200 and 220 eV as a function of the radial coordinate and temporal cycle for three different positions in the medium, namely (a) 115 μm, (b) 477 μm, (c) 900 μm (end of medium). The line plots show the integral over the radial and temporal coordinates of the relative maps (black solid lines), together with their corresponding (normalized) integrated driving intensity profile (pink solid line) and the (normalized) intensity profile of an ideal Gaussian beam propagating in free space (pink dashed line). At small propagation distances (z = 115 μm), the high peak intensity of the driving field causes rapid plasma defocusing, limiting the phase matching to the first few cycles, before full ionization of the medium occurs (panel *a*). Additional propagation leads to off-axis (10-15 μm) maximization of the HHG intensity, where the driving beam intensity over multiple cycles is sufficient for the efficient phase matching of the cutoff harmonics without causing excessive ionization of the gas (panel *b*). The driving peak intensity progressively shifts towards later time cycles, while being enhanced at lower radii (< 10 μm), where induces the depletion of the medium *i.e.* its full ionization, and prevents efficient HHG to occur on-axis. Finally, in the second half of the cell (z > 500 μm), the strongly reshaped driving field changes the generation conditions, leading to an overall yield decrease in the central region of the beam (panel *c*) and a spreading to larger radii, allowing for HHG to happen at at shorter radii (double peak). A decrease in the maximum yield, though, indicates unfavourable phase-matching conditions over long propagation distances. The comparison between the intensity profile of the actual driving field and the Gaussian field puts the accent on the influence of the pulse reshaping on the driving field: the shifts of the intensity maximum towards later times (self-steepening) during propagation allow for extending the phase matching window of higher photon energies over multiple cycles, thus leading to an extended cutoff emission.

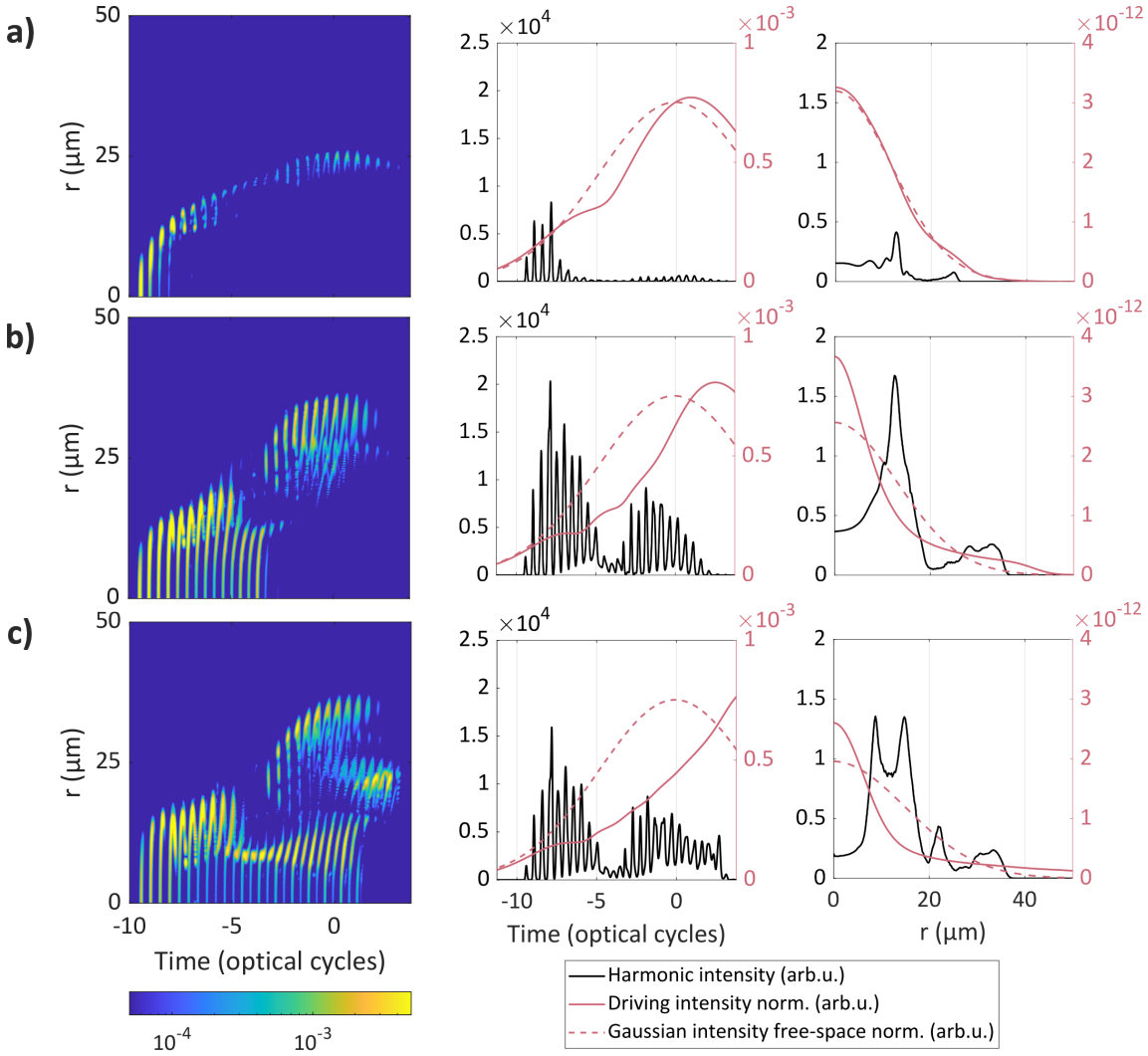

Figure 3.12: *Simulated Gabor harmonic field integrated between 200 and 220 eV as a function of the radial coordinate and temporal cycles. The left, middle, and right panels, respectively, show the intensity of harmonics as a function of radius and optical cycle, obtained through Gabor analysis, along with the corresponding integral over the radial and temporal coordinates (black solid lines) at* ***(a)*** *$z = 115$ μm,* ***(b)*** *$z = 477$ μm, and* ***(c)*** *$z = 900$ μm. The pink traces (right axis in middle and right panels) report the temporal and spatial reshaping of the driving intensity (normalized) due to high plasma density (solid line), and the corresponding (normalized) driving field intensity of a Gaussian beam propagating in free space (dashed line).*

3.4 Conclusions and perspectives

The analysis provided through the simulations guides the identification and optimization of key parameters for HHG in the overdriven regime. Figure 3.9 shows the relevance of the gas confinement: higher photon energies saturate earlier in the medium. Even in the absence of reabsorption, a longer propagation (see Fig. 3.12) can impact negatively on the ultimate harmonic yield as the excessively strong reshaping of the driving field creates unfavourable conditions for the phase matching. The two-stage differential pumping design of the glass cell used in this work nails this challenge: an exceptional gas confinement over a few hundred microns creates the optimal experimental conditions for an unprecedented cutoff extension driven by long pulses. In fact, a good balance between propagation length, therefore, on the amount of reshaping, and temporal duration can favour the cutoff extension also when driving with multicycle pulses. Despite the strong plasma defocusing, thanks to the self-steepening that shifts the field peak to a later cycle, a long and intense driving pulse will still have several sufficiently intense cycles that contribute to the generation process. The simulations additionally highlight the temporal (leading edge) and spatial (off-axis) confinement of the high photon energies of the harmonic field. A careful tuning of the generation geometry - intensity, focusing, and medium position - such that it controls the degree of plasma defocusing and self-steepening of the driving field, could favour the generation at lower radial coordinates. Overall, though, it is worth noticing that the near-field spatial dependence observed from the simulations differs from the far-field experimental measurements and propagation simulations, which show instead a rather homogeneous profile along the vertical spatial coordinate, attributed to the spatial smearing of the field over long distances.

The simplicity of this scheme, especially at 800 nm, which utilizes the direct output of a commercial laser without further temporal compression, eases most of the technical challenges in developing efficient soft X-ray sources for spectroscopic applications. The spectral range so far covered, even though not over the full water-window, already includes several relevant absorption edges of transition metals (Co, Ni, Cu, Zn, Zn, Ga), semiconductor materials (Ge, As, Si), and non-metals (P, S, Cl), and additionally exceeds a photon energy of 92 eV (13.5 nm), which is of particular interest for extreme ultraviolet (XUV) lithography [122, 123]. Moreover, considering the ever-growing use of ytterbium (Yb)-based laser sources at 1030 nm, in similar conditions of generation in the overdriven regime, efficient HHG emission above 300 eV can be expected when operating in Ne or He, and more than 150 eV in argon.

This harmonic source has indeed been designed as a probe arm for a transient ab-

sorption beamline, enabling the study of metallic complexes in solution. The pump arm is meant to be a few-cycle UV pulse generated in fibre through the non-linear process of *Resonant Dispersive Wave (RDW)* emission [124]. Additional details regarding the development of the pump arm are reported in Appendix B. Parallel to this work, the team has developed a thin, flat jet [125, 126] for sample delivery. A purely illustrative schematic of the overall beamline is also reported in Appendix B.

4 | Solid-state High-order Harmonic Generation (sHHG) spectroscopy: investigating the valence electron potential in different TiO_2 solid phases

SHHG has emerged as a powerful, ultrafast spectroscopic technique to probe the electronic structure of crystalline materials with sub-nanometer spatial resolution [38–42]. Unlike gases, where HHG originates from isolated atoms, sHHG encodes information about the periodic potential, band structure, and symmetry of the crystal lattice, making it uniquely sensitive to valence electron dynamics governing the materials' functional properties. In this context, this chapter presents and discusses preliminary results from the PIER Seed Project PIF-2023-08 *Investigation of the valence electronic structure and dynamics of nanostructured materials via high-order harmonic generation*, granted to the author of this thesis (Agata Azzolin). The project has been implemented in collaboration with Sani Harouna-Mayer and Prof. Dorota Koziej, who provided the samples for the experiments.

4.1 Introduction to the project

Over the past two decades, interest in nanophotonics has been steadily increasing, resulting in remarkable advancements in light-harvesting technologies [127], photocatalysis, and optoelectronic applications [128]. By transitioning from bulk systems to corresponding nanomaterials, functional systems undergo significant modifications

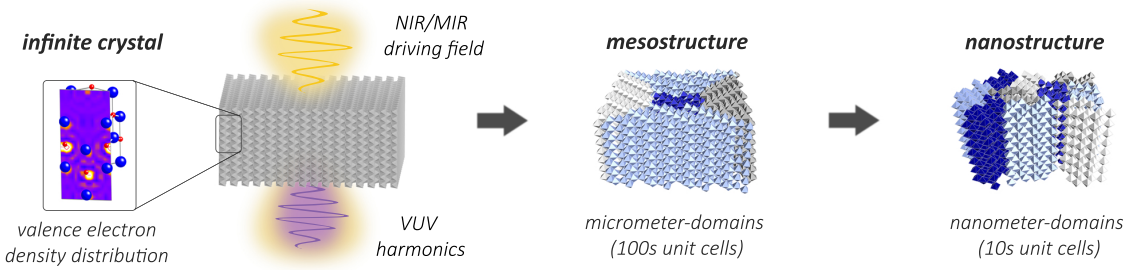

Figure 4.1: *Schematic representation of the three case-studies of TiO_2 from bulk to mesostructure to nanostructure. The HHG emission is expected to encode information on the valence electronic structure and how it is affected by spatial confinement and crystalline domain dimensionality.*

in their electronic structure, leading to enhanced control over their response to external stimuli. However, characterizing these changes remains an open challenge, particularly for valence electronic bands, which play a primary role in the materials' functionality. sHHG has been used to map valence electron distribution of crystalline samples at the picometer scale [129]. Our investigation aims at extending this technique to nanostructured materials. In particular, it focuses on the correlation between dimensionality and valence electronic distribution in the case of a prototypical optoelectronic system, TiO_2 [130], by comparing the non-perturbative HHG response for three structures: (1) bulk crystal; (2) mesostructure, having domains with crystalline orientation over a range of few microns; (3) nanostructured films made of nanorods fully or partially oriented in a preferential direction, where the crystalline orientation is limited to only few tens of unit cells. Figure 4.1 schematically illustrates the experimental idea: a NIR/MIR driving field excites the non-linear harmonic response in TiO_2, first in the bulk crystalline sample, then in the mesostructure, and, finally, in the nanostructured conformation.

4.2 Theoretical background

The microscopic mechanism of sHHG can be described semiclassically via a three-step model analogous to the gas phase (see Ch. 2) but strongly influenced by the band structure [40, 131]:

1. *Tunnelling excitation:*
   the intense driving laser field excites an electron from the valence band to the conduction band near the minimum bandgap via tunnelling ionization. This process generates a coherent electron-hole pair, where the electron's initial momentum is confined near critical points in the Brillouin zone.

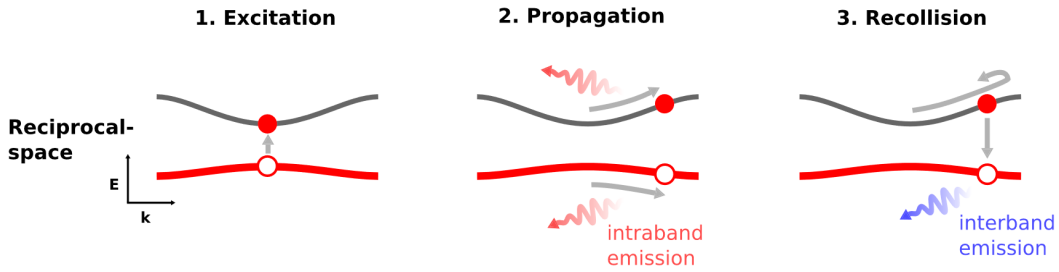

Figure 4.2: *Three-step model in solids HHG in the reciprocal space. Adapted with permission from [131] © Optica Publishing Group.*

2. *Intraband propagation and emission:*
   both the electron and hole accelerate independently in their respective energy bands under the influence of the oscillating laser field. Their dynamics are governed by the band dispersion relations $E(\mathbf{k})$, with the crystal momentum $\mathbf{k}$ evolving according to the semi-classical equation $\hbar\dot{\mathbf{k}} = -e\mathbf{F}(t)$, where $\mathbf{F}(t)$ is the time-dependent electric field.

3. *Recombination and interband emission:*
   at specific times during the laser cycle, *i.e.* when a stationary phase condition is satisfied (coherence of motion), the electron and hole recombine, releasing their accumulated energy as a high-energy photon. The emitted harmonic frequencies correspond to the energy difference between conduction and valence bands along the electron trajectory in reciprocal space.

Figure 4.2 from [131] summarizes the three steps in the reciprocal space.
In the HHG scattering regime described in Ref. [129], electrons behave as quasi-free particles moving inside the Brillouin zone without undergoing Bragg reflections (parabolic bands). This simplifies the harmonic intensity I_N dependence on the Fourier components of the crystal potential $\tilde{V}_{k_l}$ along the laser polarization direction to

$$I_N(\omega_l, F_l, \mathbf{e}_l) \propto \left| N_e \sum_{k_l} \tilde{V}_{k_l}\, k_l\, J_N\left(\frac{k_l F_l}{\omega_l^2}\right)\right|^2 \tag{4.1}$$

where N_e is the number of electrons, J_N is the Bessel function of order N, and F_l, ω_l, and $\mathbf{e}_l$ are the driving field amplitude, frequency, and polarization unit vector, respectively. Physically, this expression represents a one-dimensional projection of the crystal potential sampled by the electrons oscillating under the laser field. By systematically varying the laser polarization and field strength, the Fourier components $\tilde{V}_{k_l}$ can be experimentally retrieved, enabling a two-dimensional tomographic reconstruction of the valence electron potential with picometer-scale resolution.

Furthermore, the maximum reachable harmonic order (cutoff energy E_c) relates directly to the highest reciprocal lattice vector $k_{\max}$, setting the ultimate spatial resolution of this technique and linking to the valence electron radius r_v as:

$$r_v \approx \frac{2\pi F_l}{E_c\,\omega_l} \tag{4.2}$$

Direct access to this quantity provides not only further insights into the material's valence electronic properties and its functionality, but also real-space information to relate to spatial confinement and crystalline domains dimensions.
Another important parameter to link spatial confinement and HHG emission in nanostructured material is the *maximum electronic excursion*, x_{max}, defined as the maximum spatial displacement of the laser-driven electron in the crystal lattice. For a classically described electron, the excursion length is approximately proportional to the driving field strength and the square of the laser wavelength:

$$x_{max} \propto F_l \lambda_l^2 \ , \tag{4.3}$$

where F_l and λ_l are respectively the field amplitude and the laser central wavelength. The value of x_{max} sets the spatial scale over which the electron explores the crystal potential during sHHG. When x_{max} remains smaller than the characteristic correlation length of the crystal domains, *i.e.* the spatial extent of ordered regions, electrons experience a locally periodic potential, justifying the assumption of an infinite, perfect lattice used in most sHHG theoretical models. In this regime, harmonic emission accurately encodes the crystal's valence electronic structure. However, in nanostructured materials with reduced domain sizes or increased disorder, if x_{max} exceeds the domain correlation length, electrons are more likely to encounter structural boundaries, defects, or amorphous regions. This leads to enhanced electron scattering and decoherence, modifying the harmonic spectrum in both intensity and spectral shape, eventually invalidating the infinite crystal approximation. Recent studies on SiO_2 [132] demonstrated that crystalline and amorphous phases exhibit similar HHG responses when x_{max} is less than the correlation length, but deviate significantly beyond this scale. This behaviour provides a diagnostic tool to quantify the minimal crystal domain size and degree of order required for sHHG spectroscopy to remain valid.
In the following, preliminary experimental results are presented that apply these concepts to bulk, semi-ordered, and amorphous TiO_2 samples.

4.3 Experimental setup

The measurements have been performed using the custom-developed 7013-XPIC OPCPA system from *Class5*. The laser system provides 250-μJ energy, 30-fs FWHM-duration pulses centred at 2 μm up to 100 kHz repetition rate. The output spectrum is reported in Figure 4.3. It has two main peaks at 1950 and 2050 nm and a prominent shoulder at 2150 nm. The source has residual components in the visible (VIS) that are filtered using a long-pass filter. The driving laser is focused into the sample using a CaF_2 lens with a 40 cm focal length, resulting in a driving beam spot size of 200 μm in diameter. A tunable intensity attenuator consisting of a half-wave plate (super-achromatic quartz and MgF_2 retarder, B-Halle GmbH) and a wiregrid polariser (WP25M-UB Thorlabs), followed by an additional half-wave plate to tune the driving field polarization, is placed before the focusing optic. Considering the losses introduced by the optics, the maximum pulse energy at the sample position is 180 μJ. The samples are placed on an XY translational optical mount to tune their vertical and horizontal position and hit a fresh, non-damaged spot at every new acquisition. The position of the samples along the laser propagation direction is controlled through a manual translation stage. A motorized stage, on the other hand, is used to control the direction of the transverse axis with respect to the laser propagation. To limit thermal-induced damage in the transmission optics and on the samples, the repetition rate is limited to 5 kHz. The emitted radiation is refocused and collected using a commercial VIS-UV spectrometer (OceanFX, Ocean Optics), which covers the wavelength range from 1000 nm to 200 nm. The residual driving field radiation after generation is partially filtered with a pinhole before entering the spectrometer, exploiting its larger divergence compared to the emitted harmonics. A vacuum-ultraviolet (VUV) spectrometer (VS150, Resonance) can be optionally installed in place of the VIS-UV one to detect signals down to 110 nm. To this purpose, the samples and refocusing optics are placed in a vacuum chamber (1-mm thick CaF_2 window at entrance) that can reach pressures in the order of $10^{-5} - 10^{-4}$ mbar.

4.3.1 TiO_2 samples

TiO_2 exists in different polymorphic forms, the most common of which are rutile, anatase, and brookite (Figure 4.4 from [133]). Its natural crystalline form is typically rutile, as the other polymorphs are unstable over extended ranges. Anatase and brookite are generally grown only as thin films or nanoparticles. Anatase and rutile crystalline forms have a tetragonal structure, corresponding, respectively, to the space groups $I4_1/amd$ and $P4_2/mnm$. Meanwhile, brookite is orthorhombic with the

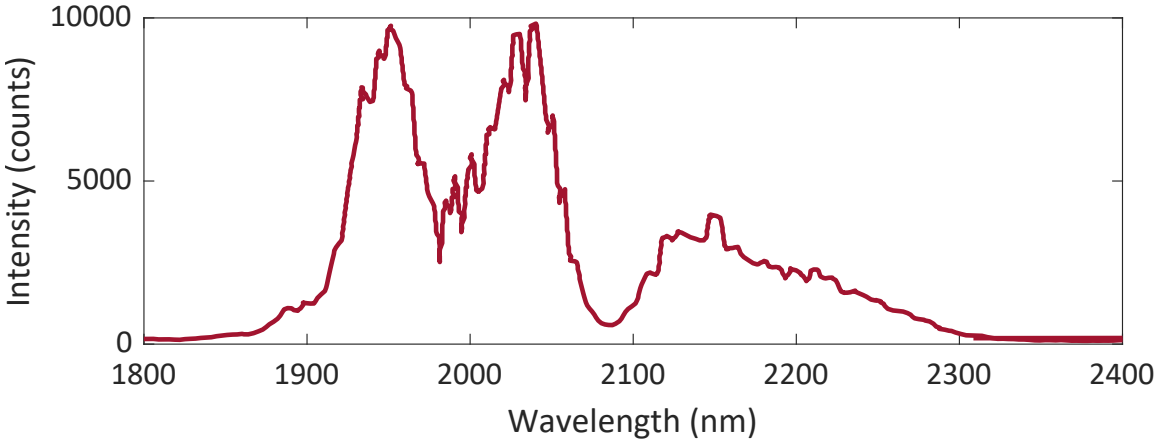

Figure 4.3: *Output spectrum of the 7013-XPIC OPCPA laser system (Class 5).*

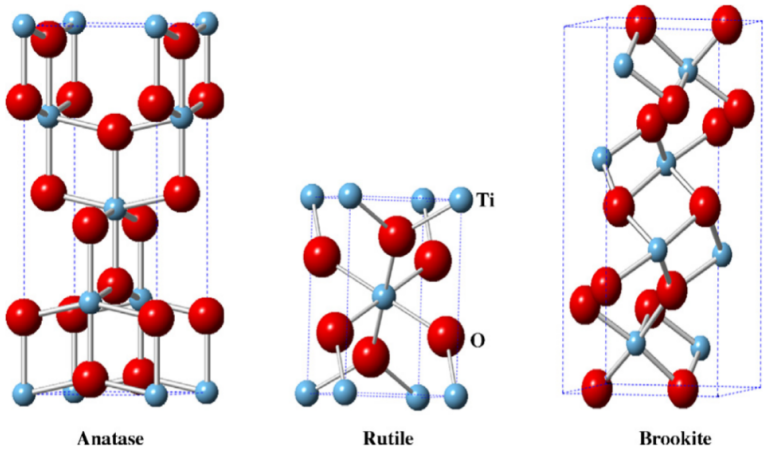

Figure 4.4: *Crystalline structures of anatase (tetragonal), rutile (tetragonal), and brookite (orthorombic) TiO_2 polymorphs. Reproduced from [133] with permission from Elsevier.*

space group Pcab. The bandgap is in the range of 3.2-3.3 eV for all polymorphs. This means that the material starts absorbing UV light around 300 nm, and it is transparent at longer wavelengths. The different crystalline symmetries can be mapped by sHHG, *i.e.* for the same generation parameters, they are expected to produce spectra differing in intensity and shape.

The experimental measurements have been performed on a set of TiO_2 structures summarized in the following:

1. *Rutile (110)*:
   Flat bulk crystal substrate of 500 µm thickness in the rutile form cut along the plane (110), polished on both side with an average surface roughness (Ra) lower than 0.5 nm, commercially provided by Crystal GmbH.

2. *Amorphous thin films*:
   The films are synthesized through Atomic Layer Deposition (ALD), a tech-

nique that allows fine tuning of the thickness, and are deposited on sapphire substrates of thickness either of 100 μm or 500 μm (both side polished, Ra<0.5 nm from Crystal GmbH). Sapphire is chosen for its large bandgap (9 eV), giving it transparency down to the UV, and high damage threshold, as it can withstand high intensities without contributing to the harmonic generation nor introducing non-linearities. The samples are characterized by the collaborators through X-ray diffraction (XRD) measurements and their anisotropy studied by three-dimensional pair distribution function [134]. The films produced have thicknesses of 101, 48, and 17 nm.

3. *Meso-crystalline films*:
   Meso-crystalline films are obtained through TiO_2 nanorod-alignment (100 x 20 nm) by Langmuir-Blodgett (LB) technique, a flexible method that allows control of the ordering of the nanorods, and of the film thickness [135], followed by high-temperature crystallization at 1000°C. As for the amorphous samples, the films are deposited on sapphire substrates (specifications above) and are characterized using XRD. hey have a brookite crystalline orientation along the (100) plane, confined to domains of only a few hundred nanometres. The films result from the stacking of 2, 6, or 10 layers of nanorods, corresponding to a thickness in the order of hundreds of nanometres. In principle, the LB technique would allow the realization of fully-aligned nanorod systems; however, the use of sapphire substrates, rather than fused silica ones, causes superficial tensions that prevent their complete alignment. So far, only partially aligned systems have been synthesized.

4.3.2 Geometry of generation

The measurements have been performed both in transmission and reflection geometry. The transmission geometry generally allows for higher intensities at the generation point (normal incidence); however, in this configuration, the emitted radiation can be strongly affected by reabsorption in the sample and phase mismatch (walk-off of the harmonic components). To mitigate this effect, the samples are illuminated from the back, *i.e.* the substrate side. In this case, only sapphire substrates of 100-μm thickness have been employed to limit possible non-linear effects on the driving field. In the transmission measurements, the thickness of the sample significantly affects the harmonic emission; therefore only thin samples can be considered.
In comparison, a reflection geometry at grazing incidence can offer several advantages without being limited by the sample's thickness. First, it suppresses bulk phase

mismatching effects [38, 136–138] and reabsorption as the generation is confined near the surface [139]. Even though the driving field can penetrate deeply into the material, given the TiO_2 transparency to the NIR, harmonics generated far from the surface cannot escape the material, being reabsorbed by the material or undergoing phase mismatch along propagation. The effective length contributing to the generation can be defined as the minimum between absorption-limited escape length and coherence length. A harmonic generated at depth δ and at an internal angle θ_h with respect to the surface normal must propagate in the material through a path length of

$$L_{propag} = \frac{\delta}{\cos(\theta_h)} \ . \tag{4.4}$$

Note that for transmission (normal incidence), $\theta_h = 0$: for the same depth δ, harmonics propagate through a shorter distance to escape the material. This means that transmission geometry has the potential of generating harmonics at higher depths. The emission intensity I_0 is attenuated by absorption following Lambert-Beer's law

$$I_0 \exp(-\alpha_h \, L_{propag}) \ , \tag{4.5}$$

where α_h is the absorption coefficient for the harmonic frequency. From these considerations, the maximum effective length before the harmonic radiation is fully reabsorbed is

$$L'_{abs} = \frac{\cos(\theta_h)}{\alpha_h} \ . \tag{4.6}$$

Analogously to the generation in gases (see Ch. 2), the coherence length is defined as

$$L_{coh} = \frac{1}{|\Delta k_z|} \ , \tag{4.7}$$

where Δk_z is the phase mismatch along the surface normal: $\Delta k_z = n_h k_{L,z} - k_{h,z}$, with n_h the harmonic order, and k_L, k_h the wavevectors of the driving and harmonic fields respectively. Thus, the effective depth contributing to generation can be approximated as

$$L_{eff} \approx \min\{L'_{abs}, L_{coh}\} \ . \tag{4.8}$$

Considering a driving field in the NIR and a harmonic field in the UV, this effective length is typically on the order of a few tens of nanometres in absorbing dielectric materials. It decreases as the harmonic frequency increases, *i.e.* with increasing difference in refractive indices between driving and harmonic fields. Since the sHHG emission in the reflection configuration is confined to a few nanometres, it also means that it is more strongly affected by surface impurities that act as sources of decoher-

ence.

Moreover, in reflection geometry, the excitation of different material components can be selectively accessed by controlling the polarization state of the driving field. Since the non-linear optical response in anisotropic or birefringent materials depends strongly on the polarization direction relative to the crystallographic axes, varying the driver polarization enables the selective excitation of ordinary or extraordinary waves, or different non-linear tensor components [140]. This control is particularly effective in reflection, where the incident and generated fields interact near the surface and different polarization components can be preferentially enhanced or suppressed, allowing tailored access to distinct excitation pathways within the material. For example, working close to the Brewster angle with p-polarized light maximizes the transmission of the driver in the material while limiting its reflection, thus acting as a natural spectral filtering of the (weak) harmonics with respect to the fundamental beam [137]. The Brewster angle in TiO_2 is 67.6° for the ordinary axis and 69.5° for the extraordinary one. In transmission geometry, the excitation of different material components through driver polarization control is generally less effective because the driving field propagates deeply through the bulk of the material, averaging over all polarization-dependent non-linearities along the path. This causes the contributions from different tensor components or polarization directions to mix and interfere, thereby reducing the method's selectivity. Finally, a grazing incidence angle allows for illuminating the sample over a larger area leading in turn to a lower peak intensity with respect to normal incidence, scaled by $\cos(\theta)$, which minimizes damages. Based on the considerations above, an incidence angle of 75° has been employed for the measurements reported in the next section.

As reported in recent reviews [39, 42], transmission geometries have been generally preferred due to the lower technical complexity, while still giving access to structural information, of interest especially for two-dimensional materials. The reflection geometry (backward emission) has been discussed in comparison to the transmission geometry (forward emission) in Ref. [137], which highlights the optimal phase matching of the former with respect to the latter. Reflection setups have been mainly used to generate harmonics from plasma at surfaces, with early measurements reported in Refs. [141–144] and a more recent overview of the methods in Refs. [145, 146]. However, only few experiments [136, 138, 147] exploited a reflection configuration for sHHG spectroscopy, as the additional degrees of freedom it offers often add complexity to the interpretation of the results.

4.4 Experimental results

The transmission geometry has been employed to study the response of the ALD-synthetized amorphous TiO_2 films while varying their thickness. Due to the strong reabsorption, sHHG from the bulk sample cannot be achieved. The generation from the meso-samples has been attempted too, however observing only up to the 5^{th} harmonic (HH) thus not offering deeper insights with respect to what is reported in the following for the reflection geometry. The results from the generation in the ALD-synthetized samples are shown in Figure 4.5. The spectra have been generated at a driving peak intensity of 12.4 TW/cm^2 and s-polarization (vertical) of the driving field. The 5^{th} HH is strongly visible for all three cases, while the 7^{th} HH increases in intensity by lowering the thickness due to reabsorption effects. The 9^{th} HH could be detected only from the thinnest sample. Since the harmonics generated deeper in the sample are more likely to be affected by both decoherence and reabsorption, large thickness results in a detrimental effect on the harmonic yield compared to thinner samples. This observation is in agreement with the data reported in Ref. [148] for below-bandgap harmonics in epitaxially grown ZnO films. A numerical investigation proposed in Ref. [149] for silicon films suggests that the optimal thicknesses for HHG is between 2 and 15 nm. Moreover, for amorphous samples, the bandgap tends to decrease the with the thickness [150] as a consequence of quantum confinement and structural changes in the limit of nanometre-thicknesses. A larger bandgap translates into a larger transparency window, directly affecting the transmission of the 7^{th} (285 nm) and 9^{th} (222 nm) HHs, which are generated close to the bandgap. In Ref. [151] the authors have demonstrated that the efficiency of the harmonics is limited by phase mismatching below the bandgap, and by absorption for those above the bandgap. Considering that the harmonics observed in Fig. 4.5 are close to the bandgap, most probably the emission is ruled by the interplay of both mechanisms.
By varying the intensity of the driving field, the scaling law of the harmonic intensities can be determined. If the intensity of the n-th harmonic I_h scales proportionally to I_L^n, with I_L the driving intensity, the generation occurs within the perturbative regime; otherwise, it corresponds to the non-perturbative regime. This behaviour provides insight into the underlying generation mechanisms and guides the appropriate modelling [38, 131], *e.g.* in the perturbative regime the harmonics are generated by a cascade of non-linear processes, such as multiphoton absorption and wave mixing, while in the non-perturbative regime the generation is dominated by intra- and inter-band electron dynamics, such as Bloch oscillations. The harmonic intensity scaling laws for the three amorphous samples in the transmission configuration are

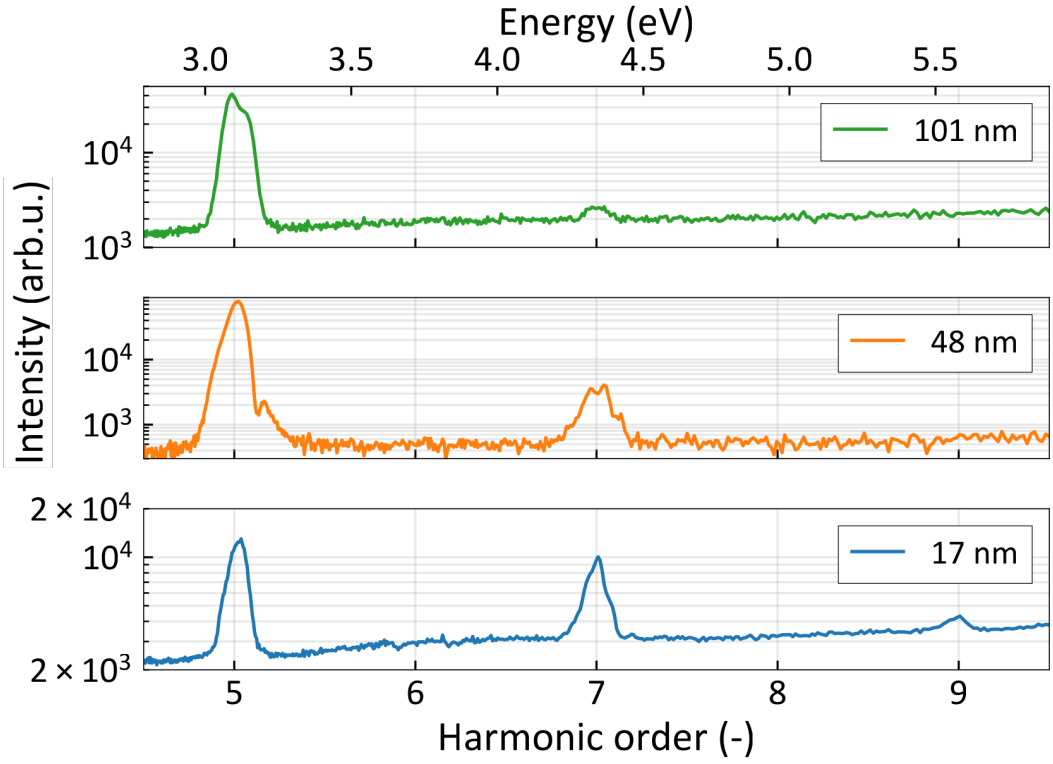

Figure 4.5: *sHHG spectra in transmission geometry from amorphous TiO_2 samples of thickness 101 nm (top, green), 48 nm (middle, orange), 17 nm (bottom, blue), synthesized through ALD. The driving field is s-polarized and has a peak intensity of 12.4 TW/cm^2.*

reported in Figure 4.6a-c. Only the 5^{th} HH of the 17-nm-thick sample is generated in the perturbative regime. All other HHs strongly deviate from the perturbative scaling, even though they do not show a clear correlation between them. The harmonic intensities saturate between 10-12 TW/cm^2 in the thickest samples, and at 14 TW/cm^2 for the thinner, consistently with previous results of sHHG from oxides materials [40]. At higher driving intensities, deviations from saturation are most likely related to sample damage.

In this measurement campaign, the reflection geometry has allowed to map the sHHG response from the whole set of samples under investigation (Figure 4.7), including: bulk crystal rutile (110) (top, red), amorphous samples of thickness 101 (green) nm and 48 nm (orange) synthesized by ALD (middle), and meso-crystal consisting of a 6-layer deposition through LB technique (purple, bottom). Due to the geometry, the maximum driving peak intensity achievable has been 6 TW/cm^2. The spectra here reported have been collected at a driving peak intensity of 4.8 TW/cm^2 for the rutile and the meso-crystal sample, and of 6 TW/cm^2 for the two ALD-synthesized samples. In order to avoid saturation also the 5^{th} HH of the 48-nm sample is reported for a driving intensity of 4.8 TW/cm^2. The difference of driver between 5^{th}

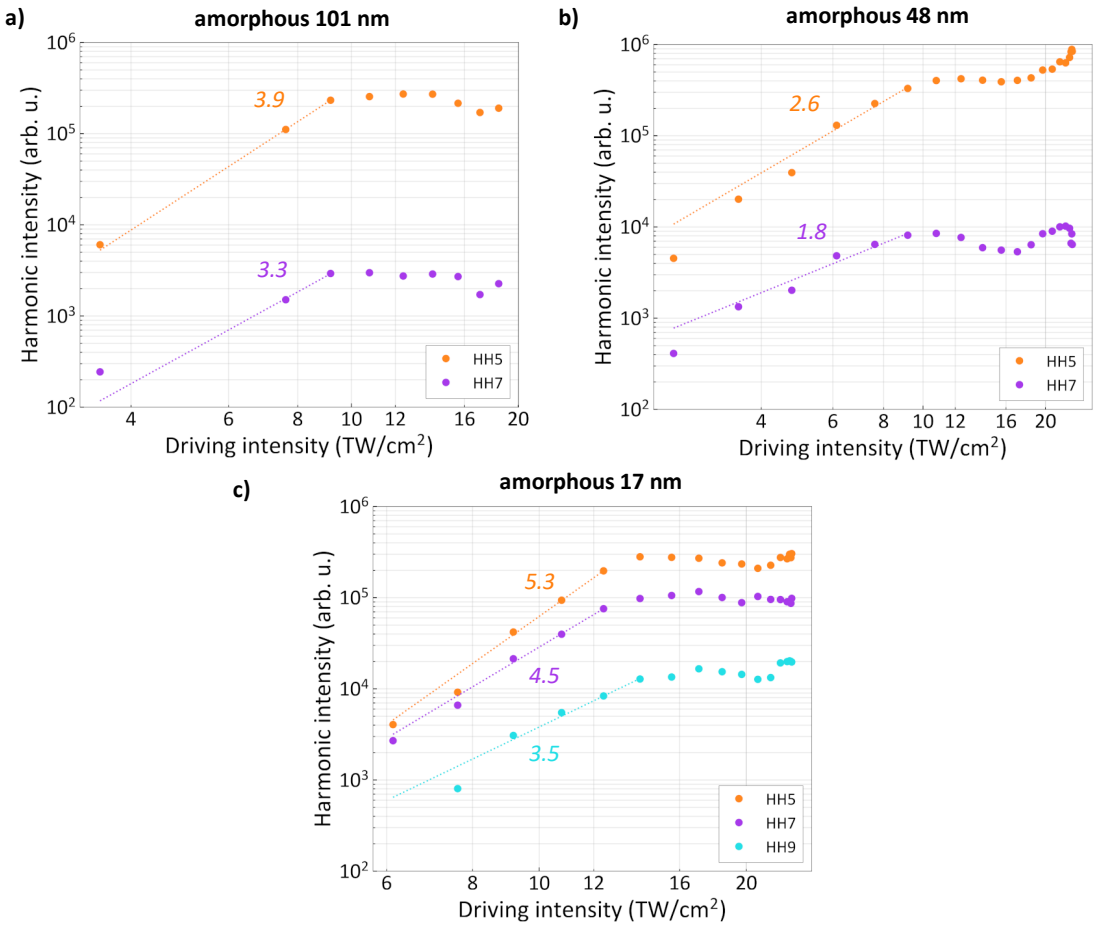

Figure 4.6: *Harmonic intensity scaling with respect to the driving intensity for the amorphous samples of thickness* ***(a)*** *101 nm,* ***(b)*** *48 nm, and* ***(c)*** *17 nm. The colour-coded numbers reported in the plots correspond to the scaling powers of each harmonic as retrieved from the fitting (dashed lines).*

and 7^{th} HH is highlighted in the plot as a dotted discontinuity. The driving field is p-polarized (horizontal) for the spectra of rutile crystal and amorphous films, and is s-polarized for the meso-crystalline sample. The 5^{th} HH is clearly visible for all the three cases. The 7^{th} HH has been observed in the rutile and amorphous samples, but not in the meso-crystalline one. In the former, it has comparable intensity to the 5^{th} HH, but in the amorphous samples it is almost an order of magnitude less intense. The 9^{th} HH could be observed only from the rutile sample. The absence of higher harmonics in the amorphous samples together with their very weak emission of the 7^{th} HH suggest that the maximum driving intensity achievable in this configuration has not been enough to excite emission of higher orders. However, since the emission is confined to a few nanometers, the harmonic spectrum could be strongly affected by phase matching and surface impurities. In the explored driving conditions (intensity and polarization, see below), the meso-crystalline sample emitted the 5^{th} HH only.

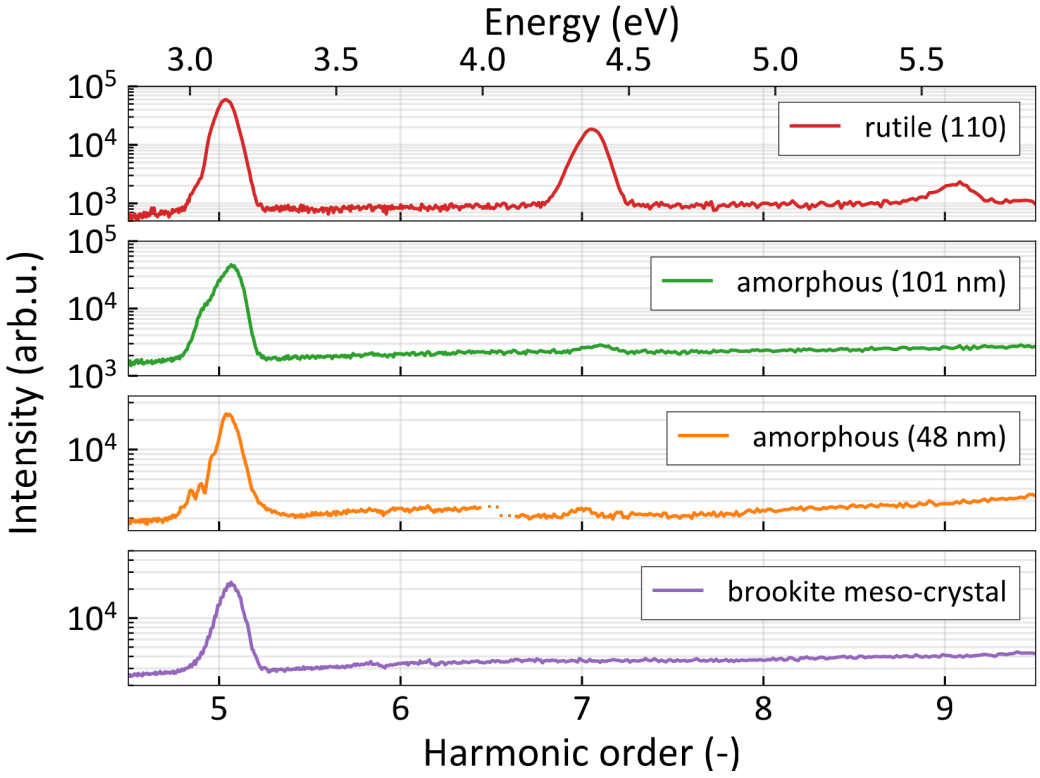

Figure 4.7: *sHHG spectra in reflection geometry (75° angle of incidence) from TiO_2 samples: bulk rutile (110) crystal (top, red), amorphous films of thickness 101 nm (middle, green), 48 nm (middle, orange), and brookite meso-crystalline sample consisting of a 6-layer deposition through LB technique (purple, bottom). The driving peak intensity is between 4.8 and 6 TW/cm^2 and the driving field is p-polarized except for the bottom spectrum where is s-polarized (see main text for details). For the 48-nm-thick sample, the 5^{th} HH is shown for a driving intensity of 4.8 TW/cm^2 to avoid saturation, while the 7^{th} HH for 6 TW/cm^2, to enhance the response. The difference is represented in the plot as a dotted discontinuity.*

The intensity scaling law for the four samples of Figure 4.7 is reported in Figure 4.8a-d. For the 48-nm-thick amorphous sample, the intensity dependence of the 7^{th} HH has been omitted as the threshold intensity to observe it is close to the maximum achievable one, thus the fitting wouldn't have been reliable, consisting of only a few points over a very small range. For all the cases, the 5^{th} HH seem to result from the perturbative regime, with scaling powers ranging from 4.9 to 5.9. The 7^{th} and 9^{th} HHs for rutile and the 101-nm-thick amorphous samples scale non-perturbatively with scaling powers between 4 and 5.

Moreover, in reflection geometry the anisotropic response of the TiO_2 samples with respect to the polarization of the driving field was characterized. After calibration, different linear polarizations of the driving field have been selected by moving the second half-wave plate at fixed input intensity (see setup description in Sect. 4.3). An angle of 0° in the plots corresponds to an s-polarized driving field, and 90° to a p-polarized field. A polarization-dependent measurement for the rutile (110) crys-

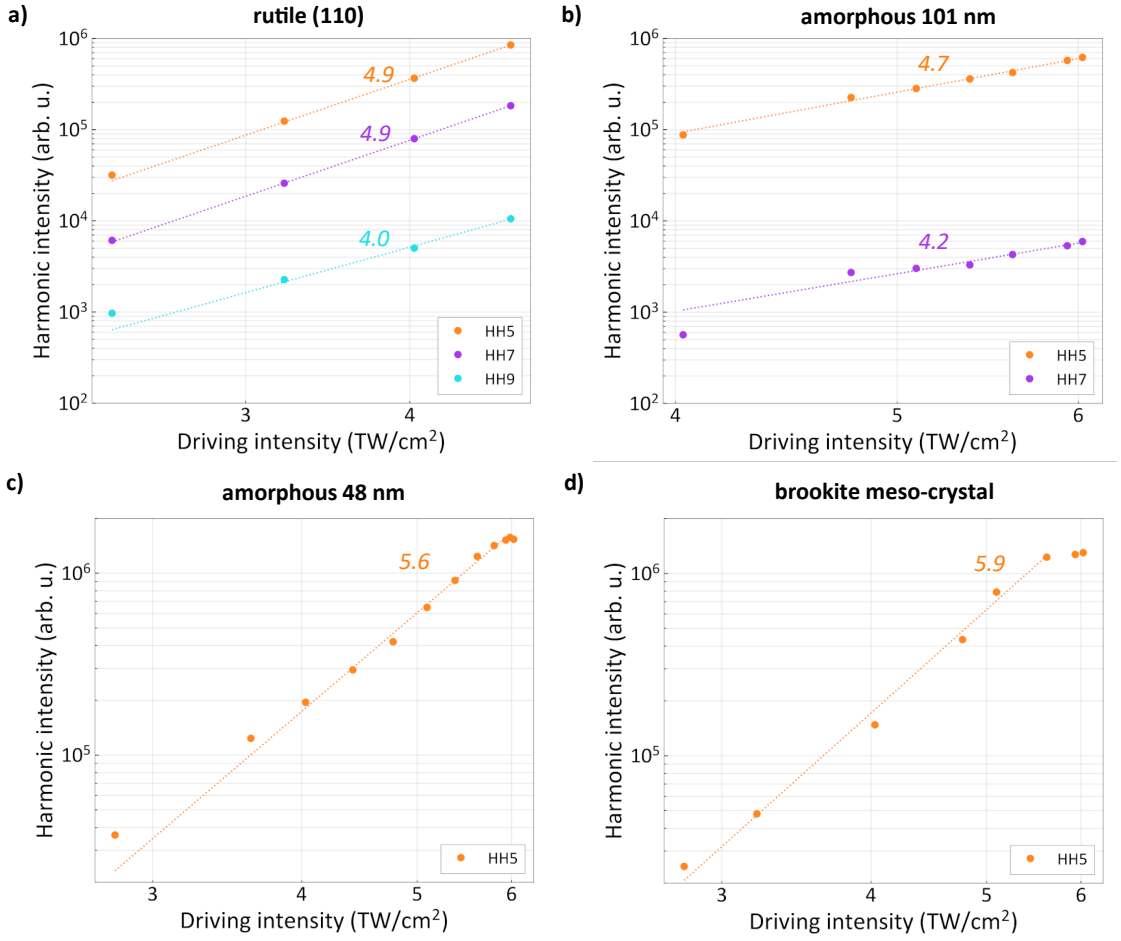

Figure 4.8: *Harmonic intensity scaling with respect to the driving intensity for the samples of Fig. 4.7.* ***(a)*** *bulk rutile (110) crystal,* ***(b)*** *101-nm-thick amorphous film,* ***(c)*** *48-nm-thick amorphous film, and* ***(d)*** *meso-crystalline system (brookite film). The colour-coded numbers reported in the plots correspond to the scaling powers of each harmonic as retrieved from the fitting (dashed lines).*

talline sample is reported in Figure 4.9 as a polar map having the spectral photon energy (harmonic order) as radial coordinate, providing a concise overview of the anisotropic emission of each harmonic. To visualize the behaviour of different harmonics, the map has been translated into polar plots. Single harmonic emissions are reported in Figure 4.10a-d for each of the four samples of Fig. 4.7. The intensities used in these measurements have been kept below the damage threshold, ensuring that the response does not change over the acquisition time (approximately 20 minutes, with integration times between 500 and 700 ms for each spectrum). This corresponds to a driving intensity of 5 TW/cm^2. For the rutile (110) sample, top row in Fig. 4.10, the harmonic response is strongly (5^{th} and 9^{th} HHs) or fully (7^{th} HH) suppressed when the driving field is vertically polarized (0° in the plots). This reflects the anisotropy of the crystal, and it is also consistent with the fact that the angle of incidence is close to the TiO_2 Brewster angle, thereby enhancing p-polarized radia-

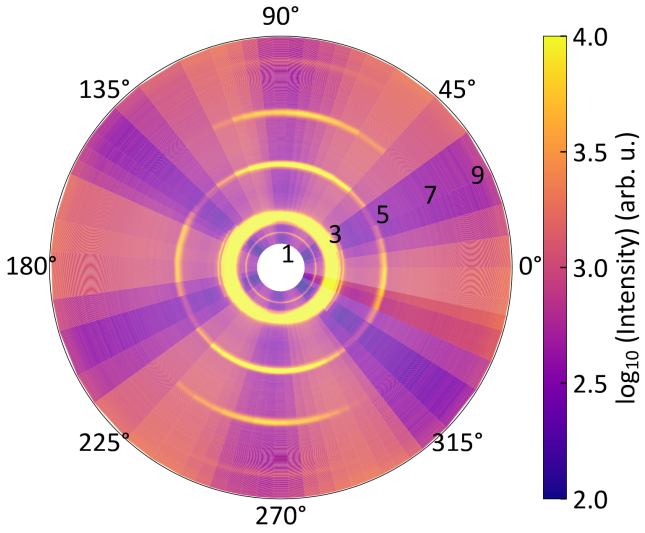

Figure 4.9: *sHHG as a function of the linear polarization of the driving field. An angle of 0° corresponds to s-polarized (vertical) driving field, 90° to p-polarized (horizontal). The radial coordinate corresponds to the HH order.*

tion inside the material and suppressing s-polarized radiation. Multiple polarization scans at different driving intensities, as reported in Ref. [152], could shed light on the interplay between microscopic mechanisms and threshold intensities for different polarizations and are planned for the near future. For the amorphous samples (middle rows), the relative emission efficiency for 0° polarization is comparable to 90°. In particular, they are equivalent in the 48-nm-thick sample, indicating an increasing loss of anisotropy, in agreement with the amorphous nature of the sample. The 7^{th} HH of the 101-nm amorphous sample shows a non-trivial emission along the 45° polarization axis. However, the signal-to-noise ratio for this harmonic is particularly low to claim this with certainty. Instead, the 7^{th} of the 48-nm thick amorphous sample has the same symmetry as its 5^{th} emission. The brookite meso-crystalline sample (bottom row), despite the limited crystalline ordering, shows a residual anisotropy with stronger harmonic emission for s-polarized driving light. Its response differs from both rutile and amorphous samples, with a double peak dependency around the horizontal polarization (90° in the plots). The different responses are potentially related to the different TiO_2 phases, similarly to the case of liquid crystals in Ref. [153]. However, to transcend the qualitative comparison reported here, numerical simulations are necessary, and external theoretical support is currently under development.

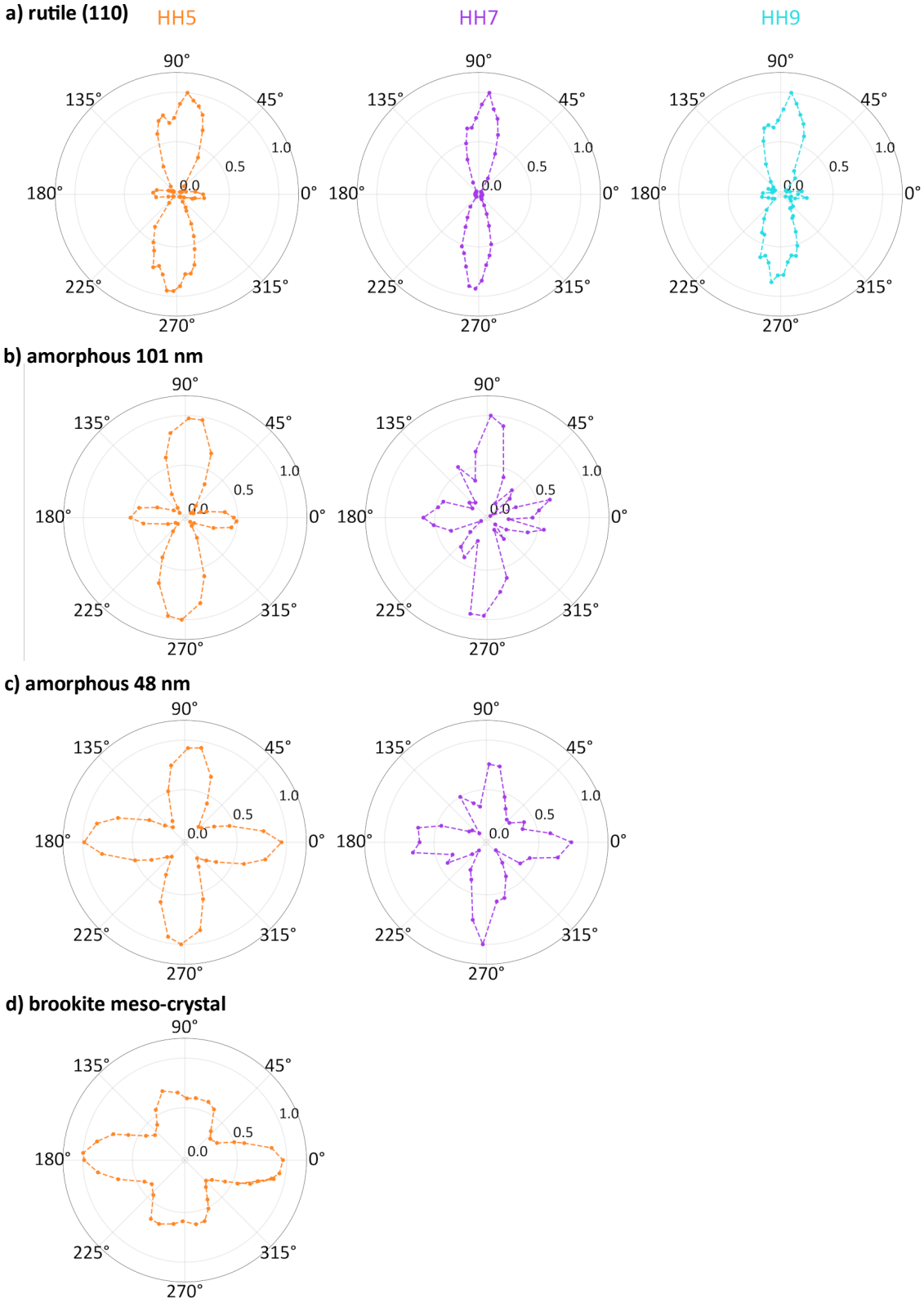

Figure 4.10: *Normalized polar-plot of the anisotropic sHHG emission as a function of the driving field polarization for* ***(a)*** *bulk rutile (110) crystal, amorphous films of thickness* ***(b)*** *101 nm,* ***(c)*** *48 nm synthesized through ALD, and* ***(d)*** *brookite meso-crystalline sample consisting of a 6-layer deposition through LB technique (purple, bottom). An angle of 0° corresponds to s-polarized (vertical) driving field, 90° to p-polarized (horizontal). The radial coordinate corresponds to the normalized HH intensity.*

4.5 Conclusions and perspectives

This chapter reported preliminary results of sHHG in different solid state phases of TiO_2, from bulk crystals to meso-crystals, and amorphous films. Although further analysis and numerical simulations are ongoing, the qualitative comparison of the results reveals significant differences in the response of the samples. These results set a clear course of action to achieve the originally planned objectives of a tomographic mapping of the valence electron potential. The method proposed in [129] is based on the fitting of the harmonic intensity with respect to the driving field strength. In order to ensure the robustness of the procedure, (1) more than two or three harmonics need to be measured, (2) over a finer grid of intensity points. Considering the strong reabsorption of TiO_2 in the UV and VUV, it could be useful to use a longer driving wavelength in the MIR to shift the spectral emission in the VIS region. A finer and reproducible tuning of the intensity should be ensured my a motorized rotor stage controlling the angle of the first half wave-plate (see setup description in Sect. 4.3). Moreover, this fitting procedure needs to be repeated for different crystalline orientations with respect to the polarization of the laser field. To this purpose, even though the reflection geometry offers the advantage of a harmonic emission free from propagation effects [136, 137], it complicates the understanding of which crystalline axis is responsible of which emission as the direction of the field in the material is subjected to refraction according to the Snell's law and to reflection and transmission as per Fresnel equations. Therefore, to simplify the interpretation of the results, a transmission geometry should be preferred with the implication, supported by these results, of working with thinner samples, both amorphous and crystalline, the latter synthesized for different orientations. In these conditions, the signal is expected to be several orders of magnitude lower than the driving field and therefore the setup and detection system should be able to provide high sensitivity, *i.e.* high signal to noise ratio. To achieve this goal, on one hand, it is primary to improve the rejection of the driving field after generation using dedicated spectral filters; on the other hand, increasing the data statistic by operating at higher repetition rates would be advisable. Further experiments that would provide deeper insights into the microscopic mechanisms linking sHHG to the sample structure and spatial confinement include the investigation of the harmonic anisotropic response as the driving field intensity changes, and the analysis of the polarization of the emitted harmonics. Finally, further characterizations of the samples under investigation could help complete the picture. For example, spectroscopic ellipsometry measurements would determine the sample's bandgap and complex refractive index, and Scanning

Electron Microscopy (SEM) would characterize the surface structure of the films. The latter has not been performed yet as it is a destructive technique that requires the deposition of a conductive layer on the dielectric material to be imaged.
The proposed workflow has the potential to provide a full correlation map between harmonic response, sample structure and spatial confinement, an aspect not yet fully explored in literature, except for few examples involving the generation from quantum dots [154–156], plasmonic nanostructures [157, 158], or liquid crystals [153]. The same methodology could be extended to other materials to establish a convenient all-optical technique for investigating the valence electron distribution as a function of spatial confinement, a topic at the heart of nanoscience.

PART III

Double-Blind Holography at Free-Electron Lasers

5 | Fundamentals of Double-Blind Holography (DBH)

This chapter introduces the fundamentals of DBH, an all-optical method used for pulse characterization and imaging reconstruction. The method and algorithm are illustrated here to support the experimental results presented in the following Chapter 6. The theoretical foundation for this work was provided by collaborators at the Weizmann Institute of Science in Rehovot, Israel, specifically Prof. Nirit Dudovich, Prof. Dan Oron, and Prof. Oren Raz, along with their respective teams.
DBH is a specific implementation of *holography*. In holography, an unknown field (or object) is reconstructed from the interference with a known reference field. A typical scheme (Figure 5.1) consists of an interferometer in which one arm interacts with an unknown object whilst the other arm propagates unperturbed. Their interference is collected onto a photographic plate, which, upon illumination with the reference field, reproduces the original object as the recorded interferogram acts as a diffraction grating. In DBH, both fields are unknown. In order to reconstruct the fields, two requirements need to be satisfied: (1) the fields are fully independent, *i.e.* they cannot have common polynomial roots, (2) the fields fulfil the temporal Compact Support (CS) condition, for which they are non-zero inside a temporal window of a given length, and exactly zero outside it. In the following, the reconstruction algorithm as presented in Refs.[159, 160] is introduced.

5.1 Vectorial Phase Retrieval (VPR) algorithm

The algorithm used in DBH for the full retrieval of unknown fields is called *Vectorial Phase Retrieval (VPR)*. This method is documented and mathematically demonstrated in terms of robustness and uniqueness of solution in its one-dimensional form in [159, 160, 162], and subsequently extended in two dimensions in [63, 163]. This

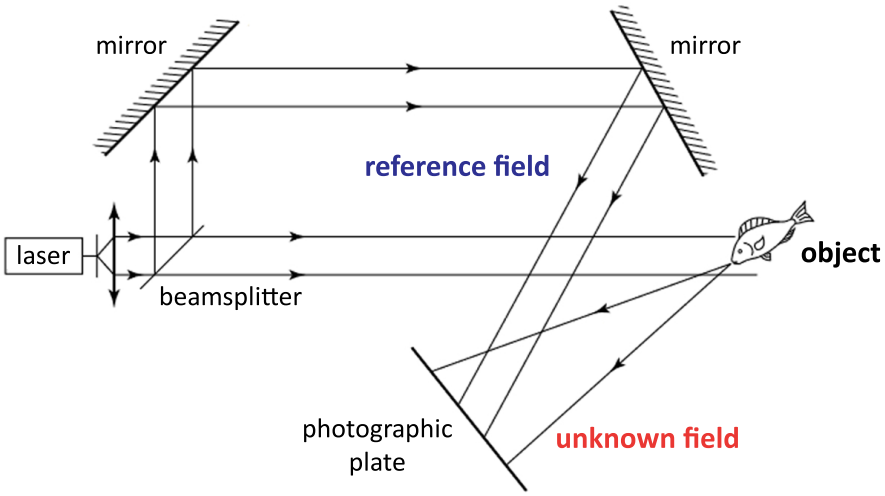

Figure 5.1: *Holographic system,The interference of a known reference field with an unknown field interacting with an object is recorded at the photographic plate. Upon illumination of the plate, the original unknown object (i.e., its field) can be reconstructed. Illustration reproduced and adapted from [161] with permission from Cambridge University Press through PLSclear.*

section presents and summarizes the main concepts behind the algorithm without aiming at its full mathematical demonstration, for which the reader is referred to the original works.

Let $f_i(t_k)$, with $i = 1, 2$, be two unknown discrete temporal signal defined as:

$$f_i(t_k) = \frac{\Delta\omega}{2\pi} \sum_{j=0}^{N-1} |F_i(\omega_j)| e^{\mathbf{i}\phi_i(\omega_j)+\mathbf{i}\omega_j t_k} \tag{5.1}$$

where $|F_i(\omega_j)|$ denotes the spectral amplitude sampled over $n = 1, ..., N$ equispaced frequencies $\omega_j = j\ \Delta\omega = 2\pi j/n$, and t_k are the corresponding discrete time points given by $t_k = \frac{2\pi k}{n\Delta\omega}$. When the spectral amplitudes are known, reconstructing the time-domain fields becomes a phase retrieval problem with $2N$ unknown phase values. The problem is typically addressed by measuring four spectral quantities: the individual spectra, $|F_1(\omega)|^2$ and $|F_2(\omega)|^2$, their direct interference, $|F_3(\omega)|^2 = |F_1(\omega) + F_2(\omega)|^2$, and the interference of the two fields, one of which affected by a $\pi/2$ phase shift, $|F_4(\omega)|^2 = |F_1(\omega) + iF_2(\omega)|^2$. However, as shown in Ref. [160], only the first three quantities are strictly necessary, as the fourth can be retrieved from them (see below). The algorithm aims at recovering the spectral phases of the fields, namely $x_1(\omega_j) = \exp(i\phi_1(\omega_j))$ and $x_2(\omega_j) = \exp(i\phi_2(\omega_j)) \in \mathbb{C}^n$, by minimizing a suitable quadratic function, *i.e.* solving a linear system of equations. The four spectral measurements defined above provides an estimate of the relative phase between the signals. In fact, indicating the estimators of the phases as $\hat{x}_1(\omega_j), \hat{x}_2(\omega_j) \in \mathbb{C}^n$, and omitting from

now on their dependence on ω_j, the following relation holds

$$\hat{x}_1 = \hat{x}_2 \tilde{G}(\omega_j) \tag{5.2}$$

with $\tilde{G}(\omega_j)$ defined as

$$\tilde{G}(\omega_j) = \frac{|F_3|^2 + i|F_4|^2 - (1+i)(|F_1|^2 + |F_2|^2)}{2|F_1||F_2|} = \frac{F_1 F_2^*}{|F_1 F_2|} \tag{5.3}$$

Equation 5.2 corresponds to having a set of N linear equations in the form

$$|F_1||F_2|\, \hat{x}_1 = F_1 F_2^*\, \hat{x}_2 \tag{5.4}$$

The CS constraints provides additional equations. In fact, the estimates of the signals over a CS of width τ are defined as

$$\hat{f}_i(t_k) = \frac{1}{n} \sum_j |\tilde{F}_{1,2}(\omega_j)| \hat{x}_{1,2}(\omega_j) e^{i\omega_j t_k} \qquad \text{with } \; i = 1, 2 \tag{5.5}$$

Since the signals are known to vanish outside the temporal CS of duration τ, this condition provides an additional set of $2N - 2\tau$ equations. In the VPR algorithm, the solution is obtained by minimizing the residuals associated with the out-of-support signal components. Specifically, for $t_k > \tau$, the residuals are defined as

$$R_i(t_k) = R_i(t_k | \hat{x}_1, \hat{x}_2) \qquad \text{with } \; i = 1, 2 \tag{5.6}$$

where each $R_i(t_k)$ quantifies the deviation of the estimated signal from zero outside the known support. The interference information, instead, can be expressed in the form of residual as:

$$R_3(\omega_j) = \hat{x}_1(\omega_j) - \hat{x}_2(\omega_j)\, \frac{\tilde{G}(\omega_j)}{|\tilde{G}(\omega_j)|} \tag{5.7}$$

where $R_3 \neq 0$ in presence of noise. Using these expression, the quadratic functional to be minimized is defined as the weighted sum of the residuals over their variances $V_{1,2,3}$:

$$Q_\tau(\hat{x}) = \sum_{t_k > \tau} \frac{|R_1(t_k)|^2}{V_1} + \frac{|R_2(t_k)|^2}{V_2} + \sum_{j=1}^{N} \frac{|R_3(\omega_j)|^2}{V_{3,j}} \tag{5.8}$$

The problem is an over-determined system of $3N - 2\tau$ equations for $2N$ unknowns with unique solution when $N > 2\tau$ [160]. The residuals are linear in the unknown phase vectors, therefore the minimizing functional is a quadratic (convex) function of these variables. From a computational point of view, the optimization (minimization) of a convex functional is a problem with a unique solution that can be solved efficiently

through least squares minimization. More details on the solution method adopted for the VPR algorithm are reported in [159].
So far, a known compact support of length τ has been assumed, however, estimating τ is a crucial part of the VPR algorithm. In practice, all possible supports of length s are scanned, meaning that the corresponding Q_s is minimized for each s. For $s = \tau$, the correct phase vector is the unique vector that gives exactly $Q_\tau = 0$, hence the correct phase. This means that the minimization problem is repeated over several possible length of the compact support and the solution is that length s that gives the minimal residuals.
As mentioned early in this section, the fourth measurement is not strictly required [160]. In fact, from Eq. 5.3:

$$\tilde{G} = \frac{\hat{x}_1}{\hat{x}_2} = \frac{F_1 F_2^*}{|F_1 F_2|} \tag{5.9}$$

where the product $F_1 F_2^*$ can be written as

$$\Re\{F_1 F_2^*\} = \frac{1}{2}(|F_3|^2 - |F_1|^2 - |F_2|^2) = |F_1||F_2| \cos\phi_{12} \tag{5.10}$$

$$|\Im\{F_1 F_2^*\}| = \sqrt{|F_1|^2 |F_2|^2 - \Re\{F_1 F_2^*\}} \tag{5.11}$$

Retrieving $F_1 F_2^*$ then becomes a *sign* problem. For some cases, the phases can be retrieved even without solving the sign problem (see pulses at zero delay in Ch. 6 and Ref. [62]). However, more generally the *sign ambiguity* has to be solved with dedicated methods, as the one reported in App. C.

5.2 Examples of reconstructions from literature

This section presents two illustrative cases from the literature that help clarifying the DBH method and its extension to single-shot FEL pulse reconstruction, which is discussed in the next chapter.

5.2.1 One-dimensional implementation: attosecond pulse reconstruction

The first reconstruction of attosecond pulses has been shown through numerical simulations in Ref. [162] where the authors considered two attosecond pulses generated from the alignment of CO_2 molecules and their interference. Later, the first experimental demonstration has been reported in Ref. [62]. In this case, the three fields are defined as: an HHG spectrum generated in argon, an HHG spectrum generated

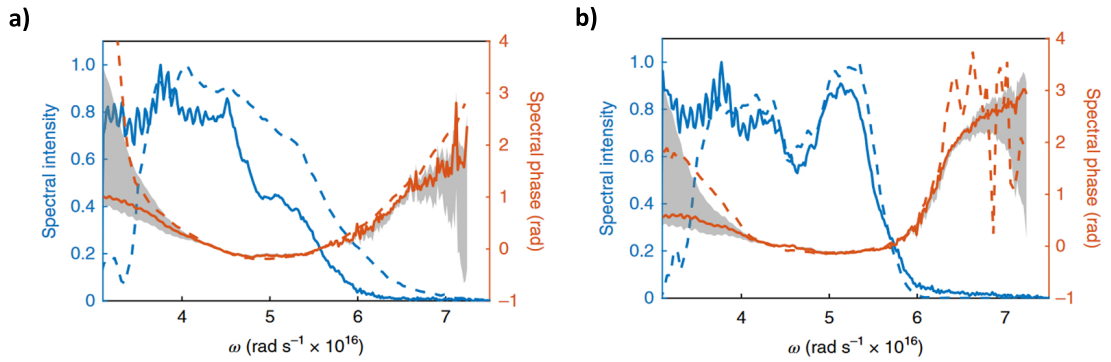

Figure 5.2: *Reconstructed spectral phase and intensity of HHG fields in* ***(a)*** *Ar, and* ***(b)*** N_2 *from DBH (solid lines) and FROG-CRAB (dashed lines). The gray areas indicate the uncertainty interval in the phase given by the choice of the compact support width. The extremes correspond to a CS width shifted by* ± 80 *as from the optimal width. Reproduced from [62] with permission from Springer Nature.*

in nitrogen, and an HHG spectrum generated in a mixture of the two gases using the same driving field. This scheme ensures full independence of the fields and a unique solution without sign ambiguity, as the signals are intrinsically at zero delay (trivial ambiguities excluded, *i.e.* circular shifts of N/2 [160]). On top of being the first experimental demonstration of DBH for attosecond pulse reconstruction, the experiment is relevant to this discussion as the result obtained have been directly compared with Frequency Resolved Optical Gating for Complete Reconstruction of Attosecond Bursts (FROG-CRAB) retrievals [164, 165] performed during the same experimental campaign. The very good agreement between the outputs from the two methods (Figure 5.2) proves the efficacy of the DBH approach, with the perspective of extending it to more complex scenarios where scanning approaches are not possible.

Moreover, in the same experimental campaign, two attosecond pulses generated in argon by shifting the CEP of the driver to $\pi/2$ have been reconstructed from a single-shot measurement. In this case, the approach relies on the fact that the two pulses, even though generated by the same driver and in the same medium, are independent: in fact, by introducing a CEP of $\pi/2$, the HHG pulses generated are separated by half optical period of the driving field (1.35 fs), which is more than twice their individual compact support length. The three fields are retrieved from the Fourier temporal domain by isolating the (sum of) single-object autocorrelations and the cross-correlations (two side bands) of the pulses and transforming back the three separated objects. This method is the extension to the temporal domain of the two-dimensional DBH approach adopted in diffraction imaging [63, 163] that is introduced in the following section.

5.2.2 Two-dimensional implementation: coherent diffractive imaging

The first experimental studies of DBH have been performed for coherent diffractive imaging, *i.e.* the spatial domain [63, 163]. In this case, the three well-separated objects are defined in the Fourier space (x, y) of the measured diffraction image as: (1) the sum of the autocorrelations of the single objects A, B (main central lobe), (2) and (3) the cross-correlations of the objects (side lobes, note that $A \star B \neq B \star A$). Additionally, the CS is defined in Fourier space as a masking area (literally a mask of 0 and 1) that isolates the objects. The concept is illustrated in Figure 5.3 adapted from [63]. The first panel shows the two objects to be imaged, the second one is the diffraction pattern collected at the detector, and the last panel shows the Fourier Transform (FT) of the diffraction, *i.e.* the autocorrelation of the total signal. The algorithm, as presented in the first section of this chapter, runs on the objects obtained by inverse Fourier transforming the masked objects, *i.e.* in the diffraction image space. The cross-correlations correspond to the the product of one object by the complex conjugate of the other, A^*B and AB^*, and can be seen as the interferences. The autocorrelation is instead equivalent to $|A|^2 + |B|^2$, and the fourth object is retrieved from the others by the difference of the two individual objects $|D_{A,B}| = |A|^2 - |B|^2$. The sign problem is solved by making analogous assumptions to what is reported in Appendix C, *i.e.* the signal can change sign only at zero-crossing points (minima of $|D_{A,B}|$), and it is constant over portions of the signal (segments) in between. It has a unique solution for sufficiently high over-segmentation, meaning sampling at least at double the Nyquist rate plus the number of segments M, $N > 2\tau + M$.
In Ref. [63], the authors directly compared the reconstructed objects with the original one, finding very good agreement. Additionally, Monte Carlo and perturbative numerical simulations have been performed, confirming the validity and robustness of the method against noise.
Scaling the problem to the two dimensions has a significant impact on the computational requirements, as the optimal CS length for the two objects needs to be scanned on both x and y axes in the autocorrelation plane. This means solving $T_x^2 T_y^2$ minimization problems, where T_x and T_y represent the dimensions in x and y of the compact support, squared to consider all possible combinations for both original objects. The problem can be solved by utilizing the two-dimensional Fast-Fourier Transform (FFT) algorithm, which is standardly available in most programming languages. Alternatively, it can be performed row-by-row and column-by-column as one-dimensional problems, and then the solutions can be merged together [163]. In

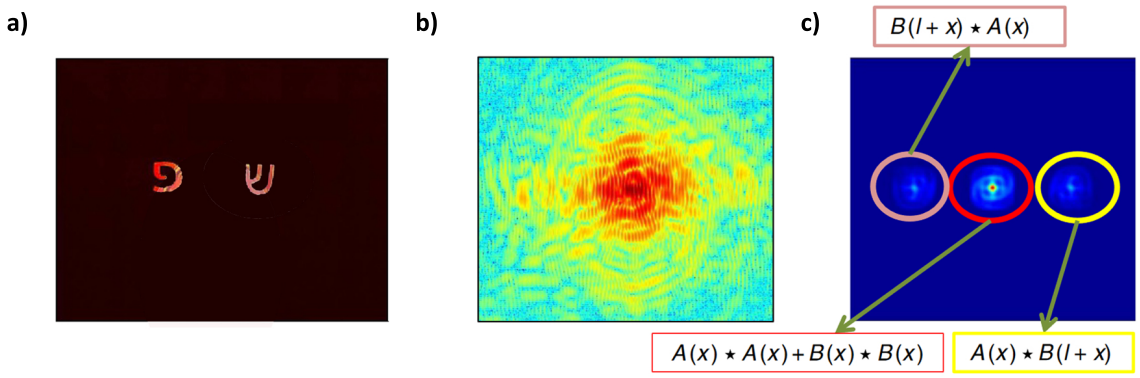

Figure 5.3: ***(a)*** *Two separated objects with non-trivial phases to be imaged and then reconstructed (nm scale).* ***(b)*** *The diffraction pattern of (a) collected at the detector.* ***(c)*** *The FT of the diffraction pattern, i.e. the autocorrelation of the signal, composed by the sum of the autocorrelation of the individual signals (red circle), and their cross-correlations (pink and yellow circles) with the signal B, including a shift "l" in space corresponding to a shift in phase. Illustration adapted and reproduced from [63] under the Creative Commons Attribution 4.0 International License.*

the work presented in the next chapter, the VPR algorithm is applied directly to the two-dimensional map. Since every iteration over the CS dimension can be viewed as an independent VPR problem, the computation has been parallelized by exploiting the server cluster system *Maxwell* available at the Deutsches Elektronen-Synchrotron DESY (Hamburg, Germany), reducing the overall computational time to just a few minutes.

Based on the theoretical framework presented so far, the next chapter extends the DBH method to the single-shot reconstruction of SASE-FEL pulses.

6 | Experiment: DBH of ultrashort Free-Electron Laser pulses

Building on the fundamentals of DBH previously illustrated in Ch. 5, this chapter presents and discusses the application of DBH to ultrashort FEL pulses. The experiment showcases the method as a delay tagging tool and pulse characterization technique, with the potential to extend it to spectroscopic applications.

6.1 Experimental setup

The experiment has been performed at the FEL facility FLASH2 (Hamburg) at the beamline FL26 under the proposal F-20220697. FLASH2 is a SASE FEL delivering a train of pulses at 10 Hz with repetition rate within the train up to 1 MHz. This kind of source is affected by high spectral and temporal jittering [166, 167], meaning that the delivered pulses change shot to shot.
In our experiment, the three fields used for the DBH method are the spectrum of the FEL source, the spectrum of an HHG source, and their interference. Recalling the two main requirements for DBH presented in Ch. 5, the independency of the objects is satisfied by the fact that these are independent sources, while the temporal domain constraint is satisfied by the finite ultrashort duration of both HHG and FEL pulses, the latter mostly operated in single-spike mode [47]. The beamline [168] chosen for the experiment has been originally designed for XUV-pump/XUV-probe transient absorption spectroscopy and coincidence measurements in gas targets, and it makes use of an HHG source covering up to 40 eV synchronized with the FEL beam itself. By implementing a specific alignment of the beamline, it has been possible to spectrally, temporally and spatially overlap the two independent HHG and FEL sources directly at the detector, consisting of a CCD camera with a 20 μm pixel

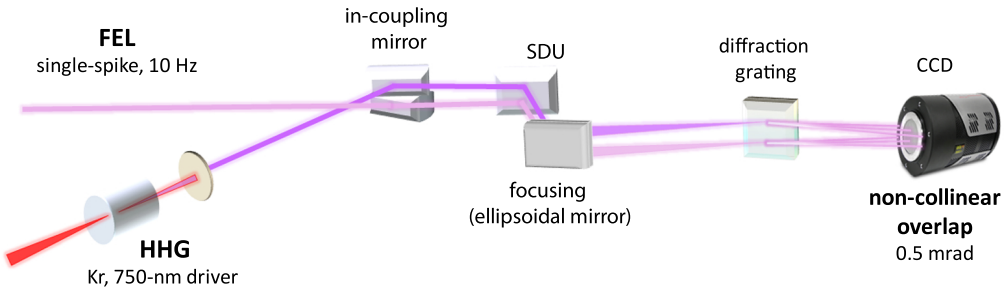

Figure 6.1: *The HHG beam and FEL beam are spatially overlapped at the detector (CCD) in a non-collinear geometry (0.5 mrad) after being spectrally dispersed by a diffraction grating. In-coupling and focusing mirrors are ensuring control over the beams direction and focusing, while the split-and-delay unit (SDU) is used together with the laser synchronization system to control the delay between the pulses. The system is operating at 10 Hz, with the FEL in single-spike mode and matching harmonic number 21 (34.5 eV) in Kr driven by 750-nm OPCPA.*

size (Teledyne, PIXIS). The individual spectra and their interference were simultaneously collected on a single-shot basis after energy dispersion through a grating. The beams were overlapped in a non-collinear geometry (0.5 mrad), which allows for encoding information on the phase on the vertical spatial coordinate - a relevant aspect that will be discussed in more detail in Section 6.3. The temporal overlap was controlled through the laser synchronization system and the so-called split-and-delay unit (SDU), a plane motorized mirror controlling the HHG and FEL paths. Exploiting the capabilities of the beamline, time zero, *i.e.* the instant of zero delay between the two pulses, has been determined by measuring a transient absorption cross-correlation trace in argon. On the other side, the spectral overlap is ensured by tuning the FEL undulator to match one of the harmonics of the broadband HHG source. The FEL machine has been operated in single-to-few spike mode [47] in order to avoid a spectral modulation accidentally matching the periodicity of the spectral interference fringes, thus hindering the DBH retrieval. More specifically, the single-spike FEL pulses delivered at 10 Hz spectrally overlap with the harmonic 21^{st} at 34.5 eV. The HHG spectrum is generated in Kr in a semi-infinite gas cell by the OPCPA FEL-synchronized source offered at FLASH2 and centred at 750 nm. A schematic of the beam steering and alignment to the detector is reported in Figure 6.1. Figure 6.2 reports instead the three spectra as collected and overlapped at the detector. The top panels show full maps as a function of energy and spatial coordinate, the bottom panels show the normalized spectra obtained by integrating the signal along the vertical pixels. The maps of the single beams (right and central panels in the top row) are recorded only for calibration and alignment purposes. The HHG spectrum is broader than the FEL one, a necessary condition to the reconstruction of the latter field. In fact, the interference contains information on the relative phase of the fields

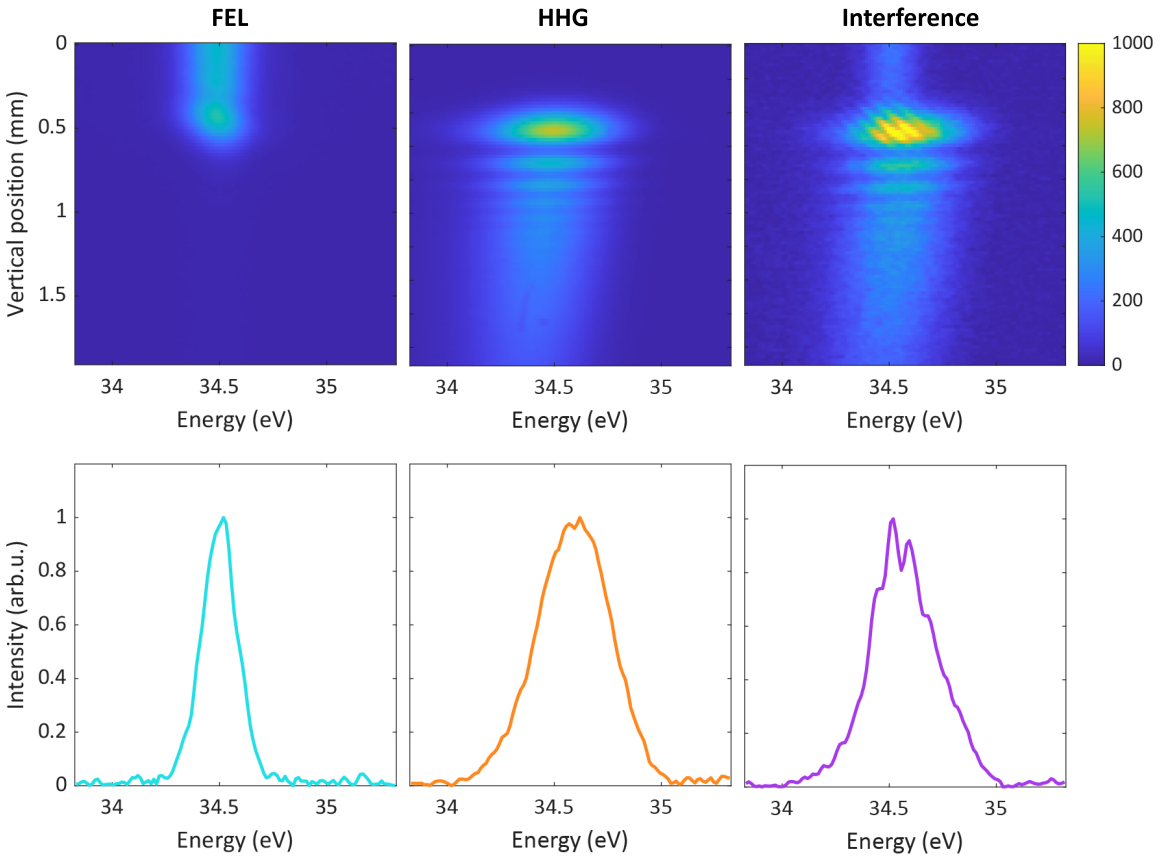

Figure 6.2: *Top: FEL, HHG, and interference spectra as a function of energy and vertical coordinate as recorded at the detector. Bottom: normalized integrated spectra corresponding to the spectral maps in the first row.*

at energy whose amplitude is non-null (see Eqs. (5.2) and (5.3)). This means that a spectrally broader harmonic spectrum ensures the collection of full information on the FEL spectrum, while the non-overlapping portion of the HHG spectrum cannot be reliably reconstructed.

6.2 Timing tool

The DBH trace intrinsically carries information on the delay between the two pulses. In fact, when calculating the autocorrelation of the signal (two-dimensional FT) the two cross-correlation peaks given by $f_1(t + \Delta t, k_y + \Delta k_y) \star f_2(t, k_y)$ and $f_2(t, k_y) \star f_1(t + \Delta t, k_y + \Delta k_y)$ are centred at $(\pm\Delta t, \pm\Delta k_y)$, where t is the time and k_y the vertical momentum, and Δt and Δk_y are the shifts in time and vertical momentum with respect to the centre of the FT. The autocorrelation signal of the interference map of Fig. 6.2 (top right panel) is reported in Figure 6.3 as directly obtained from the

two-dimensional FT without filtering or background removal. The exact temporal delay between the pulses is determined by fitting the cross-correlation lobes (either the positive or negative one) with a Gaussian function. While the residual fitting error is on the order of 0.3 fs, the actual precision is ultimately limited by the width of the spectral window used. In the maps presented so far, the temporal resolution obtained from the FT is 2.75 fs. This value reflects a compromise between temporal resolution and noise suppression: widening the spectral window to include noisy regions reduces the contrast of the autocorrelation signal. The intrinsic ambiguity on the sign of the retrieved delay is considered a trivial ambiguity of the DBH method corresponding to a circular time shift [159].
By repeating this procedure for each acquired shot, it has been possible to correlate the time delay obtained from the autocorrelation with the estimations of the Beam Arrival Monitor (BAM) and Laser Arrival Monitor (LAM), *i.e.* the electronic monitors synchronizing the FEL and HHG beams. The result is reported in Figure 6.4, where the orange dots mark the data used in the correlation while the blue dots are outliers. The delays from the FT have been defined from the lobe at positive vertical momentum, thus leading to a negative linear correlation (coefficient -1) with the BAM-LAM difference. Choosing the other lobe would give a positive correlation. The Root-Mean-Squared Error (RSME) from this correlation is 7 fs, thus benchmarking the excellent performances of the time synchronization unit at FLASH2, which effectively compensates for the time jittering of the SASE-FEL, usually covering tens of femtoseconds.
In perspective, this method can be used as a delay tagging tool to be implemented in parallel to a main experiment, similarly to other timing tool techniques [49, 169–172].

6.3 Pulse reconstruction

In this experimental campaign, the DBH method has been used to reconstruct single-shot SASE-FEL pulses. Both one-dimensional and two-dimensional reconstruction methods have been adopted (see Sect. 5.2) covering complementary cases. In fact, on the one hand, the one-dimensional retrieval is affected by sign-ambiguity when the two pulses are delayed (see Ch. 5 and App. C), on the other hand, the two-dimensional retrieval cannot be applied for pulses at 0-fs delay, *i.e.* overlapping in time. In the latter case, the autocorrelation map in time and vertical momentum would lack the side lobes from the cross-correlations, displaying only the main lobe resulting from the sum of the individual autocorrelations. This makes it impossible

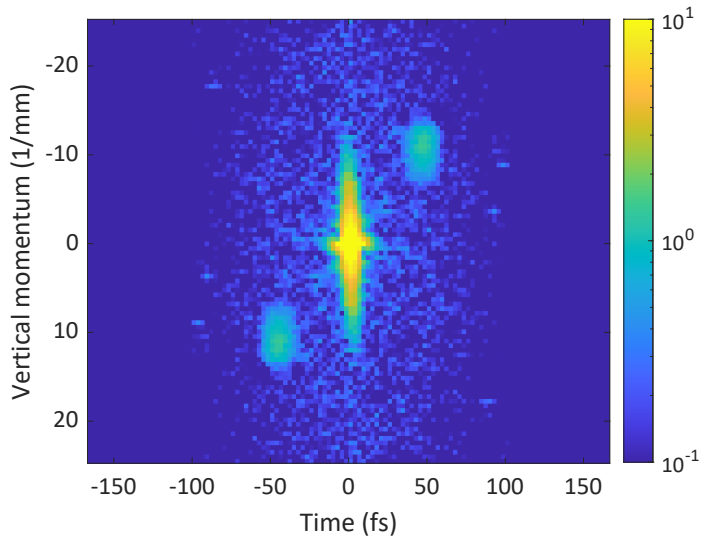

Figure 6.3: *Autocorrelation (two-dimensional FT) of the interference signal of Fig. 6.2 (top right panel). The main lobe corresponds to the sum of the autocorrelations of the individual signals, while the side lobes correspond to the cross-correlations. The delay is retrieved by Gaussian fitting of the cross-correlation lobe at positive vertical momentum (in this case, giving a positive delay).*

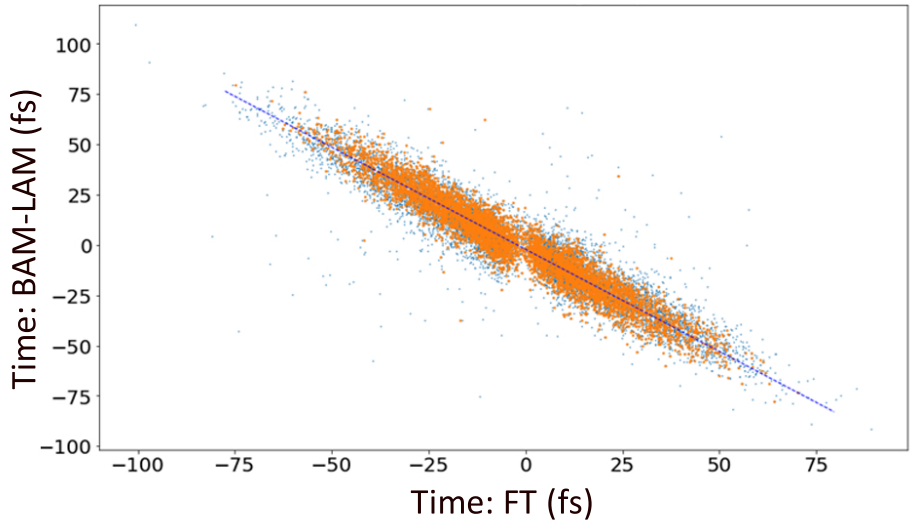

Figure 6.4: *Correlation plot between the delay as retrieved from the signal autocorrelation map, i.e., the FT, of the measured signal, and the delay as from the BAM and LAM that are controlling and monitoring the synchronization of the beams. The quantities are linearly correlated with a RMSE of 7 fs. The orange dots are the points actually used for the linear fitting, removing the outlier shown in blue.*

to distinguish the three independent objects required for reconstruction. The results from both methods are presented below.

6.3.1 One-dimensional FEL reconstruction

The spectra used in the one-dimensional reconstruction algorithm are obtained starting from the two-dimensional images of the individual HHG and FEL signals and their interference, as reported in Fig. 6.2 (top row). The integrated spectra are obtained by rescaling the intensity outside the overlap region to match the intensity that actually interferes with the other beam. This correction accounts for possible spatial inhomogeneities in the beam profile. For the FEL beam,the scaling factor is usually 1 to 1.2, as the spatial profile is rather homogeneous, especially when in single-spike mode. For the HHG, the intensity at the interference region is retrieved from the relative intensity of the harmonic collected without the FEL beam (middle column Fig. 6.2), as, contrary to the FEL jittering shot-to-shot, the harmonic signal is very stable and reproducible. To reduce high-frequency fluctuations, a moving average filter with a width of 5 data points has been applied to the three spectra using a convolution function. The baseline has also been removed. The resulting spectra from this procedure are shown in Figure 6.5a, with the FEL spectrum in light-blue, the HHG one in orange and their interference in purple. The absence of fringes in the latter spectrum is due to the overlap in time of the two pulses. Their constructive interference is ensured by the higher intensity of the interference signal compared to the incoherent sum of the separate HHG and FEL intensities. The reconstruction algorithm has been applied exactly as illustrated in Section 5.1 without the necessity of applying any sign correction (see App. C). Although the method provides reconstruction for both fields, HHG and FEL, the reconstruction of the harmonic, having a shorter duration, is considered unreliable due to its partial spectral overlap with the FEL. Panels *b* and *c* of Fig. 6.5 present the results of the FEL pulse reconstruction. Panel *b* shows the spectral phase plotted against the corresponding spectrum as retrieved from the code. The phase has a positive chirp of about 15 fs^2. The corresponding temporal profile is shown in panel *c*. The retrieved pulse has a duration of 10.4 fs, compared to a Transform-Limited (TL) duration of 7.0 fs. The result agrees with the expected performances for the FEL machine settings.

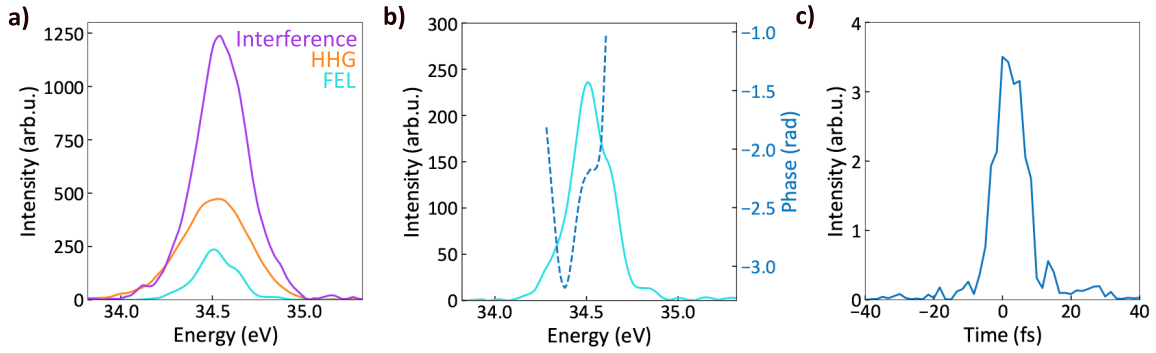

Figure 6.5: *One-dimensional reconstruction of the FEL pulse.* ***(a)*** *The three integrated spectra from a single-shot measurement at 0-fs delay (no fringes): interference (purple), HHG (orange), FEL (light blue).* ***(b)*** *Reconstructed temporal profile of the FEL pulse with a FWHM duration of 10.4 fs (TL: 7.0 fs).* ***(c)*** *Reconstructed spectral phase (dashed blue line) plotted against the measured FEL spectrum, as shown in panel (a).*

6.3.2 Two-dimensional FEL reconstruction

The two-dimensional maps collected by the detector contain more information than the three spectra used in the one-dimensional reconstruction. This is a consequence of the non-collinear geometry implemented in the experiment. In fact, when two chirped (linearly dispersed) pulses interfere non-collinearly in space and time, the interference pattern measured as a function of spatial coordinate and energy exhibits fringes with a curvature that encodes the relative Group Delay Dispersion (GDD) of the pulses. In fact, the interference signal between two beams, $E_1(y,\omega)$ and $E_2(y,\omega)$ displaced by a (vertical) angle θ is defined as:

$$\begin{aligned} I(y,\omega) &= |E_1(y,\omega) + E_2(y,\omega)|^2 \\ &= |E_1(y,\omega)|^2 + |E_2(y,\omega)|^2 + 2|E_1(y,\omega)||E_2(y,\omega)|\cos[\Delta\Phi(y,\omega)] \end{aligned} \tag{6.1}$$

where

$$\Delta\Phi(y,\omega) = \Delta k_y(\omega)\cdot y(\omega) + \Delta\phi_{1,2} \tag{6.2}$$

is the relative phase between the beams, with $\Delta k_y(\omega) \approx k(\omega)\theta = (\omega/c)\theta$ the difference in the transverse wave vectors approximated for small angles ($\sin\theta \approx \theta$ in radians), and $\Delta\phi_{1,2}$ the difference in the spectral phases of the pulses. By definition, the frequency components of a chirped pulse are affected by a frequency-dependent delay with respect to the central frequency ω_0 arriving at τ_0, which is given by

$$\tau_g(\omega) = \left.\frac{\partial\phi}{\partial\omega}\right|_{\omega_0} + \left.\frac{\partial^2\phi}{\partial\omega^2}\right|_{\omega_0}(\omega-\omega_0) = \tau_0 + GDD\,(\omega-\omega_0) \tag{6.3}$$

with the corresponding spectral phase (its integral) given by

$$\phi = \tau_0 \left(\omega - \omega_0\right) + \frac{1}{2} GDD \left(\omega - \omega_0\right)^2 \quad . \tag{6.4}$$

From the definitions above and considering pulses centred at approximately the same ω_0, the difference in phase in Eq. (6.2) can be ultimately written as

$$\Delta\Phi(y,\omega) \approx k(\omega)\, \theta\, y(\omega) + \tau_{1,2} \left(\omega - \omega_0\right) + \frac{1}{2} GDD_{1,2} \left(\omega - \omega_0\right)^2 \tag{6.5}$$

where $GDD_{1,2}$ is the relative group delay dispersion between the pulses, *i.e.* $(GDD_1 - GDD_2)$ and $\tau_{1,2}$ is their relative time delay at ω_0, *i.e.* $(\tau_{0,1} - \tau_{0,2})$. The maxima of the interference signal $(\partial I(y,\omega)/\partial y = 0)$ correspond to those points for which $\cos[\Delta\Phi(y,\omega)] = 1$ and therefore $\Delta\Phi(y,\omega) = 0$ or integer multiples of 2π. Their vertical position as a function of the frequency is therefore given by

$$y(\omega) \approx -\frac{c}{\omega\, \theta} \left[\tau_{1,2} \left(\omega - \omega_0\right) + \frac{1}{2} GDD_{1,2} \left(\omega - \omega_0\right)^2\right] \quad . \tag{6.6}$$

In the interferogram $I(y,\omega)$, this results in interference fringes that bend as a function of frequency, forming a semi-parabolic pattern whose curvature is proportional to the relative GDD. In the experimental conditions here considered, the GDD giving rise to the observed curvature can, to a good approximation, be ascribed entirely to the FEL pulse. This is justified by the fact that, knowing the beams propagate in vacuum and do not encounter any additional dispersive elements before detection, the harmonic field is only influenced by its intrinsic atto-chirp (see Ch.2), which is typically small, *i.e.* in the order of $\sim$1 fs^2[164, 173, 174]. Two examples of experimental interferograms showing this effect are reported in Figure 6.6.

The relative GDD between the pulses, $GDD_{1,2}$, can be extracted by fitting the positions of the interference maxima using Eq. (6.6). However, the convergence and reliability of this fit are highly sensitive to factors such as the sampling rate and the presence of noise, often making the procedure challenging to apply without imposing strict constraints on the fitting parameters. For this reason, alternative approaches like DBH, which do not rely on prior assumptions about the dataset, offer a more robust and attractive solution for pulse reconstruction.

The VPR algorithm is applied as illustrated for the case of diffraction imaging in Sect. 5.2, to which the reader is referred for further details. In summary, the CS is employed to map and isolate the cross-correlations and autocorrelation sum in the Fourier space. The algorithm is then applied in the spectral domain in two dimensions, after having transformed back the three isolated signals. The optimal CS has

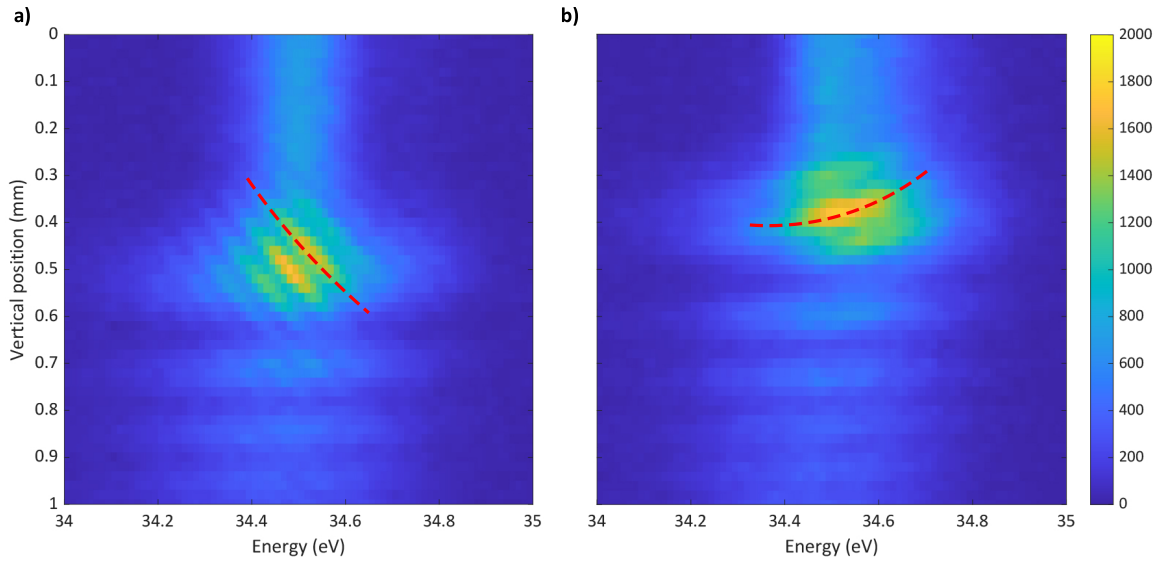

Figure 6.6: ***(a,b)*** *Two experimental interferograms $I(y,\omega)$ as function of the energy and vertical displacement. In the left panel, the vertical displacement of the fringes' maxima increases with energy, while in the right panel, it decreases with energy (note that the vertical axis is set to 0 at the top). The behaviour is highlighted by the dashed red lines.*

been found by scanning the two dimensions and evaluating it through the *leakage score error* defined as

$$Err = \frac{||Rec_{HHG}||^2_{out} + ||Rec_{FEL}||^2_{out}}{||Rec_{HHG}||^2_{tot} + ||Rec_{FEL}||^2_{tot}} \tag{6.7}$$

This error quantifies the amount of signals left outside the CS (Rec_{out}) with respect to the total signals (Rec_{tot}). Typical values are in the order of 0.1-0.2.

To reduce sources of noise in the reconstruction, instead of using the autocorrelation trace from the direct FT shown in Fig. 6.3, a supergaussian apodization has been applied in the spectral domain to isolate the interference pattern. This improves the convergence of the method by cleaning the trace of noise in a manner similar to the moving average applied in one-dimensional reconstruction. The result of the apodization on the autocorrelation trace reported in Figure 6.3 is illustrated in Figure 6.7, where the background is reduced and the contrast sensibly improved with respect to the untreated data.

The reconstruction of the FEL pulse is reported in Figure 6.8. The profile corresponds to the integration along the vertical axis of the two-dimensional reconstructed maps (y,ω) obtained from the algorithm. Panel *a* shows the retrieved spectral phase (dashed line) plotted against the normalized experimentally measured spectrum (solid light-blue line) and the reconstructed spectral profile (shaded area). The reconstructed phase gives a GDD of about 12 fs^2. The retrieved spectral bandwidth

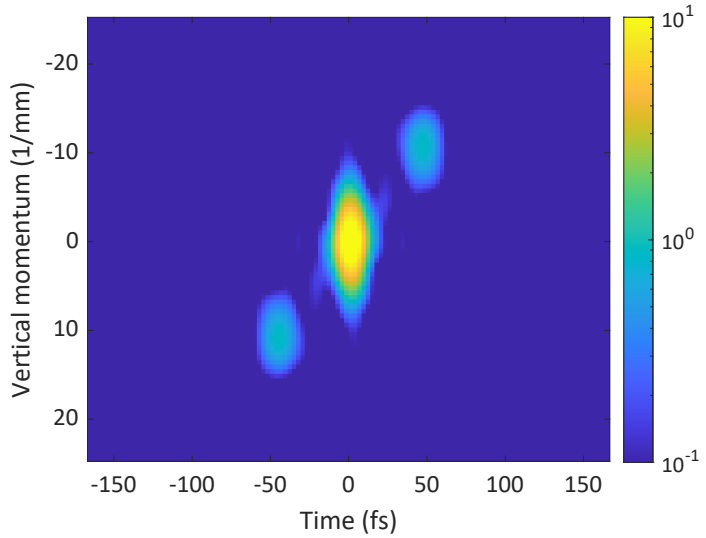

Figure 6.7: *Apodization (supergaussian filtering) of the autocorrelation signal reported in Fig.6.3. Applying apodization to the two-dimensional spectral map of Fig.6.2c filters out the interference pattern from the rest of the map, leading to improved contrast of the autocorrelation signal and a reduced background.*

closely matches the measured one, providing an immediate benchmark on the quality of the reconstruction. Panel *b* shows the temporal profile of the FEL pulse as obtained from FT of the spectral profile: the dashed line reports the TL Gaussian profile with a duration of 8.9 fs, the solid line corresponds to the reconstructed temporal profile using the phase obtained from the VPR algorithm (dashed line in panel *a*) and the measured spectral intensity, providing a duration of 10.4 fs, while the shaded area corresponds to the temporal profile obtained with the reconstructed phase and reconstructed spectral intensity, resulting in a duration of 10.1 fs. To avoid aliasing effects in the FT and improve the convergence of the Gaussian fits used to define the FWHM durations, the temporal axis sampling has been enhanced through interpolation, reducing the time step from 2.8 fs to 0.03 fs. As mentioned in Ch. 5, every reconstruction is affected by a trivial ambiguity corresponding to a circular time shift [159]. This means that positive-to-negative time flips should also be considered. This trivial ambiguity is generally solved simply looking at the measured experimental trace, and at both the integrated spectrum and the curvatures of the fringes. As for the one-dimensional case, the HHG is not considered reliable due to the lack of information caused by the extended spectral bandwidth not interfering with the FEL beam.

Contrary to Refs. [62, 63], for this experiment, there are no other reconstruction methods that can be used in parallel to benchmark the DBH reconstruction. Nevertheless, various metrics can be employed to evaluate the quality of the reconstruction. The *robustness* is inherited from diffraction imaging where Monte Carlo and perturba-

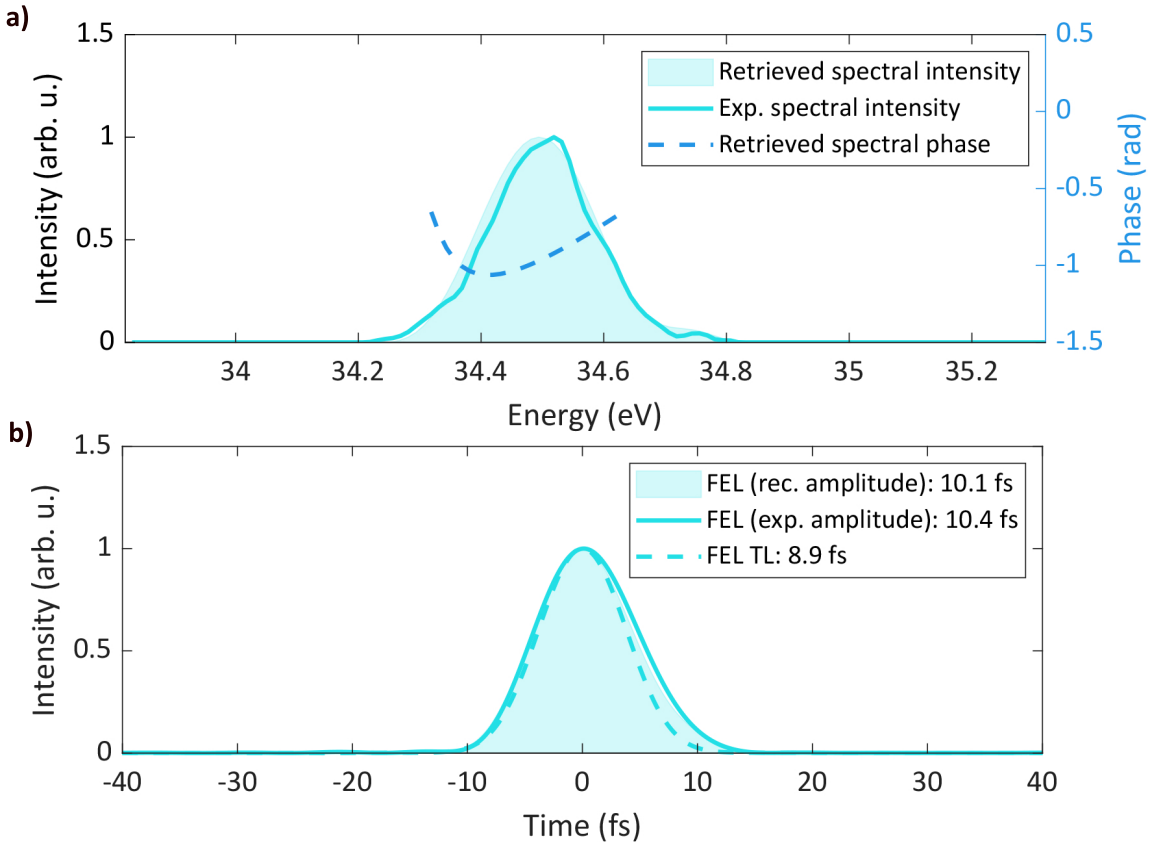

Figure 6.8: *Example of FEL pulse reconstruction with the two-dimensional method.* ***(a)*** *Spectral phase (dashed line) against the normalized measured spectrum (solid line) and the reconstructed spectrum (shaded area).* ***(b)*** *Temporal profile of the FEL pulse: TL Gaussian profile (dashed line), the profile obtained from the reconstructed phase and the measured spectrum (solid line), and the profile obtained from the reconstructed phase and reconstructed spectrum (shaded area).*

tive numerical simulations have been used to benchmark the reliability of the method under noisy scenarios [63, 163]. The *precision* is ultimately defined by the resolution of the spectrometer (0.01 eV); in time, it can be quantified along the several steps leading to the integrated profile shown in Fig. 6.8, *e.g.*, it is in the order of the few attoseconds in the Gaussian fits, but the step size is tens to hundreds of attoseconds. It is ultimately considered in the order of ± 0.1 fs. The *accuracy* is assessed in the first approximation through the comparison between retrieved and measured spectra. Simulations based on the FEL machine settings are ongoing to further validate the reliability and accuracy of the reconstruction.

6.4 Conclusions and perspectives

The experiment presented here demonstrates the effectiveness of the DBH method for reconstructing phases and pulses in more complex scenarios—specifically, those affected by the time and spectral jitter inherent to SASE-FELs. The method is *fully optical*, relying solely on the interference measurement between two pulses, and *linear*, requiring only low field intensities. It also inherently functions as a *delay-tagging* tool. In this case, it has been used to benchmark the performance of the arrival time monitors at FLASH2; however, it could also be implemented independently as a delay control unit within a feedback loop.

The VPR algorithm, used here for phase reconstruction, served as a diagnostic tool to fully characterize SASE-FEL pulses. However, its application is broader and can extend to experimental cases in which the phase associated with an excited state of a material, atom, or molecule is the primary observable under investigation. In this regard, DBH is intended to be applied on the same beamline to measure the phase of Fano resonances [175] in argon, krypton, and their ions. Previous studies using traditional techniques, such as the Reconstruction of Attosecond Beating By Interference of Two-photon Transitions (RABBITT) method [173, 174], have characterized these resonances in neutral atoms using HHG [176]. The higher photon flux currently offered by FEL sources enables the study of more complex systems, including ions, and strong-field regimes known to influence the shape of the Fano resonance. The proposed implementation involves directing the FEL beam to interact with a gas target before interfering with the unperturbed HHG beam at the detector. In this configuration, the amplitude and phase of the electron wave packet generated through the autoionization process in the gas target are encoded in the transmitted FEL pulse. This experiment positions DBH not only as a diagnostic technique but also as a powerful tool for holographic spectroscopy.

PART IV

Conclusions

7 | Future perspectives

This thesis presents advancements in HHG sources, including high-photon energy generation in the water-window spectral region, sHHG spectroscopy of bulk and semi-ordered materials, and characterization of FEL pulses. The work demonstrates the potential of HHG for investigating ultrafast electron dynamics in matter and contributes to the field implementing technical solutions and novel methodologies.

The first part (Chapters 2, 3) introduces a new scheme for HHG in the overdriven regime, utilizing a custom-designed differentially pumped glass chip for efficient gas confinement over sub-millimetre lengths. This approach delivers broadband HHG spectra above the carbon K-edge using long multicycle driving pulses. Driving the generation with the direct output of a commercial Ti:Sapphire laser reduces the technical complexity typically associated with soft X-ray schemes. Given recent advancements in the stability, peak power, and pulse durations of ytterbium (Yb)-based sources, evaluating the performance of the differentially pumped chip with high-repetition-rate Yb-laser systems is a priority for future research. In fact, theoretical models and preliminary simulations indicate the potential to achieve photon energies up to 300 eV with multi-cycle driving pulses. Meanwhile, the current source will be integrated into a transient absorption scheme to study near-edge charge transfer dynamics in solvated molecules (see Appendix A).

As an additional perspective on HHG-based schemes, this thesis (Chapter 4) shows the working principles of sHHG, reporting preliminary results from multiple TiO_2 phases, including bulk crystalline, semi-ordered, and amorphous forms. The experiments aim to reconstruct the valence electronic potential as a function of crystalline ordering and spatial confinement. While the analysis is ongoing and requires both analytical and numerical modelling, initial results reveal significant differences in the harmonic response among the samples. The anisotropic response is determined by the material phase, and the harmonic yield is influenced by the thickness of the amorphous films. In comparison to conventional techniques such as angle-resolved photoemission spectroscopy (ARPES), sHHG is an all-optical method that offers a more accessible approach for characterizing the electronic structure of functional ma-

terials at the nanoscale. The straightforward technical requirements allow for *in situ* and *in-operando* applications, even under extreme conditions [177]. The results on sHHG highlight the relevance of HHG not only as a source of coherent XUV and soft X-ray radiation, but also as a powerful spectroscopic tool. In fact, sHHG is capable of revealing electronic structure variations with nanometre spatial and few–to–sub-femtosecond temporal resolution, a combination rarely achieved by a single technique.

Finally, Chapters 5 and 6 report on the use of DBH to characterize ultrashort FEL pulses via interference with a synchronized HHG source. The work demonstrates the full temporal reconstruction of SASE-FEL pulses on a single-shot basis through a simple iterative routine, the VPR algorithm. This linear optical method can be implemented in parallel with a main experiment as a non-invasive diagnostic tool with sub-femotseocond delay resolution. Beyond diagnostics, further advancements include the application of DBH as a direct spectroscopic technique. In particular, it is planned to employ DBH for single-shot amplitude and phase reconstruction of Fano resonances in argon, krypton, and their respective ions. By extending the concept of attosecond interferometry [178] to FELs, DBH has the potential to become a key technique for high photon energy and high-intensity spectroscopy. In this scenario, a standard HHG source, temporally synchronized with the FEL beam, becomes an important tool for performing such experiments.

HHG sources have found applications in ultrafast spectroscopy [7, 8], microscopy and imaging [179–182], and quantum optics [183–186]. These advances necessitate continued progress to address the evolving requirements of the attosecond science community, which is increasingly looking at the potential of FELs [187, 188]. The findings presented in this thesis contribute to this field by offering new perspectives on HHG sources, from the the development of efficient high-photon energy schemes to advances in spectroscopy and holography.

PART V

Appendices

A | Free molecular flow simulations in COMSOL

As discussed in Section 3.1.1, the design of the differentially pumped chip for HHG in the soft X-ray spectral region has been optimized based on simulations in the Free Molecular Flow regime run on COMSOL Multiphysics [114]. This regime is suitable for describing low-pressure, low-velocity gases for which the mean free path is larger than the object they are moving through, thus making it a critical tool for the design of vacuum systems. When considering high-pressure gases confined in small volumes, the High Mach Number module in COMSOL [189] could be more suitable. This is a critical aspect to retrieve the correct gas profile in the interaction region. Nevertheless, interferometric measurements performed by the collaborators at CNR-Milano have shown that, to a good approximation, the pressure profile of the interaction region can be considered constant [116]. Here, the Free-Molecular flow has been used to estimate the pressure drop from the gas inlet to the outlet (vacuum chamber), and the results are found to be in good agreement with experimental observations. In the experiment, the limitations identified while increasing the input pressure above 3 bar are related to the overall pumping system design of the beamline, which is based on an older design and was not taken into account. The following reports the output simulations (on-axis) obtained while tuning a set of critical dimensions in the chip design.

Pumping areas

Here, the pumping areas of the first stage have been varied, changing their width (*l_chamb1*). The length *x_1* sets the distance between the first and second pumping area and has been varied accordingly to preserve the overall length of the chip. The plot shows the number gas density ($n = P_{gas}/k_B T_{gas}$, with k_B the Boltzmann constant, P_{gas} and T_{gas} respectively the gas pressure and temperature, ambient temperature 298 K) for a neon input pressure of 5 bar. This simulation shows that

enlarging the pumping area (increasing the width, *l_chamb1*) while shortening the distances between the areas is beneficial to the pumping performances (blue curve, Figure A.1).

Output channels diameters

In this simulation run the parameter under investigation is the output channels diameter (*d_ch**) connecting the interaction region with the pumping stages, the pumping stages themselves and the output. Figure A.2 reports the on-axis number gas density as a function of the propagation along the chip for an input pressure of 5 bar of neon. It is clear that a larger diameter is beneficial to the pumping performance (blue curve).

Inlet pressure

Figure A.3 reports the on-axis number gas density as a function of the propagation along the chip (full final design of sect. 3.1.1) while varying the inlet pressure p_{in} of neon. All the cases exhibit a pressure drop of almost four orders of magnitude by the end of the first half of the cell.

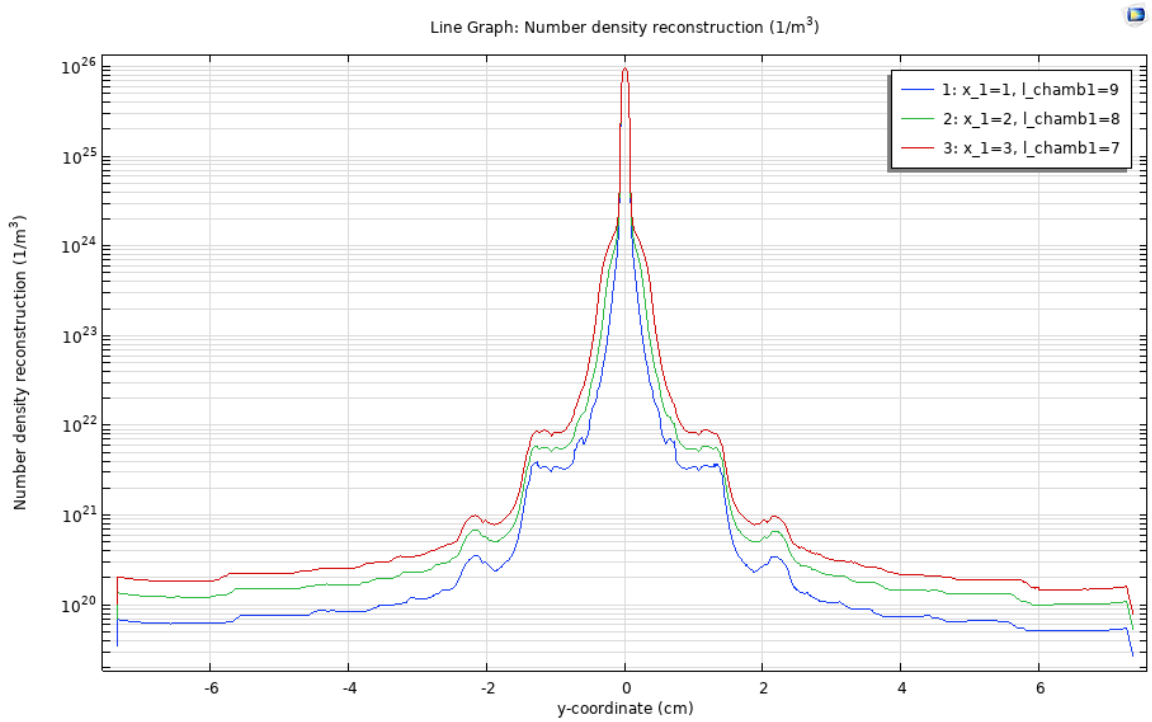

Figure A.1: *On-axis number gas density along the differentially-pumped chip presented in sect. 3.1.1, when varying the pumping area by varying its width (l_chamber1) and by modifying accordingly the pumping stages distance x_1 to preserve the total chip length.*

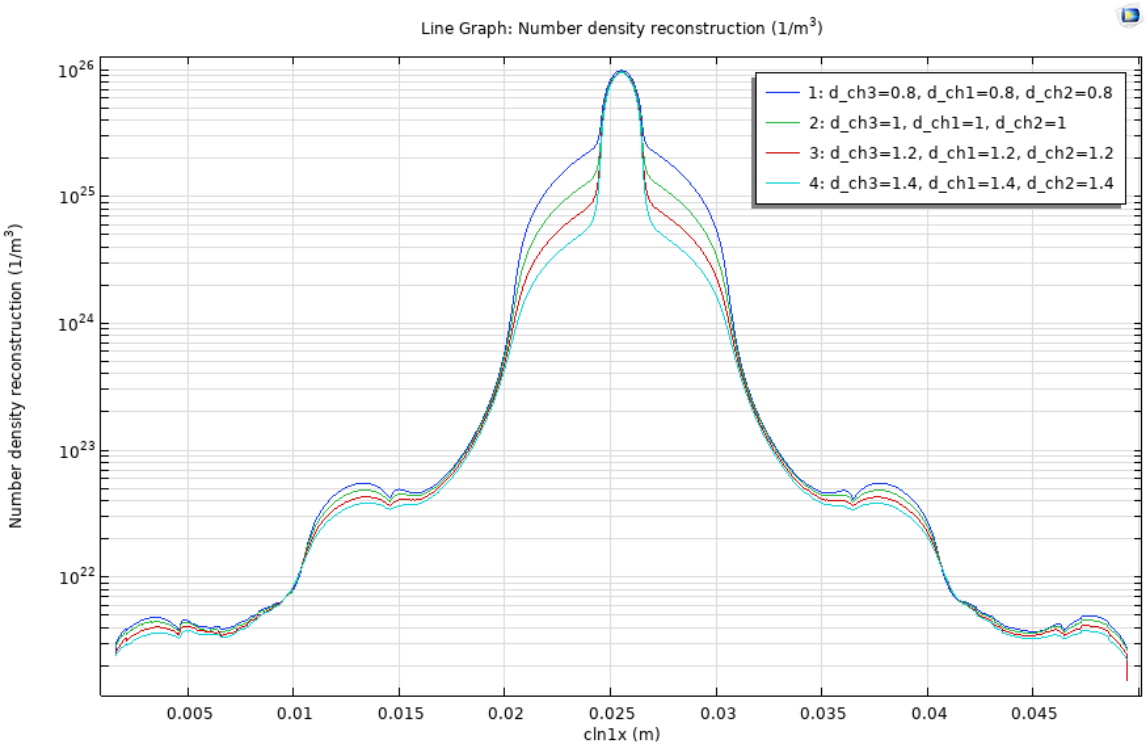

Figure A.2: *On-axis number gas density as a function of the propagation along the chip when varying the output channels diameters from 0.8 to 1.4 mm.*

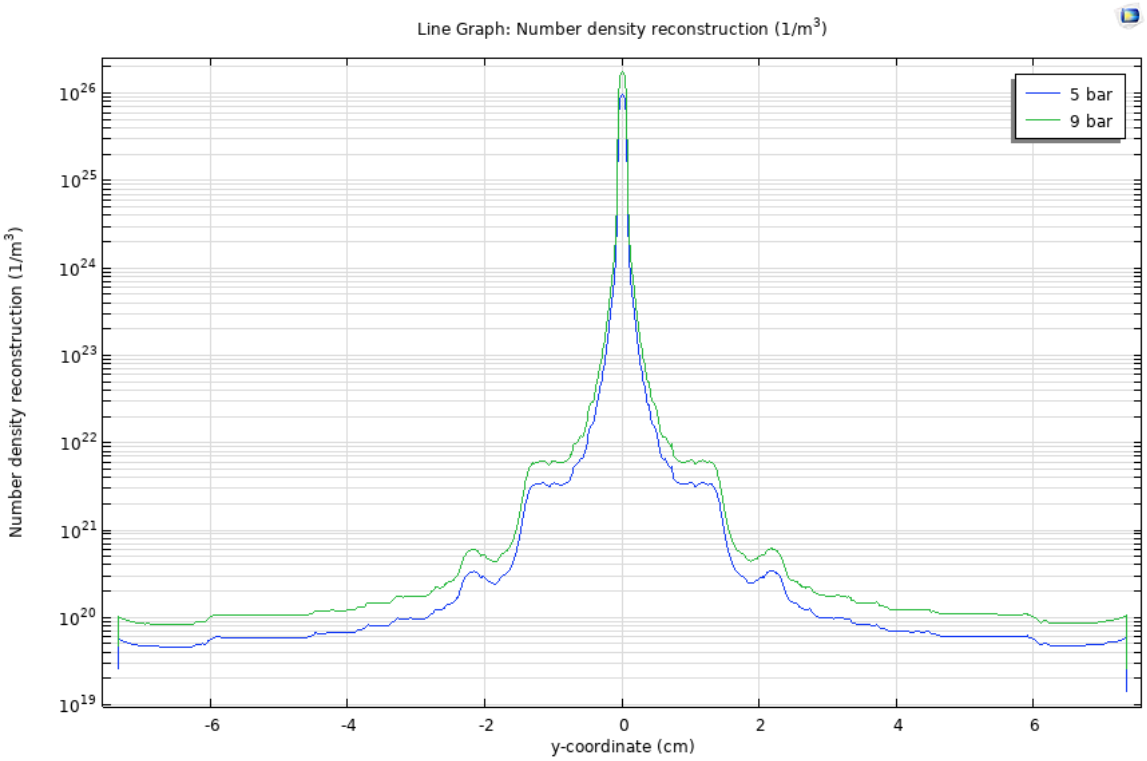

Figure A.3: *On-axis number gas density as a function of the propagation along the chip when varying the inlet pressure between 5 and 9 bar of neon.*

B | Design and development of a transient absorption spectroscopy scheme: UV pump/soft X-ray probe

The HHG source presented in Chapter 3 has been developed as a probe arm of a transient absorption scheme to study charge transfer dynamics in metallic complexes in solution. The pump arm of such a setup will be a few-cycle UV source based on Resonant Dispersive Wave (RDW) emission in fibre [124]. This section provides a brief overview of the design of this UV source and the corresponding beamline schematic.

Solitons are pulses that propagate invariant in time and space and are generated in non-linear media from the perfect balancing of a positive non-linear refractive index with a negative (anomalous) linear dispersion. The interplay between nonlinearity and dispersion along the guided propagation in a fibre can, though, give rise to phenomena such as self-compression, white-light supercontinua generation, and frequency-tunable RDW emission. Given a certain driving pulse to propagate in a gas target in a hollow-core fibre, two parameters dictate the efficiency of the RDW emission. The first is the soliton order defined as $N = (L_d \ / \ L_{nl})^{1/2}$, where L_d is the dispersion length defined as the ration between (natural) pulse duration squared and group-velocity dispersion ($\tau_0^2 \ / | \ \beta_2 |$), whilst L_{nl} is the non-linear length given by the reciprocal of the product between peak power and the non-linear coefficient of the fibre mode ($(P_0\gamma)^{-1}$), which is in turn directly proportional to the non-linear refractive index and inversely proportional to the mode effective area ($\propto n_2/A_{eff}$). The soliton order, therefore, represents the degree of balance between dispersion and self-phase modulation (nonlinearity). Generally, the soliton order for efficient RDW ranges between 2 and 3. The second relevant parameter is the zero-dispersion wavelength λ_{zd}, which for a given driving pulse of wavelength λ_0 sets the frequency at

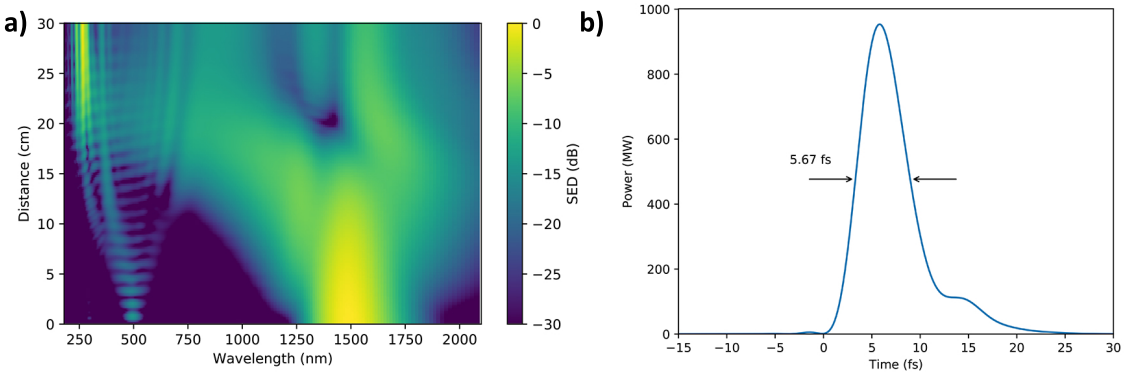

Figure B.1: *Simulated results of RDW emission at 250 nm driven in argon (1.35 bar, gradient of pressure) with a 1500-nm, 15-fs pumping pulse.* ***(a)*** *Spectral energy density (dB) as a function of the wavelength and propagation in the fibre.* ***(b)*** *Temporal profile of the emitted UV radiation at 250 nm showing a FWHM duration of 5.67 fs.*

which the RDW will be emitted. As the name suggests, it is defined as the frequency at which the dispersion is zero $\beta(\lambda_{zd}) = 0$. This wavelength can be tuned by changing the pressure of the gas medium in the fibre. Given a certain geometry, pressure tuning and control are the most relevant parameters for generation, as they directly affect both dispersion and nonlinear response. The full optimization of this process is described in several works, among which [124, 190] to which the reader is referred for further theoretical insights.

Within the scope of this project, the design of a scheme for generating few-cycle UV pulses centered at 250 nm, driven by a 1500-nm pulse, is presented. The scheme has been developed with the support of collaborators at Heriot-Watt University of Edinburgh (UK): Prof. John C. Travers, Prof. Christian Brahms, and their team. The design has been simulated using the *Luna.jl* software [191]. Optimal conditions for generating 5-fs UV pulses at 250 nm are achieved with a 30-cm-long, 75-µm-radius fibre filled with argon in a pressure gradient from 1.35 bar to vacuum, driven by 15-fs NIR pulses centred at 1500 nm with an energy of 71.6 µJ. These parameters correspond to a soliton order of 2.8. Figure B.1 shows the results of the simulation. On the left panel, the spectral energy density as a function of wavelength and propagation in the fibre: the RDW in the UV starts appearing in the last 10 cm of propagation when the spectrum has been sufficiently broadened by self-phase modulation. Panel *b* shows instead the temporal profile of the RDW at 250 nm, with a FWHM duration of about 5 fs. For similar setups based on RDW emission, the simulated temporal profile matches closely the experimental measurements [192]. Figure B.2 is intended to show how the RDW emission arises from the perfect tuning of the driving pulse conditions. Indeed, if the pulse is too long (panel *b*) or the energy is too low (panel *a*), the UV emission is suppressed.

To conclude and for illustrative purposes only, the optical layout of the interferometric pump-probe scheme for transient absorption spectroscopy, including the soft X-ray probe arm (light blue) presented in Ch. 3 and the pump arm (pink) here discussed, is reported in Figure B.3. A third arm, shown in green, indicates the possibility of pumping directly with the driving field at 1500 nm or 800 nm. The beam enters the setup from the right and splits through a beam-splitter (BS) with an 80:20 ratio, ensuring high intensity on the HHG arm. Two delay lines (gray blocks) control the delay down to sub-fs precision. A mirror on a motorized stage (green circle) can be optionally inserted or removed to choose between the UV source or the NIR driving beam. The UV RDW emission is spectrally separated from the driving NIR and then recombined with the probe in a non-collinear geometry at the target (not shown in the picture).

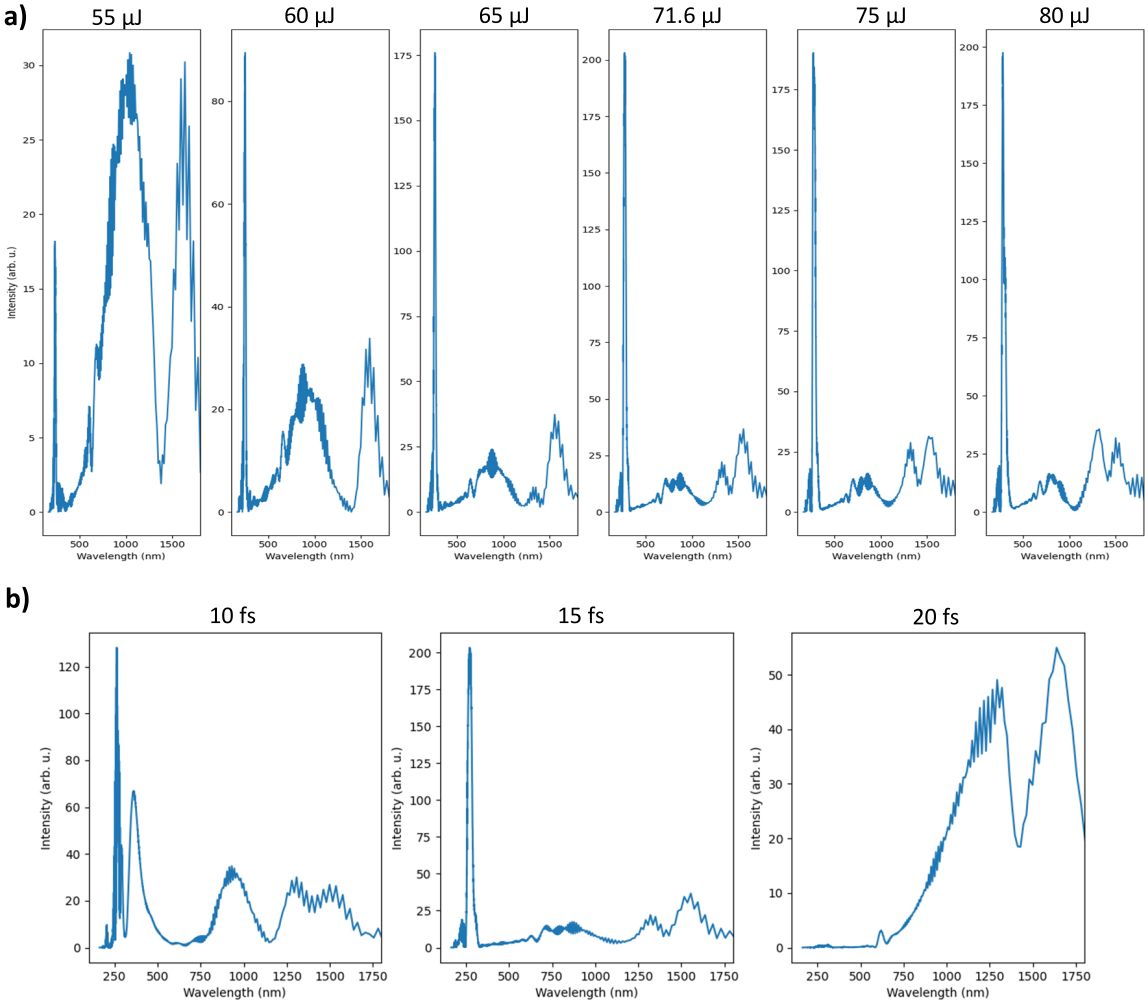

Figure B.2: ***a)*** *Spectral intensity at the output of the fibre (30 cm) for a driving pulse at 1500 nm with energy between 55 and 80 µJ and 15-fs duration.* ***(b)*** *Spectral intensity at the output of the fibre (30 cm) for a driving pulse at 1500 nm with a temporal duration between 10 and 20 fs and energy 71.6 µJ.*

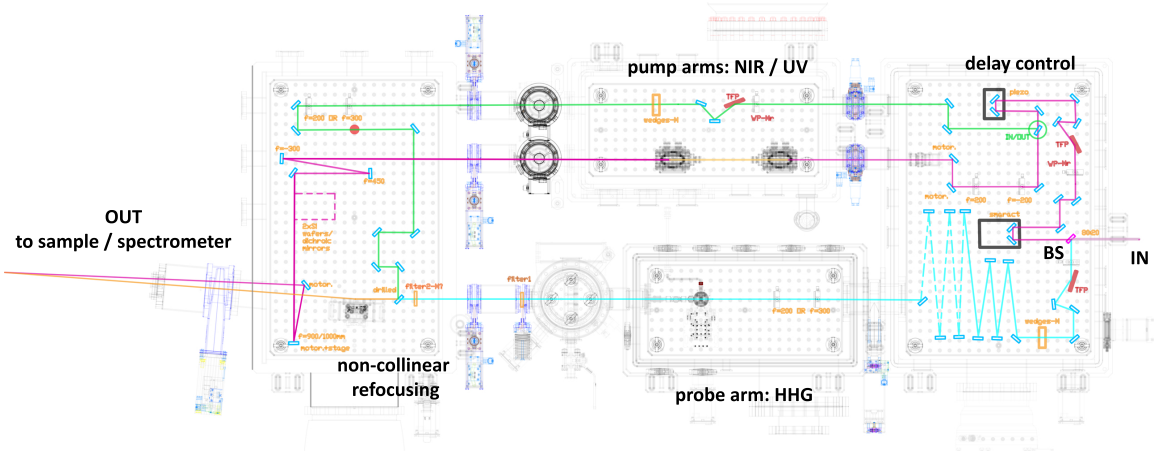

Figure B.3: *Schematic of the optical layout of the pump-probe interferometer made by the HHG source (light-blue) presented in Ch. 3 and the UV pump arm (pink) here illustrated, together with the alternative NIR pump arm (green). The beam enters from the right, splits into two arms (BS: beamsplitter), and after non-collinear refocusing, it reaches the sample and the spectrometer (not illustrated here).*

C | Sign ambiguity and over-segmentation in DBH

As discussed in Ch. 5, the DBH problem with three fields intrinsically include a sign ambiguity. Following the *over-segmentation* method presented in Ref. [160], this section presents simulated results for the reconstruction of two TL Gaussian pulses with spectral bandwidth (FWHM) respectively of 300 and 500 meV, centred at 35.4 eV and 35.5 eV, and delayed by 20 fs. The parameters have been chosen so as to reproduce the experimental conditions reported in Ch. 6.

The concept of over-segmentation is based on the idea that a discrete signal of N points defined over a compact support of width $(\tau+1)$ can change sign at a maximum τ times. In its heuristic implementation, it consists in assigning a sign to $|\Im\{F_1F_2^*\}|$ over constant intervals of points (segments) changing at every local minima. This operation is shown in Figure C.1: panel *a* shows $|\Im\{F_1F_2^*\}|$ as defined in Eq. 5.11, while panel *b* shows $\Im\{F_1F_2^*\}$ after having assigned different sign to each of the segment delimited by local minima. The change of sign is actually performed at the first point after the minimum; here, due to the low number of points chosen, the results aren't smooth. Nevertheless, this is not substantially affecting the final result, provided that the number of segments M obeys $M < N - 2\tau$, a condition ensuring the uniqueness of the solution. The reconstructions with and without sign retrieval through over-segmentation are reported in Figure C.2, respectively panel *a* and *b*, as full lines in comparison with the input of the simulation as dotted lines. In the first case, the reconstruction wrongly attributes to both pulses modulations in the temporal profile. In the latter, corrected for the sign ambiguity, the method well reproduces the input pulses. Here, the reconstruction has been applied for a case without noise, but this strategy has been demonstrated in Ref. [160] also in presence of noise and for more complex scenarios.

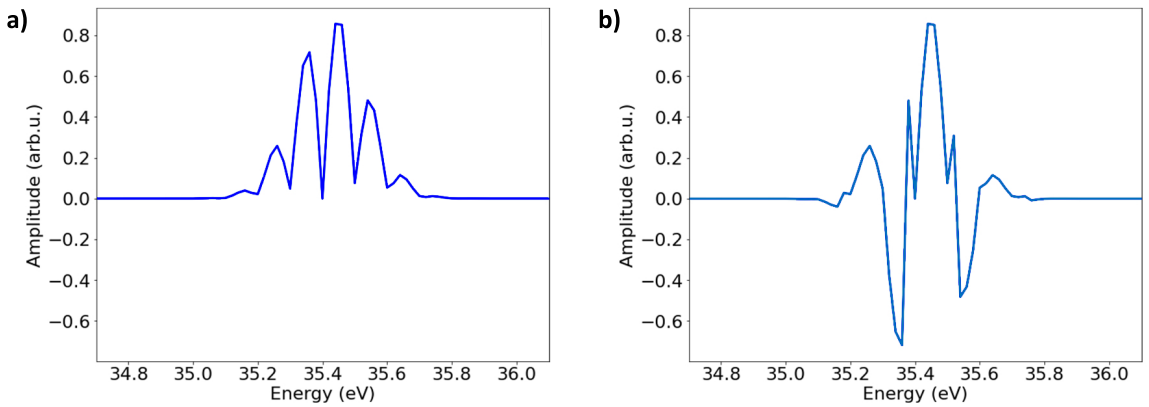

Figure C.1: *Heuristic over-segmentation applied to the simulated* $E_I = \Im\{F_1 F_2^*\}$. ***(a)*** $|E_I|$. ***(b)*** *The resulting* E_I *after assigning an alternating sign to each segment defined by the local minima of* $|E_I|$.

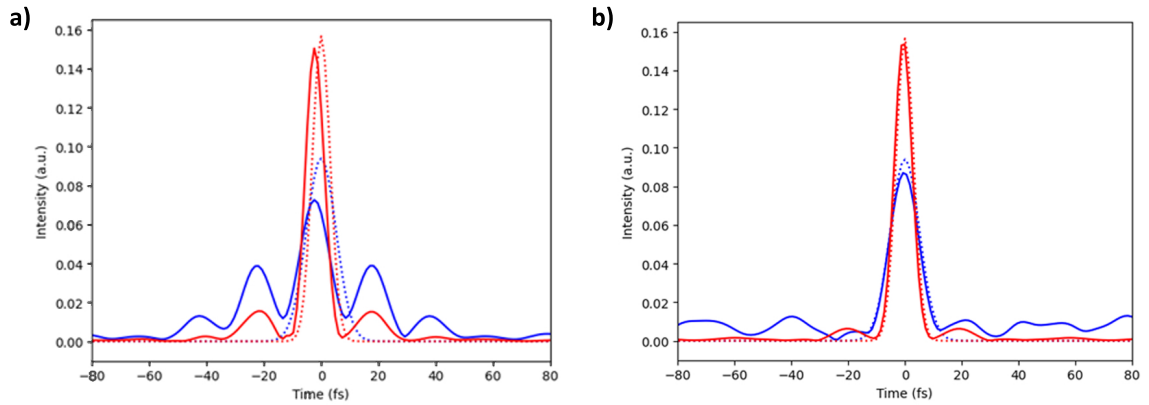

Figure C.2: *Reconstructed temporal signals (full lines) in comparison with the simulated inputs for two Gaussian fields (dotted lines) for the case* ***(a)*** *of direct application of the VPR algorithm without sign retrieval, and* ***(b)*** *after over-segmentation and sign retrieval of* $\Im\{F_1 F_2^*\}$.

D | Copyright and permissions

The following figures reproduced or adapted in this dissertation are subject to copyright. Appropriate permissions have been obtained from the respective publishers, or the material is reproduced under an open access license, as indicated below:

- Figure 1.1: Reproduced and reprinted with permission (Fig. 2) from [1]. Copyright (2025) by the American Physical Society.
- Figure 2.1: Adapted from [68] under the Creative Commons Attribution-Non Commercial-ShareAlike-3.0 License.
- Figure 2.5: Adapted from [85] under the Creative Commons Attribution Non-Commercial License 4.0 (CC BY-NC).
- Figure 3.6: Adapted from [85] under the Creative Commons Attribution Non-Commercial License 4.0 (CC BY-NC).
- Figure 4.2: Adapted with permission from [131] © Optica Publishing Group.
- Figure 4.4: Reproduced from [133] with permission from Elsevier.
- Figure 5.1: Adapted from [161] with permission from Cambridge University Press through PLSclear.
- Figure 5.2: Reproduced from [62] with permission from Springer Nature.
- Figure 5.3: Adapted from [63] under the Creative Commons Attribution 4.0 International License.

All copyright permissions for reproduced or adapted figures were requested and obtained prior to submission (dated September 5, 2025). Documentation of these permissions is available from the author of this thesis (Agata Azzolin) upon request. In some cases, the final title of the dissertation differs from the one indicated in the permission request; however, the intended use remains fully consistent with the granted authorization.

Bibliography

[1] F. Krausz and M. Ivanov. "Attosecond physics". en. In: *Reviews of Modern Physics* 81.1 (Feb. 2009), pp. 163–234. DOI: 10.1103/RevModPhys.81.163.

[2] A. McPherson et al. "Studies of multiphoton production of vacuum-ultraviolet radiation in the rare gases". en. In: *Journal of the Optical Society of America B* 4.4 (Apr. 1987), p. 595. ISSN: 0740-3224, 1520-8540. DOI: 10.1364/JOSAB.4.000595.

[3] X. F. Li et al. "Multiple-harmonic generation in rare gases at high laser intensity". In: *Physical Review A* 39.11 (June 1989), pp. 5751–5761. DOI: 10.1103/PhysRevA.39.5751.

[4] M. Ferray et al. "Multiple-harmonic conversion of 1064 nm radiation in rare gases". en. In: *Journal of Physics B: Atomic, Molecular and Optical Physics* 21.3 (Feb. 1988), p. L31. ISSN: 0953-4075. DOI: 10.1088/0953-4075/21/3/001.

[5] R. Geneaux et al. "Transient absorption spectroscopy using high harmonic generation: a review of ultrafast X-ray dynamics in molecules and solids". en. In: *Philosophical Transactions of the Royal Society A: Mathematical, Physical and Engineering Sciences* 377.2145 (May 2019), p. 20170463. DOI: 10.1098/rsta.2017.0463.

[6] J. Biegert et al. "Attosecond technology(ies) and science". en. In: *Journal of Physics B: Atomic, Molecular and Optical Physics* 54.7 (Apr. 2021), p. 070201. DOI: 10.1088/1361-6455/abcdef.

[7] R. Borrego-Varillas, M. Lucchini, and M. Nisoli. "Attosecond spectroscopy for the investigation of ultrafast dynamics in atomic, molecular and solid-state physics". en. In: *Reports on Progress in Physics* 85.6 (June 2022), p. 066401. DOI: 10.1088/1361-6633/ac5e7f.

[8] M. Nisoli et al. "Attosecond Electron Dynamics in Molecules". en. In: *Chemical Reviews* 117.16 (Aug. 2017), pp. 10760–10825. DOI: 10.1021/acs.chemrev.6b00453.

[9] M. Chini, K. Zhao, and Z. Chang. "The generation, characterization and applications of broadband isolated attosecond pulses". en. In: *Nature Photonics* 8.33 (Mar. 2014), pp. 178–186. ISSN: 1749-4893. DOI: 10.1038/nphoton.2013.362.

[10] J. Li et al. "Attosecond science based on high harmonic generation from gases and solids". In: *Nature Communications* 11.1 (2020), p. 2748. ISSN: 2041-1723. DOI: 10.1038/s41467-020-16480-6. URL: https://doi.org/10.1038/s41467-020-16480-6.

[11] T. Popmintchev et al. "Bright Coherent Ultrahigh Harmonics in the keV X-ray Regime from Mid-Infrared Femtosecond Lasers". en. In: *Science* 336.6086 (June 2012), pp. 1287–1291. ISSN: 0036-8075, 1095-9203. DOI: 10.1126/science.1218497.

[12] A. M. Summers et al. "Realizing Attosecond Core-Level X-ray Spectroscopy for the Investigation of Condensed Matter Systems". In: *Ultrafast Science* 3 (2023), p. 0004. DOI: 10.34133/ultrafastscience.0004.

[13] L. Young et al. "Roadmap of ultrafast x-ray atomic and molecular physics". In: *Journal of Physics B: Atomic, Molecular and Optical Physics* 51.3 (Jan. 2018), p. 032003. DOI: 10.1088/1361-6455/aa9735.

[14] D. Mayer et al. "Following excited-state chemical shifts in molecular ultrafast x-ray photoelectron spectroscopy". en. In: *Nature Communications* 13.1 (Jan. 2022), p. 198. ISSN: 2041-1723. DOI: 10.1038/s41467-021-27908-y.

[15] F. Calegari et al. "Ultrafast electron dynamics in phenylalanine initiated by attosecond pulses". en. In: *Science* 346.6207 (Oct. 2014), pp. 336–339. ISSN: 0036-8075, 1095-9203. DOI: 10.1126/science.1254061.

[16] F. Calegari et al. "Charge migration induced by attosecond pulses in bio-relevant molecules". en. In: *Journal of Physics B: Atomic, Molecular and Optical Physics* 49.14 (July 2016), p. 142001. ISSN: 0953-4075, 1361-6455. DOI: 10.1088/0953-4075/49/14/142001.

[17] S. M. Teichmann et al. "0.5-keV Soft X-ray attosecond continua". en. In: *Nature Communications* 7.1 (May 2016), p. 11493. ISSN: 2041-1723. DOI: 10.1038/ncomms11493.

[18] A. S. Johnson et al. "High-flux soft x-ray harmonic generation from ionization-shaped few-cycle laser pulses". en. In: *Science Advances* 4.5 (May 2018), eaar3761. ISSN: 2375-2548. DOI: 10.1126/sciadv.aar3761.

[19] K. S. Zinchenko et al. “Apparatus for attosecond transient-absorption spectroscopy in the water-window soft-X-ray region”. en. In: *Scientific Reports* 13.1 (Feb. 2023), p. 3059. ISSN: 2045-2322. DOI: 10.1038/s41598-023-29089-8.

[20] J. Tate et al. “Scaling of Wave-Packet Dynamics in an Intense Midinfrared Field”. en. In: *Physical Review Letters* 98.1 (Jan. 2007), p. 013901. ISSN: 0031-9007, 1079-7114. DOI: 10.1103/PhysRevLett.98.013901.

[21] A. D. Shiner et al. “Wavelength Scaling of High Harmonic Generation Efficiency”. en. In: *Physical Review Letters* 103.7 (Aug. 2009), p. 073902. ISSN: 0031-9007, 1079-7114. DOI: 10.1103/PhysRevLett.103.073902.

[22] K. S. Zinchenko et al. “Sub-7-femtosecond conical-intersection dynamics probed at the carbon K-edge”. In: *Science* 371.6528 (2021), pp. 489–494. DOI: 10.1126/science.abf1656.

[23] S. Severino et al. “Attosecond core-level absorption spectroscopy reveals the electronic and nuclear dynamics of molecular ring opening”. In: *Nature Photonics* 18.7 (2024), pp. 731–737. ISSN: 1749-4893. DOI: 10.1038/s41566-024-01436-9. URL: https://doi.org/10.1038/s41566-024-01436-9.

[24] Y.-P. Chang et al. “Electronic dynamics created at conical intersections and its dephasing in aqueous solution”. In: *Nature Physics* 21.1 (2025), pp. 137–145. ISSN: 1745-2481. DOI: 10.1038/s41567-024-02703-w.

[25] N. Saito et al. “Real-time observation of electronic, vibrational, and rotational dynamics in nitric oxide with attosecond soft x-ray pulses at 400 eV”. In: *Optica* 6.12 (Dec. 2019), pp. 1542–1546. DOI: 10.1364/OPTICA.6.001542.

[26] A. Chew et al. “Attosecond transient absorption spectrum of argon at the $L_{2,3}$ edge”. In: *Phys. Rev. A* 97 (3 Mar. 2018), p. 031407. DOI: 10.1103/PhysRevA.97.031407.

[27] D. Matselyukh, V. Svoboda, and H. J. Wörner. “Attosecond X-ray spectroscopy reveals the competing stochastic and ballistic dynamics of a bifurcating Jahn–Teller dissociation”. In: *Nature Communications* 16.1 (2025), p. 6540. ISSN: 2041-1723. DOI: 10.1038/s41467-025-61512-8.

[28] T. P. H. Sidiropoulos et al. “Probing the Energy Conversion Pathways between Light, Carriers, and Lattice in Real Time with Attosecond Core-Level Spectroscopy”. In: *Phys. Rev. X* 11 (4 Dec. 2021), p. 041060. DOI: 10.1103/PhysRevX.11.041060.

[29] M. Geissler, G. Tempea, and T. Brabec. “Phase-matched high-order harmonic generation in the nonadiabatic limit”. In: *Physical Review A* 62.3 (Aug. 2000), p. 033817. DOI: 10.1103/PhysRevA.62.033817.

[30] G. Tempea et al. “Self-Phase-Matched High Harmonic Generation”. In: *Physical Review Letters* 84.19 (May 2000), pp. 4329–4332. DOI: 10.1103/PhysRevLett.84.4329.

[31] V. Wanie et al. “Ultraviolet supercontinuum generation using a differentially-pumped integrated glass chip”. en. In: *Journal of Physics: Photonics* 6.2 (Mar. 2024), p. 025005. ISSN: 2515-7647. DOI: 10.1088/2515-7647/ad2bd3.

[32] C. Vozzi et al. “Millijoule-level phase-stabilized few-optical-cycle infrared parametric source”. en. In: *Optics Letters* 32.20 (Oct. 2007), p. 2957. ISSN: 0146-9592, 1539-4794. DOI: 10.1364/OL.32.002957.

[33] S. Baker et al. “Probing Proton Dynamics in Molecules on an Attosecond Time Scale”. In: *Science* 312.5772 (Apr. 2006), pp. 424–427. DOI: 10.1126/science.1123904.

[34] O. Smirnova et al. “High harmonic interferometry of multi-electron dynamics in molecules”. en. In: *Nature* 460.7258 (Aug. 2009), pp. 972–977. ISSN: 1476-4687. DOI: 10.1038/nature08253.

[35] R. Torres et al. “Revealing molecular structure and dynamics through high-order harmonic generation driven by mid-IR fields”. In: *Physical Review A* 81.5 (May 2010), p. 051802. DOI: 10.1103/PhysRevA.81.051802.

[36] R. M. Lock et al. “Extracting Continuum Electron Dynamics from High Harmonic Emission from Molecules”. In: *Physical Review Letters* 108.13 (Mar. 2012), p. 133901. DOI: 10.1103/PhysRevLett.108.133901.

[37] S. Ghimire et al. “Observation of high-order harmonic generation in a bulk crystal”. en. In: *Nature Physics* 7.2 (Feb. 2011), pp. 138–141. ISSN: 1745-2473, 1745-2481. DOI: 10.1038/nphys1847.

[38] E. Goulielmakis and T. Brabec. “High harmonic generation in condensed matter”. In: *Nature Photonics* 16.6 (2022), pp. 411–421. ISSN: 1749-4893. DOI: 10.1038/s41566-022-00988-y.

[39] J. Park et al. “Recent trends in high-order harmonic generation in solids”. en. In: *Advances in Physics: X* 7.1 (Dec. 2022), p. 2003244. ISSN: 2374-6149. DOI: 10.1080/23746149.2021.2003244.

[40] S. Ghimire and D. A. Reis. “High-harmonic generation from solids”. en. In: *Nature Physics* 15.1 (Jan. 2019), pp. 10–16. ISSN: 1745-2473, 1745-2481. DOI: 10.1038/s41567-018-0315-5.

[41] A. Zong et al. “Emerging ultrafast techniques for studying quantum materials”. en. In: *Nature Reviews Materials* (Feb. 2023). ISSN: 2058-8437. DOI: 10.1038/s41578-022-00530-0.

[42] C. Heide et al. “Ultrafast high-harmonic spectroscopy of solids”. en. In: *Nature Physics* 20.10 (Oct. 2024), pp. 1546–1557. ISSN: 1745-2481. DOI: 10.1038/s41567-024-02640-8.

[43] J. Yan et al. “Terawatt-attosecond hard X-ray free-electron laser at high repetition rate”. en. In: *Nature Photonics* 18.12 (Dec. 2024). Publisher: Nature Publishing Group, pp. 1293–1298. DOI: 10.1038/s41566-024-01566-0.

[44] R. R. Robles et al. “Spectrotemporal Shaping of Attosecond X-Ray Pulses with a Fresh-Slice Free-Electron Laser”. In: *Physical Review Letters* 134.11 (Mar. 2025). Publisher: American Physical Society, p. 115001. DOI: 10.1103/PhysRevLett.134.115001.

[45] P. Franz et al. “Terawatt-scale attosecond X-ray pulses from a cascaded superradiant free-electron laser”. en. In: *Nature Photonics* 18.7 (July 2024). Publisher: Nature Publishing Group, pp. 698–703. DOI: 10.1038/s41566-024-01427-w.

[46] L. Funke et al. “Capturing Nonlinear Electron Dynamics with Fully Characterised Attosecond X-ray Pulses”. In: arXiv:2408.03858 (Nov. 2024). arXiv:2408.03858 [physics]. DOI: 10.48550/arXiv.2408.03858.

[47] E. Schneidmiller et al. “Generation of Ultrashort Pulses in XUV and X-ray FELs via an Excessive Reverse Undulator Taper”. en. In: *Photonics* 10.66 (June 2023), p. 653. ISSN: 2304-6732. DOI: 10.3390/photonics10060653.

[48] J. Duris et al. “Tunable isolated attosecond X-ray pulses with gigawatt peak power from a free-electron laser”. en. In: *Nature Photonics* 14.1 (2020), pp. 30–36. DOI: 10.1038/s41566-019-0549-5.

[49] Z. Guo et al. “Experimental demonstration of attosecond pump–probe spectroscopy with an X-ray free-electron laser”. en. In: *Nature Photonics* 18.7 (July 2024), pp. 691–697. ISSN: 1749-4893. DOI: 10.1038/s41566-024-01419-w.

[50] S. Li et al. “Attosecond coherent electron motion in Auger-Meitner decay”. en. In: *Science* 375.6578 (Jan. 2022), pp. 285–290. DOI: 10.1126/science.abj2096.

[51] T. Driver et al. “Attosecond delays in X-ray molecular ionization”. en. In: *Nature* 632.8026 (Aug. 2024). Publisher: Nature Publishing Group, pp. 762–767. DOI: 10.1038/s41586-024-07771-9.

[52] O. Alexander et al. “Attosecond impulsive stimulated X-ray Raman scattering in liquid water”. In: *Science Advances* 10.39 (Sept. 2024). Publisher: American Association for the Advancement of Science, eadp0841. DOI: 10.1126/sciadv.adp0841.

[53] S. Li et al. “Attosecond-pump attosecond-probe x-ray spectroscopy of liquid water”. In: *Science* 383.6687 (2024), pp. 1118–1122. DOI: 10.1126/science.adn6059.

[54] S. Kuschel et al. “Non-linear enhancement of ultrafast X-ray diffraction through transient resonances”. en. In: *Nature Communications* 16.1 (Jan. 2025). Publisher: Nature Publishing Group, p. 847. DOI: 10.1038/s41467-025-56046-y.

[55] R. Riedel et al. “Single-shot pulse duration monitor for extreme ultraviolet and X-ray free-electron lasers”. en. In: *Nature Communications* 4.1 (Apr. 2013). Publisher: Nature Publishing Group, p. 1731. DOI: 10.1038/ncomms2754.

[56] P. Eckle et al. “Attosecond angular streaking”. In: *Nature Physics* 4.7 (2008), pp. 565–570. ISSN: 1745-2481. DOI: 10.1038/nphys982.

[57] N. Hartmann et al. “Attosecond time–energy structure of X-ray free-electron laser pulses”. en. In: *Nature Photonics* 12.4 (2018), pp. 215–220. DOI: 10.1038/s41566-018-0107-6. URL: http://www.nature.com/articles/s41566-018-0107-6.

[58] R. Heider et al. “Megahertz-compatible angular streaking with few-femtosecond resolution at x-ray free-electron lasers”. In: *Physical Review A* 100.5 (Nov. 2019). Publisher: American Physical Society, p. 053420. DOI: 10.1103/PhysRevA.100.053420. URL: https://link.aps.org/doi/10.1103/PhysRevA.100.053420.

[59] B. Mahieu et al. “Spectral-phase interferometry for direct electric-field reconstruction applied to seeded extreme-ultraviolet free-electron lasers”. In: *Opt. Express* 23.14 (July 2015), pp. 17665–17674. DOI: 10.1364/OE.23.017665.

[60] T. Fuji et al. “Spectral phase interferometry for direct electric-field reconstruction of synchrotron radiation”. EN. In: *Optica* 10.2 (Feb. 2023). Publisher: Optica Publishing Group, pp. 302–307. DOI: 10.1364/OPTICA.477535.

[61] A. Sanchez-Gonzalez et al. “Accurate prediction of X-ray pulse properties from a free-electron laser using machine learning”. en. In: *Nature Communications* 8.1 (June 2017). Publisher: Nature Publishing Group, p. 15461. DOI: 10.1038/ncomms15461.

[62] O. Pedatzur et al. “Double-blind holography of attosecond pulses”. en. In: *Nature Photonics* 13.2 (Feb. 2019), pp. 91–95. ISSN: 1749-4885, 1749-4893. DOI: 10.1038/s41566-018-0308-z.

[63] B. Leshem et al. “Direct single-shot phase retrieval from the diffraction pattern of separated objects”. en. In: *Nature Communications* 7.11 (Feb. 2016), p. 10820. ISSN: 2041-1723. DOI: 10.1038/ncomms10820.

[64] A. L’Huillier et al. “Calculations of high-order harmonic-generation processes in xenon at 1064 nm”. In: *Physical Review A* 46.5 (Sept. 1992), pp. 2778–2790. DOI: 10.1103/PhysRevA.46.2778.

[65] P. B. Corkum. “Plasma perspective on strong field multiphoton ionization”. en. In: *Physical Review Letters* 71.13 (Sept. 1993), pp. 1994–1997. ISSN: 0031-9007. DOI: 10.1103/PhysRevLett.71.1994.

[66] K. J. Schafer et al. “Above threshold ionization beyond the high harmonic cutoff”. en. In: *Physical Review Letters* 70.11 (Mar. 1993), pp. 1599–1602. ISSN: 0031-9007. DOI: 10.1103/PhysRevLett.70.1599.

[67] K. C. Kulander, K. J. Schafer, and J. L. Krause. “Dynamics of Short-Pulse Excitation, Ionization and Harmonic Conversion”. In: *Super-Intense Laser-Atom Physics*. Ed. by B. Piraux, A. L’Huillier, and K. Rzążewski. Vol. 316. NATO ASI Series. Boston, MA: Springer US, 1993, pp. 95–110. ISBN: 978-1-4615-7965-6. DOI: 10.1007/978-1-4615-7963-2_10.

[68] K. L. Ishikawa. “High-Harmonic Generation”. en. In: *Advances in Solid State Lasers Development and Applications*. Ed. by M. Grishin. InTech, Feb. 2010. ISBN: 978-953-7619-80-0. DOI: 10.5772/7961.

[69] A. L’Huillier et al. “High-order Harmonic-generation cutoff”. In: *Physical Review A* 48.5 (Nov. 1993), R3433–R3436. DOI: 10.1103/PhysRevA.48.R3433.

[70] M. Lewenstein et al. “Theory of high-harmonic generation by low-frequency laser fields”. en. In: *Physical Review A* 49.3 (Mar. 1994), pp. 2117–2132. ISSN: 1050-2947, 1094-1622. DOI: 10.1103/PhysRevA.49.2117.

[71] L. V. Keldysh. “Ionization in the field of a strong electromagnetic wave”. In: *Soviet Physics Jept* 20.5 (May 1965).

[72] M. V. Ammosov and V. P. Krainov. “Tunnel ionization of complex atoms and of atomic ions in an alternating electromagnetic field”. en. In: *Journal of Experimental and Theoretical Physics* 91 (Dec. 1986), pp. 2008–2013.

[73] A. M. Perelomov, V. S. Popov, and M. V. Terent'Ev. “Ionization of Atoms in an Alternating Electric Field”. en. In: *Soviet Journal of Experimental and Theoretical Physics* 50 (1966), pp. 1393–1409.

[74] A. Scrinzi, M. Geissler, and T. Brabec. “Ionization Above the Coulomb Barrier”. In: *Physical Review Letters* 83.4 (July 1999), pp. 706–709. DOI: 10.1103/PhysRevLett.83.706.

[75] A. Scrinzi. “Ionization of multielectron atoms by strong static electric fields”. In: *Physical Review A* 61.4 (Mar. 2000), p. 041402. DOI: 10.1103/PhysRevA.61.041402.

[76] M. B. Gaarde, J. L. Tate, and K. J. Schafer. “Macroscopic aspects of attosecond pulse generation”. en. In: *Journal of Physics B: Atomic, Molecular and Optical Physics* 41.13 (June 2008), p. 132001. ISSN: 0953-4075. DOI: 10.1088/0953-4075/41/13/132001.

[77] V. P. Majety and A. Scrinzi. “Static field ionization rates for multi-electron atoms and small molecules”. en. In: *Journal of Physics B: Atomic, Molecular and Optical Physics* 48.24 (Nov. 2015), p. 245603. ISSN: 0953-4075. DOI: 10.1088/0953-4075/48/24/245603.

[78] D. Bauer and P. Mulser. “Exact field ionization rates in the barrier-suppression regime from numerical time-dependent Schrödinger-equation calculations”. In: *Physical Review A* 59.1 (Jan. 1999), pp. 569–577. DOI: 10.1103/PhysRevA.59.569.

[79] X. M. Tong and C. D. Lin. “Empirical formula for static field ionization rates of atoms and molecules by lasers in the barrier-suppression regime”. en. In: *Journal of Physics B: Atomic, Molecular and Optical Physics* 38.15 (July 2005), p. 2593. ISSN: 0953-4075. DOI: 10.1088/0953-4075/38/15/001.

[80] E. Priori et al. “Nonadiabatic three-dimensional model of high-order harmonic generation in the few-optical-cycle regime”. en. In: *Physical Review A* 61.6 (May 2000), p. 063801. ISSN: 1050-2947, 1094-1622. DOI: 10.1103/PhysRevA.61.063801.

[81] R. Weissenbilder et al. “How to optimize high-order harmonic generation in gases”. en. In: *Nature Reviews Physics* 4.11 (Oct. 2022), pp. 713–722. ISSN: 2522-5820. DOI: 10.1038/s42254-022-00522-7.

[82] P. Balcou et al. “Generalized phase-matching conditions for high harmonics: The role of field-gradient forces”. en. In: *Physical Review A* 55.4 (Apr. 1997), pp. 3204–3210. ISSN: 1050-2947, 1094-1622. DOI: 10.1103/PhysRevA.55.3204.

[83] T. Popmintchev et al. “Extended phase matching of high harmonics driven by mid-infrared light”. en. In: *Optics Letters* 33.18 (Sept. 2008), p. 2128. ISSN: 0146-9592, 1539-4794. DOI: 10.1364/OL.33.002128.

[84] T. Popmintchev et al. “Phase matching of high harmonic generation in the soft and hard X-ray regions of the spectrum”. en. In: *Proceedings of the National Academy of Sciences* 106.26 (June 2009), pp. 10516–10521. ISSN: 0027-8424, 1091-6490. DOI: 10.1073/pnas.0903748106.

[85] Z. Fu et al. “Extension of the bright high-harmonic photon energy range via nonadiabatic critical phase matching”. en. In: *Science Advances* 8.51 (Dec. 2022), eadd7482. ISSN: 2375-2548. DOI: 10.1126/sciadv.add7482.

[86] E. A. Gibson et al. “Coherent Soft X-ray Generation in the Water Window with Quasi-Phase Matching”. en. In: *Science* 302.5642 (Oct. 2003), pp. 95–98. ISSN: 0036-8075, 1095-9203. DOI: 10.1126/science.1088654.

[87] O. Cohen et al. “Grating-Assisted Phase Matching in Extreme Nonlinear Optics”. en. In: *Physical Review Letters* 99.5 (July 2007), p. 053902. ISSN: 0031-9007, 1079-7114. DOI: 10.1103/PhysRevLett.99.053902.

[88] A. Paul et al. “Quasi-phase-matched generation of coherent extreme-ultraviolet light”. en. In: *Nature* 421.69186918 (Jan. 2003), pp. 51–54. ISSN: 1476-4687. DOI: 10.1038/nature01222.

[89] X. Zhang et al. “Quasi-phase-matching and quantum-path control of high-harmonic generation using counterpropagating light”. en. In: *Nature Physics* 3.44 (Apr. 2007), pp. 270–275. ISSN: 1745-2481. DOI: 10.1038/nphys541.

[90] A. G. Ciriolo et al. “Microfluidic devices for quasi-phase-matching in high-order harmonic generation”. en. In: *APL Photonics* 7.11 (Nov. 2022), p. 110801. ISSN: 2378-0967. DOI: 10.1063/5.0118199.

[91] K. Kovács et al. “Quasi-Phase-Matching High-Harmonic Radiation Using Chirped THz Pulses”. In: *Physical Review Letters* 108.19 (May 2012), p. 193903. DOI: 10.1103/PhysRevLett.108.193903.

[92] F. Wiegandt et al. “Quasi-phase-matched high-harmonic generation in gas-filled hollow-core photonic crystal fiber”. EN. In: *Optica* 6.4 (Apr. 2019), pp. 442–447. ISSN: 2334-2536. DOI: 10.1364/OPTICA.6.000442.

[93] P.-A. Chevreuil et al. “Water-window high harmonic generation with 0.8-µm and 2.2-µm OPCPAs at 100 kHz”. en. In: *Optics Express* 29.21 (Oct. 2021), p. 32996. ISSN: 1094-4087. DOI: 10.1364/OE.440273.

[94] B. Major et al. “High-order harmonic generation in a strongly overdriven regime”. en. In: *Physical Review A* 107.2 (Feb. 2023), p. 023514. ISSN: 2469-9926, 2469-9934. DOI: 10.1103/PhysRevA.107.023514.

[95] H.-W. Sun et al. “Extended phase matching of high harmonic generation by plasma-induced defocusing”. en. In: *Optica* 4.8 (Aug. 2017), p. 976. ISSN: 2334-2536. DOI: 10.1364/OPTICA.4.000976.

[96] J. Schötz et al. “Phase-Matching for Generation of Isolated Attosecond XUV and Soft-X-Ray Pulses with Few-Cycle Drivers”. en. In: *Physical Review X* 10.4 (Oct. 2020), p. 041011. ISSN: 2160-3308. DOI: 10.1103/PhysRevX.10.041011.

[97] Y. Chen et al. “Phase-matched high-harmonic generation under nonadiabatic conditions: Model and Experiment”. In: *Ultrafast Science* 0.ja (Nov. 2023). DOI: 10.34133/ultrafastscience.0045.

[98] J. Seres et al. “Generation of coherent keV x-rays with intense femtosecond laser pulses”. en. In: *New Journal of Physics* 8.10 (Oct. 2006), p. 251. ISSN: 1367-2630. DOI: 10.1088/1367-2630/8/10/251.

[99] C.-J. Lai and F. X. Kärtner. “The influence of plasma defocusing in high harmonic generation”. en. In: *Optics Express* 19.23 (Nov. 2011), p. 22377. ISSN: 1094-4087. DOI: 10.1364/OE.19.022377.

[100] A.-T. Le et al. “Quantitative rescattering theory for high-order harmonic generation from molecules”. In: *Physical Review A* 80.1 (July 2009), p. 013401. DOI: 10.1103/PhysRevA.80.013401.

[101] J. W. Cooper. “Photoionization from Outer Atomic Subshells. A Model Study”. In: *Physical Review* 128.2 (Oct. 1962), pp. 681–693. DOI: 10.1103/PhysRev.128.681.

[102] G. L. Yudin and M. Y. Ivanov. “Nonadiabatic tunnel ionization: Looking inside a laser cycle”. In: *Physical Review A* 64.1 (June 2001), p. 013409. DOI: 10.1103/PhysRevA.64.013409.

[103] V. Tosa, K. T. Kim, and C. H. Nam. “Macroscopic generation of attosecond-pulse trains in strongly ionized media”. In: *Physical Review A* 79.4 (Apr. 2009), p. 043828. DOI: 10.1103/PhysRevA.79.043828.

[104] C. Vozzi et al. “Phase-matching effects in the generation of high-energy photons by mid-infrared few-cycle laser pulses”. en. In: *New Journal of Physics* 13.7 (July 2011), p. 073003. ISSN: 1367-2630. DOI: 10.1088/1367-2630/13/7/073003.

[105] V. Tosa et al. “Attosecond pulses generated by the lighthouse effect in Ar gas”. In: *Physical Review A* 91.5 (May 2015), p. 051801. DOI: 10.1103/PhysRevA.91.051801.

[106] E. Constant et al. “Optimizing High Harmonic Generation in Absorbing Gases: Model and Experiment”. en. In: *Physical Review Letters* 82.8 (Feb. 1999), pp. 1668–1671. ISSN: 0031-9007, 1079-7114. DOI: 10.1103/PhysRevLett.82.1668.

[107] V. Tosa et al. “Propagation effects in highly ionised gas media”. en. In: *Quantum Electronics* 46.4 (Apr. 2016), p. 321. ISSN: 1063-7818. DOI: 10.1070/QEL16039.

[108] M. Lucchini et al. “Nonadiabatic quantum path analysis of the high-order harmonic generation in a highly ionized medium”. en. In: *New Journal of Physics* 14.3 (Mar. 2012), p. 033009. ISSN: 1367-2630. DOI: 10.1088/1367-2630/14/3/033009.

[109] B. L. Henke, E. M. Gullikson, and J. C. Davis. “X-Ray Interactions: Photoabsorption, Scattering, Transmission, and Reflection at E = 50-30,000 eV, Z = 1-92”. In: *Atomic Data and Nuclear Data Tables* 54.2 (July 1993), pp. 181–342. ISSN: 0092-640X. DOI: 10.1006/adnd.1993.1013.

[110] S. Mitra et al. “Propagation effects in polarization-gated attosecond soft-X-ray pulse generation”. EN. In: *Optics Express* 32.2 (Jan. 2024), pp. 1151–1160. ISSN: 1094-4087. DOI: 10.1364/OE.504636.

[111] R. Martínez Vázquez et al. “Femtosecond laser micromachining of integrated glass devices for high-order harmonic generation”. en. In: *International Journal of Applied Glass Science* 13.2 (Apr. 2022), pp. 162–170. ISSN: 2041-1286, 2041-1294. DOI: 10.1111/ijag.16546.

[112] K. C. Vishnubhatla et al. “Shape control of microchannels fabricated in fused silica by femtosecond laser irradiation and chemical etching”. en. In: *Optics Express* 17.10 (May 2009), p. 8685. ISSN: 1094-4087. DOI: 10.1364/OE.17.008685.

[113] R. Osellame et al. “Femtosecond laser microstructuring: an enabling tool for optofluidic lab-on-chips”. en. In: *Laser & Photonics Reviews* 5.3 (2011), pp. 442–463. ISSN: 1863-8899. DOI: 10.1002/lpor.201000031.

[114] *COMSOL Multiphysics, Free Molecular Flow Module Documentation.* URL: https://doc.comsol.com/5.5/doc/com.comsol.help.molec/molec_ug_modeling.5.07.html.

[115] P. Barbato. “Femtosecond laser micromachining of integrated optofluidic devices for extreme UV generation in gases”. eng. Accepted: 2021-05-20T07:18:07Z. Apr. 2021. URL: https://www.politesi.polimi.it/handle/10589/173597.

[116] D. W. Lodi. “Femtosecond laser micromachining of integrated optofluidic devices for HHG and Soft-X spectroscopy”. eng. Accepted: 2023-03-16T15:21:48Z. Dec. 2022. URL: https://www.politesi.polimi.it/handle/10589/197113.

[117] C. Trallero-Herrero et al. “Generation of broad XUV continuous high harmonic spectra and isolated attosecond pulses with intense mid-infrared lasers”. en. In: *Journal of Physics B: Atomic, Molecular and Optical Physics* 45.1 (Dec. 2011), p. 011001. ISSN: 0953-4075. DOI: 10.1088/0953-4075/45/1/011001.

[118] T. Harada et al. “Optimum design of a grazing-incidence flat-field spectrograph with a spherical varied-line-space grating”. en. In: *Applied Optics* 38.13 (May 1999), p. 2743. ISSN: 0003-6935, 1539-4522. DOI: 10.1364/AO.38.002743.

[119] N. Ishii et al. “Generation of soft x-ray and water window harmonics using a few-cycle, phase-locked, optical parametric chirped-pulse amplifier”. en. In: *Optics Letters* 37.1 (Jan. 2012), p. 97. ISSN: 0146-9592, 1539-4794. DOI: https://doi.org/10.1038/ncomms4331.

[120] D. Gabor. “Theory of communication. Part 1: The analysis of information”. In: *Journal of the Institution of Electrical Engineers - Part III: Radio and Communication Engineering* 93.26 (Nov. 1946), pp. 429–441. DOI: 10.1049/ji-3-2.1946.0074.

[121] C. C. Chirilă et al. “Emission times in high-order harmonic generation”. In: *Physical Review A* 81.3 (Mar. 2010), p. 033412. DOI: 10.1103/PhysRevA.81.033412.

[122] D. Kazazis et al. “Extreme ultraviolet lithography”. en. In: *Nature Reviews Methods Primers* 4.1 (Nov. 2024), p. 84. ISSN: 2662-8449. DOI: 10.1038/s43586-024-00361-z.

[123] J. v. Schoot. “Exposure Tool Development Toward Advanced EUV Lithography: A Journey of 40 Years Driving Moore’s Law”. In: *IEEE Electron Devices Magazine* 2.1 (Mar. 2024), pp. 8–22. ISSN: 2832-7691. DOI: 10.1109/MED.2023.3337129.

[124] J. C. Travers et al. “High-energy pulse self-compression and ultraviolet generation through soliton dynamics in hollow capillary fibres”. en. In: *Nature Photonics* 13.8 (Aug. 2019), pp. 547–554. ISSN: 1749-4885, 1749-4893. DOI: 10.1038/s41566-019-0416-4.

[125] J. D. Koralek et al. “Generation and characterization of ultrathin free-flowing liquid sheets”. en. In: *Nature Communications* 9.1 (Apr. 2018), p. 1353. ISSN: 2041-1723. DOI: 10.1038/s41467-018-03696-w.

[126] G. Giovannetti et al. “Real-Time Tracking of the intramolecular vibrational dynamics of liquid water”. Under Review, Nature portfolio. June 2025. DOI: 10.21203/rs.3.rs-6745336/v1.

[127] S. Kundu and A. Patra. “Nanoscale Strategies for Light Harvesting”. In: *Chemical Reviews* 117.2 (Jan. 2017), pp. 712–757. ISSN: 0009-2665. DOI: 10.1021/acs.chemrev.6b00036.

[128] X. Liu et al. “Large-Scale Integration of Semiconductor Nanowires for High-Performance Flexible Electronics”. In: *ACS Nano* 6.3 (Mar. 2012), pp. 1888–1900. ISSN: 1936-0851. DOI: 10.1021/nn204848r.

[129] H. Lakhotia et al. “Laser picoscopy of valence electrons in solids”. en. In: *Nature* 583.7814 (July 2020), pp. 55–59. ISSN: 0028-0836, 1476-4687. DOI: 10.1038/s41586-020-2429-z.

[130] Q. Guo et al. “Fundamentals of TiO2 Photocatalysis: Concepts, Mechanisms, and Challenges”. en. In: *Advanced Materials* 31.50 (2019), p. 1901997. ISSN: 1521-4095. DOI: 10.1002/adma.201901997.

[131] L. Yue and M. B. Gaarde. “Introduction to theory of high-harmonic generation in solids: tutorial”. en. In: *Journal of the Optical Society of America B* 39.2 (Feb. 2022), p. 535. ISSN: 0740-3224, 1520-8540. DOI: 10.1364/JOSAB.448602.

[132] Y. S. You et al. “High-harmonic generation in amorphous solids”. en. In: *Nature Communications* 8.1 (Sept. 2017), p. 724. ISSN: 2041-1723. DOI: 10.1038/s41467-017-00989-4.

[133] V. Etacheri et al. “Visible-light activation of TiO2 photocatalysts: Advances in theory and experiments”. In: *Journal of Photochemistry and Photobiology C: Photochemistry Reviews* 25 (2015), pp. 1–29. ISSN: 1389-5567. DOI: https://doi.org/10.1016/j.jphotochemrev.2015.08.003.

[134] S. Y. Harouna-Mayer et al. “Real-space texture and pole-figure analysis using the 3D pair distribution function on a platinum thin film”. en. In: *IUCrJ* 9.5 (Sept. 2022), pp. 594–603. ISSN: 2052-2525. DOI: 10.1107/S2052252522006674.

[135] K. Choudhary et al. “Ultrathin Films of TiO2 Nanoparticles at Interfaces”. In: *Langmuir* 31.4 (Feb. 2015), pp. 1385–1392. ISSN: 0743-7463. DOI: 10.1021/la503514p.

[136] P. Xia et al. “Nonlinear propagation effects in high harmonic generation in reflection and transmission from gallium arsenide”. In: *Opt. Express* 26.22 (Oct. 2018), pp. 29393–29400. DOI: 10.1364/OE.26.029393.

[137] G. Vampa et al. “Observation of backward high-harmonic emission from solids”. In: *Opt. Express* 26.9 (Apr. 2018), pp. 12210–12218. DOI: 10.1364/OE.26.012210.

[138] J. Lu et al. “Interferometry of dipole phase in high harmonics from solids”. In: *Nature Photonics* 13.2 (2019), pp. 96–100. ISSN: 1749-4893. DOI: 10.1038/s41566-018-0326-x.

[139] N. Bloembergen and P. S. Pershan. “Light Waves at the Boundary of Nonlinear Media”. In: *Phys. Rev.* 128 (2 Oct. 1962), pp. 606–622. DOI: 10.1103/PhysRev.128.606.

[140] Y. S. You, D. A. Reis, and S. Ghimire. “Anisotropic high-harmonic generation in bulk crystals”. en. In: *Nature Physics* 13.44 (Apr. 2017), pp. 345–349. ISSN: 1745-2481. DOI: 10.1038/nphys3955.

[141] D. von der Linde et al. “Generation of high-order harmonics from solid surfaces by intense femtosecond laser pulses”. In: *Phys. Rev. A* 52 (1 July 1995), R25–R27. DOI: 10.1103/PhysRevA.52.R25.

[142] P. A. Norreys et al. “Efficient Extreme UV Harmonics Generated from Picosecond Laser Pulse Interactions with Solid Targets”. In: *Phys. Rev. Lett.* 76 (11 Mar. 1996), pp. 1832–1835. DOI: 10.1103/PhysRevLett.76.1832.

[143] N. H. Burnett et al. “Harmonic generation in CO2 laser target interaction”. In: *Applied Physics Letters* 31.3 (Aug. 1977), pp. 172–174. ISSN: 0003-6951. DOI: 10.1063/1.89628.

[144] R. L. Carman, D. W. Forslund, and J. M. Kindel. "Visible Harmonic Emission as a Way of Measuring Profile Steepening". In: *Phys. Rev. Lett.* 46 (1 Jan. 1981), pp. 29–32. DOI: 10.1103/PhysRevLett.46.29.

[145] U. Teubner and P. Gibbon. "High-order harmonics from laser-irradiated plasma surfaces". In: *Rev. Mod. Phys.* 81 (2 Apr. 2009), pp. 445–479. DOI: 10.1103/RevModPhys.81.445.

[146] A. Tarasevitch, C. Wünsche, and D. von der Linde. "High-Order Harmonics from Plasma Surfaces". In: *Strong Field Laser Physics*. Ed. by T. Brabec. New York, NY: Springer New York, 2009, pp. 301–319. ISBN: 978-0-387-34755-4. DOI: 10.1007/978-0-387-34755-4_14.

[147] G. Vampa et al. "Attosecond synchronization of extreme ultraviolet high harmonics from crystals". In: *Journal of Physics B: Atomic, Molecular and Optical Physics* 53.14 (June 2020), p. 144003. DOI: 10.1088/1361-6455/ab8e56.

[148] T. Journigan et al. "High harmonic generation in epitaxially grown zinc oxide films". EN. In: *JOSA B* 41.6 (June 2024), B1–B6. ISSN: 1520-8540. DOI: 10.1364/JOSAB.503550.

[149] S. Yamada and K. Yabana. "Determining the optimum thickness for high harmonic generation from nanoscale thin films: An ab initio computational study". In: *Phys. Rev. B* 103 (15 Apr. 2021), p. 155426. DOI: 10.1103/PhysRevB.103.155426.

[150] S. Sarkar et al. "Hybridized Guided-Mode Resonances via Colloidal Plasmonic Self-Assembled Grating". In: *ACS Applied Materials & Interfaces* 11.14 (Apr. 2019), pp. 13752–13760. ISSN: 1944-8244. DOI: 10.1021/acsami.8b20535.

[151] S. Ghimire et al. "Generation and propagation of high-order harmonics in crystals". en. In: *Physical Review A* 85.4 (Apr. 2012), p. 043836. ISSN: 1050-2947, 1094-1622. DOI: 10.1103/PhysRevA.85.043836. (Visited on 04/18/2023).

[152] Á. Jiménez-Galán et al. "Orbital perspective on high-harmonic generation from solids". In: *Nature Communications* 14.1 (2023), p. 8421. ISSN: 2041-1723. DOI: 10.1038/s41467-023-44041-0.

[153] A. Annunziata et al. "High-order harmonic generation in liquid crystals". In: *APL Photonics* 9.6 (July 2024), p. 060801. ISSN: 2378-0967. DOI: 10.1063/5.0191184.

[154] H. N. Gopalakrishna et al. "Tracing spatial confinement in semiconductor quantum dots by high-order harmonic generation". In: *Phys. Rev. Res.* 5 (1 Feb. 2023), p. 013128. DOI: 10.1103/PhysRevResearch.5.013128.

[155] W.-X. Yang. "High-order harmonics in a quantum dot and metallic nanorod complex". In: *Opt. Lett.* 40.21 (Nov. 2015), pp. 4903–4906. DOI: 10.1364/OL.40.004903.

[156] K. Nakagawa et al. "Size-controlled quantum dots reveal the impact of intraband transitions on high-order harmonic generation in solids". In: *Nature Physics* 18.8 (2022), pp. 874–878. ISSN: 1745-2481. DOI: 10.1038/s41567-022-01639-3.

[157] S. Han et al. "High-harmonic generation by field enhanced femtosecond pulses in metal-sapphire nanostructure". In: *Nature Communications* 7.1 (2016), p. 13105. ISSN: 2041-1723. DOI: 10.1038/ncomms13105.

[158] G. Vampa et al. "Plasmon-enhanced high-harmonic generation from silicon". In: *Nature Physics* 13.7 (2017), pp. 659–662. ISSN: 1745-2481. DOI: 10.1038/nphys4087.

[159] O. Raz, N. Dudovich, and B. Nadler. "Vectorial Phase Retrieval of 1-D Signals". In: *IEEE Transactions on Signal Processing* 61.7 (Apr. 2013), pp. 1632–1643. ISSN: 1941-0476. DOI: 10.1109/TSP.2013.2239994.

[160] B. Leshem et al. "The discrete sign problem: Uniqueness, recovery algorithms and phase retrieval applications". In: *Applied and Computational Harmonic Analysis* 45.3 (Nov. 2018), pp. 463–485. ISSN: 1063-5203. DOI: 10.1016/j.acha.2016.12.003.

[161] F. L. Pedrotti, L. M. Pedrotti, and L. S. Pedrotti. *Introduction to Optics*. en. 3rd. Cambridge University Press, Dec. 2017. ISBN: 9781108552493. DOI: 10.1017/9781108552493.

[162] O. Raz et al. "Vectorial Phase Retrieval for Linear Characterization of Attosecond Pulses". In: *Physical Review Letters* 107.13 (Sept. 2011), p. 133902. DOI: 10.1103/PhysRevLett.107.133902.

[163] O. Raz et al. "Direct phase retrieval in double blind Fourier holography". EN. In: *Optics Express* 22.21 (Oct. 2014), pp. 24935–24950. ISSN: 1094-4087. DOI: 10.1364/OE.22.024935.

[164] Y. Mairesse and F. Quéré. "Frequency-resolved optical gating for complete reconstruction of attosecond bursts". en. In: *Physical Review A* 71.1 (Jan. 2005), p. 011401. ISSN: 1050-2947, 1094-1622. DOI: 10.1103/PhysRevA.71.011401.

[165] G. Sansone et al. “Isolated Single-Cycle Attosecond Pulses”. en. In: *Science* 314.5798 (Oct. 2006), pp. 443–446. ISSN: 0036-8075, 1095-9203. DOI: 10.1126/science.1132838.

[166] E. L. Saldin, E. A. Schneidmiller, and M. V. Yurkov. “The physics of free electron lasers. An introduction”. In: *Physics Reports* 260.4 (Sept. 1995), pp. 187–327. ISSN: 0370-1573. DOI: 10.1016/0370-1573(95)00004-Z.

[167] V. K. Khanna. “Free electron lasers”. en. In: *Practical Terahertz Electronics: Devices and Applications, Volume 1: Solid-state devices and vacuum tubes*. IOP Publishing, Dec. 2021. DOI: 10.1088/978-0-7503-3171-5ch10.

[168] E. Appi et al. “Synchronized beamline at FLASH2 based on high-order harmonic generation for two-color dynamics studies”. In: *Review of Scientific Instruments* 92.12 (Dec. 2021), p. 123004. ISSN: 0034-6748. DOI: 10.1063/5.0063225.

[169] M. R. Bionta et al. “Spectral encoding of x-ray/optical relative delay”. EN. In: *Optics Express* 19.22 (Oct. 2011), pp. 21855–21865. ISSN: 1094-4087. DOI: 10.1364/OE.19.021855.

[170] P. Grychtol et al. “Timing and X-ray pulse characterization at the Small Quantum Systems instrument of the European X-ray Free Electron Laser”. EN. In: *Optics Express* 29.23 (Nov. 2021), pp. 37429–37442. ISSN: 1094-4087. DOI: 10.1364/OE.440718.

[171] I. Gorgisyan et al. “THz streak camera method for synchronous arrival time measurement of two-color hard X-ray FEL pulses”. EN. In: *Optics Express* 25.3 (Feb. 2017), pp. 2080–2091. ISSN: 1094-4087. DOI: 10.1364/OE.25.002080.

[172] M. Diez et al. “A sensitive high repetition rate arrival time monitor for X-ray free electron lasers”. en. In: *Nature Communications* 14.1 (Apr. 2023), p. 2495. ISSN: 2041-1723. DOI: 10.1038/s41467-023-38143-y.

[173] P. M. Paul et al. “Observation of a Train of Attosecond Pulses from High Harmonic Generation”. en. In: *Science* 292.5522 (June 2001), pp. 1689–1692. ISSN: 0036-8075, 1095-9203. DOI: 10.1126/science.1059413.

[174] H. Muller. “Reconstruction of attosecond harmonic beating by interference of two-photon transitions”. en. In: *Applied Physics B* 74.S1 (June 2002), s17–s21. ISSN: 0946-2171, 1432-0649. DOI: 10.1007/s00340-002-0894-8.

[175] U. Fano. “Sullo spettro di assorbimento dei gas nobili presso il limite dello spettro d’arco”. it. In: *Il Nuovo Cimento (1924-1942)* 12.3 (Mar. 1935), pp. 154–161. ISSN: 1827-6121. DOI: 10.1007/BF02958288.

[176] C. Cirelli et al. “Anisotropic photoemission time delays close to a Fano resonance”. en. In: *Nature Communications* 9.1 (Mar. 2018), p. 955. ISSN: 2041-1723. DOI: 10.1038/s41467-018-03009-1.

[177] B. R. Nebgen et al. *Isostructural electronic transition in MoS_2 probed by solid-state high harmonic generation spectroscopy*. 2025. arXiv: 2506.14215 [cond-mat.mtrl-sci].

[178] O. Kneller et al. “Attosecond transient interferometry”. en. In: *Nature Photonics* (Nov. 2024), pp. 1–8. ISSN: 1749-4893. DOI: 10.1038/s41566-024-01556-2.

[179] S. Zayko et al. “Ultrafast high-harmonic nanoscopy of magnetization dynamics”. en. In: *Nature Communications* 12.11 (Nov. 2021), p. 6337. ISSN: 2041-1723. DOI: 10.1038/s41467-021-26594-0.

[180] P. Dombi et al. “Strong-field nano-optics”. In: *Reviews of Modern Physics* 92.2 (June 2020), p. 025003. DOI: 10.1103/RevModPhys.92.025003.

[181] A. Korobenko et al. “In situ high-harmonic microscopy of a nanostructured solid”. EN. In: *Optica* 10.5 (May 2023), pp. 642–649. ISSN: 2334-2536. DOI: 10.1364/OPTICA.488545.

[182] M. Zürch et al. “Real-time and Sub-wavelength Ultrafast Coherent Diffraction Imaging in the Extreme Ultraviolet”. en. In: *Scientific Reports* 4.11 (Dec. 2014), p. 7356. ISSN: 2045-2322. DOI: 10.1038/srep07356.

[183] A. Gorlach et al. “High-harmonic generation driven by quantum light”. en. In: *Nature Physics* (Aug. 2023), pp. 1–8. ISSN: 1745-2481. DOI: 10.1038/s41567-023-02127-y.

[184] A. Rasputnyi et al. “High-harmonic generation by a bright squeezed vacuum”. en. In: *Nature Physics* 20.12 (Dec. 2024), pp. 1960–1965. ISSN: 1745-2481. DOI: 10.1038/s41567-024-02659-x.

[185] D. Theidel et al. “Evidence of the Quantum Optical Nature of High-Harmonic Generation”. In: *PRX Quantum* 5.4 (Nov. 2024), p. 040319. DOI: 10.1103/PRXQuantum.5.040319.

[186] S. Lemieux et al. “Photon bunching in high-harmonic emission controlled by quantum light”. en. In: *Nature Photonics* 19.7 (July 2025), pp. 767–771. ISSN: 1749-4893. DOI: 10.1038/s41566-025-01673-6.

[187] E. Lindroth et al. “Challenges and opportunities in attosecond and XFEL science”. en. In: *Nature Reviews Physics* 1.2 (Jan. 2019), pp. 107–111. ISSN: 2522-5820. DOI: 10.1038/s42254-019-0023-9.

[188] M. Ilchen et al. “Opportunities for gas-phase science at short-wavelength free-electron lasers with undulator-based polarization control”. In: *Physical Review Research* 7.1 (Jan. 2025), p. 011001. DOI: 10.1103/PhysRevResearch.7.011001.

[189] *COMSOL Multiphysics, High Mach Number Flow Interface Documentation.* URL: https://doc.comsol.com/5.5/doc/com.comsol.help.cfd/cfd_ug_fluidflow_high_mach.08.04.html#1485526.

[190] J. C. Travers et al. “Ultrafast nonlinear optics in gas-filled hollow-core photonic crystal fibers [Invited]”. en. In: *Journal of the Optical Society of America B* 28.12 (Dec. 2011), A11. ISSN: 0740-3224, 1520-8540. DOI: 10.1364/JOSAB.28.000A11.

[191] C. Brahms and J. C. Travers. *Luna.jl*. DOI: 10.5281/zenodo.5513570.

[192] M. Reduzzi et al. “Direct temporal characterization of sub-3-fs deep UV pulses generated by resonant dispersive wave emission”. EN. In: *Optics Express* 31.16 (July 2023), pp. 26854–26864. ISSN: 1094-4087. DOI: 10.1364/OE.494879.

Publication list

Peer-reviewed journals

1. A. Azzolin, et al. "Engineering High-Order Harmonic Generation through Gas Confinement at Sub-Millimeter Lengths". Preprint: `arXiv:2510.09496`, 2025. Accepted in *Journal of Physics: Photonics*, January 2026.

2. A. Azzolin, et al. "Double-Blind Holography of Ultrashort Free-Electron Laser Pulses," Manuscript in preparation, 2025.

Conference proceedings

1. A. Azzolin, et al. "Double-blind holography of ultrashort free-electron laser pulses", 2025, 10th International Conference on Attosecond Science and Technology, ATTO X, Lund, Sweden. Oral contribution. Book of Abstracts.

2. O. Cannelli, A. Azzolin, et al. "Efficient high-order harmonic generation in the overdriven regime in a sub-mm glass chip", 2025, 10th International Conference on Attosecond Science and Technology, ATTO X, Lund, Sweden. Poster contribution. Book of Abstracts.

3. S. Rockenstein, G. Giovannetti, A. Azzolin, et al. "Ultrathin liquid flat jet system for attosecond spectroscopy of solvated molecules", 10th International Conference on Attosecond Science and Technology, ATTO X, Lund, Sweden. Poster contribution. Book of Abstracts.

4. A. Azzolin, et al. "Double-blind holography with ultrashort free-electron laser pulses", 2025, Conference on Lasers and Electro-Optics Europe & European Quantum Electronics Conference (CLEO/Europe-EQEC), Munich, Germany. Oral contribution.

5. A. Azzolin, et al. "Nonadiabatic High-order Harmonic Generation in Chip", 2024, The 23rd International Conference on Ultrafast Phenomena, Barcelona, Spain. Poster contribution.

6. A. Azzolin, O. Cannelli, et al. "Single-Shot Double-Blind Holography of Self-Amplified Spontaneous Emission Pulses of Free Electron Lasers", 2024, The 23rd International Conference on Ultrafast Phenomena, Barcelona, Spain. Oral contribution.

7. A. Azzolin, O. Cannelli, et al. "Single-shot Double-blind Holography of Self-amplified Spontaneous Emission Pulses of Free Electron Lasers", 2024, Science @FELs, Paris, France. Poster contribution. Book of Abstracts.

8. R. Martínez Vázquez, A. Azzolin, et al. "Integrated microfluidic devices for high-order harmonic generation," Proc. SPIE PC12869, Nonlinear Frequency Generation and Conversion: Materials and Devices XXIII, PC128690M (13 March 2024). https://doi.org/10.1117/12.3001819

9. A. Azzolin, et al. "Nonadiabatic Harmonic Generation in a Sub-mm Glass Chip", 2024, High-Brightness Sources and Light-Driven Interactions Congress, Wien, Austria. Invited oral contribution. Technical Digest Series (Optica Publishing Group, 2024), paper HW3B.4. https://doi.org/10.1364/HILAS.2024.HW3B.4

10. A. Azzolin et al., "High-order Harmonic Generation in the nonadiabatic regime over a sub-mm glass chip", 2023, Frontiers in Optics + Laser Science (FiO, LS), Tacoma, USA. Post-deadline oral contribution. Technical Digest Series (Optica Publishing Group, 2023), paper JTu7C.5. https://doi.org/10.1364/FIO.2023.JTu7C.5

11. A. Azzolin et al., "High-Order Harmonic Generation in a Sub-mm Glass Chip", 2023, Conference on Lasers and Electro-Optics Europe & European Quantum Electronics Conference (CLEO/Europe-EQEC), Munich, Germany. Oral contribution. https://doi.org/10.1109/CLEO/Europe-EQEC57999.2023.10231415

Acknowledgements

A doctorate is a transformative experience, marked by highs and lows. It demands effort, commitment, passion, and the right mix of fun and self-irony to endure.
The results and scientific knowledge gained over the years were possible in the first place thanks to my supervisor, Francesca, whom I deeply thank for her guidance and support. Andrea, Vincent, and Terry, your engaging scientific discussions have been pushing me forward every time: thank you. Erik, without you, this group and all of us could not have lasted a day: thank you for your extensive help on the most diverse tasks. Special thanks to those I spent most of my hours with in the lab: the Soft-X team—past members, Gaia, Fan, Sabbir, and present members, Sabine, Linda, Noah, and Oliviero. You will always hold a special place in my memories. Oliviero, your mentorship over the past few years has been crucial, and I am deeply grateful for it. Thank you, Patricia, for your support outside the lab, our nice morning chats were always giving me the right start into the day. To all the other CFEL-ATTO members over the years—Kai, Marc, Kate, Sergey, Ammar, Lorenzo, Ana, Katinka, Laura, Klas, Keno, Keerthana, Fatemeh, Felix, Alex—thank you for sharing this adventure with fun and passion.
To all the many collaborators of the projects presented here, I extend my gratitude for the valuable discussions and the trust you placed in working together. To my co-supervisor, Markus, thank you for the guidance over the years.
To my mentors, Danka and Tobias, who truly helped me navigate the ups and downs of this doctorate: thank you for listening and supporting me, your words have always been of great encouragement.
A special thank you to the Optica Student Chapter, POSHH, and all its members. It has been a great experience and way of doing science also outside the labs. It gave me the chance to meet amazing people, and find again motivation and enthusiasm when I was lacking it.
My close friends and family always got the unfiltered story of this journey. Sometimes, they got only the complaints. I hope that with this achievement, they can also see the joy of doing science. They are and will always be my safety net, and I couldn't

be more grateful for this.

After years abroad, home is hard to define, but I think I've found mine, and it's Dan—wherever we go. Thank you for navigating life with me with endless patience, love, care, and dedication.

This doctorate hasn't broken or bent me. I am proud of what I have achieved and deeply grateful for this experience.

Vola solo chi osa farlo